Degradation, Efficiency, and Equilibrium of a Dead-Ended Anode Fuel Cell

by

Jixin Chen

A dissertation submitted in partial fulfillment
of the requirements for the degree of
Doctor of Philosophy
(Mechanical Engineering)
in The University of Michigan
2013

Doctoral Committee:

Professor Anna G. Stefanopoulou, Co-Chair
Research Scientist Jason B. Siegel, Co-Chair
Assistant Professor Donald J. Siegel
Professor Levi T. Thompson
Ford Technical Expert James R. Waldecker

© Jixin Chen

All Rights Reserved
2013

Attitude is everything.

— Francie Baltazar-Schwartz

To Xinli and Liangdi

Acknowledgments

I would like sincerely to thank my co-advisors Anna Stefanopoulou and Jason Siegel, from the bottom of my heart, for their guidance, discussion, and help throughout my Ph.D. study. Their brilliance, enthusiasm, and tirelessness always motivated me to work even harder towards my dream. The Ph.D. experiences with them have been wonderful and will remain unforgettable for the rest of my life, and I hope that they can be my advisors, not only academically but also spiritually, for the rest of my life.

During my two internships at Fuel Cell Stack Research at the Ford Motor Company, my advisor, James Waldecker, provided me with guidance, tutoring, and mentoring. In addition, his constructive criticism on my thesis and prior papers has been most helpful. I appreciate him for all kinds of help. His brilliance, enthusiasm, diligence, and great personality will inspire me throughout my career. I look forward to joining Ford and working with him soon.

Thanks also go to my labmate Toyoaki Matsuura for providing valuable discussions and a lot of important data for tuning my model.

Furthermore, I appreciate my committee members, Donald Siegel and Levi Thompson, for their efforts in reviewing and improving my thesis. This thesis would never have been finished without their guidance and help.

At this point, as I am finishing my Ph.D., I realize that my parents are getting old and I owe so much to them. Over the past eight years, they have given me the greatest freedom and let me pursue my dream on the opposite side of the world. I appreciate their understanding, support, and love in a way no words can express. I will take the best care of them so that I can feel better for my eight-year absence.

Finally, deep thanks go to my wife, Jingwen, and my son, Jonathan, for giving me a wonderful little family. I love you!

Table of Contents

List of Tables

Table

List of Figures

Figure

Abstract

The dead-ended anode (DEA) operation of a proton exchange membrane (PEM) fuel cell is a promising solution for applications with mild power density requirements. The hydrogen recirculation hardware can be simplified while maintaining high fuel utilization. The simplified system architecture for DEA operation reduces the cost. However, nitrogen and water accumulate in the anode, leading to decreasing voltage in galvanostatic operation due to local hydrogen depletion or starvation. Anode purging is thus necessary to release the accumulated nitrogen and water, and recover the voltage.

The thesis aims to optimize a DEA fuel cell by overcoming the disadvantages while maintaining the benefits. One of the major issues with local fuel starvation in DEA operation is the corrosion of the carbon that supports the platinum in the cathode catalyst layer, which dramatically reduces the durability. An along-channel and transient model has been developed to predict the carbon corrosion and associate irreversible voltage degradation in DEA operation. The carbon corrosion rate and voltage degradation were identified quantitatively after model tuning. Simulation results suggest that purge interval and cycle duration affect the spatiotemporal distribution of anode species and, therefore, the carbon corrosion rate in the opposite cathode; consequently, a model-based optimization of these two design variables were performed to achieve high lifetime efficiency of a DEA cell. There are three interrelated objectives in this optimization: the hydrogen loss during the purge, the average voltage output between the purges, and the voltage degradation due to the carbon corrosion. The simulation results show that the durability concern with DEA operation can be reduced when a systematic engineering optimization is performed. The highest lifetime efficiency is achieved with medium cycle duration and short purge interval. Finally, the focus was turned to DEA operation without purging, in which system equilibrium is observed under certain operating conditions. The criteria for achieving such a nitrogen-blanketing based equilibrium with reasonable power output were analyzed by solving the reduced-order model numerically and comparing with the full-order model simulation. The results suggest another way of operating a DEA cell with minimum requirements on power regulation and purge optimization.

Chapter 1
Introduction

A fuel cell is a device that generates electricity by a chemical reaction. Fuel cells have been utilized as an ideal power source for a variety of applications such as automotive and substitute batteries due to their significant advantages, i.e., high efficiency, low emission, silence and simplicity [1]. It is anticipated that fuel cells will eventually replace internal combustion engines in vehicular applications [2]. Among all kinds of fuel cells, the polymer electrolyte membrane (PEM) fuel cells, also known as proton exchange membrane fuel cells, is an ideal candidate for this purpose primarily due to its low operating temperature (60 °C- 90 °C) and fast start-up. The PEM fuel cell combines hydrogen and oxygen (from the air) to produce electricity, water, and heat. Hydrogen generation from renewable energy sources such as solar, wind, and waves or specialized geothermal energy, even if stored as compressed gas, can provide clean and high-density energy, offsetting current carbon-emitting practices.

The basic structure of the PEM fuel cell is shown in Fig. 1.1. The fuel and oxygen (air) are delivered across the active area through a series of channels. These channels are typically stamped into the electrically conductive backplanes so that the electrons can be transferred to the current collectors and an electric circuit is completed. The Gas Diffusion Layer (GDL), usually carbon paper or carbon cloth, is a porous material used to distribute the reactant gases from the channel to the catalyst surface. The GDL is also designed to promote the removal of product water from the catalyst area, by treatment of the carbon with a hydrophobic coating such as Teflon. The Catalyst Layer (CL) contains carbon-supported platinum as a catalyst and ionomer to facilitate the proton transport from the membrane. The CL is the place where the reaction takes place inside the fuel cell. A three-phase contact between protons, oxygen and electrons take places at the catalytic surface. Protons are transported through the proton conductive membrane material, usually perfluorinated sulfonic acid (PFSA), sandwiched between two CLs and two GDLs. Such a five-layered structure is called a membrane electrode assembly (MEA). Membranes are non-conductive to electrons, which are forced to travel through the external circuit to reach the cathode

and form the current. A thin Micro-Porous Layer (MPL) can also be inserted between the GDL and CL to increase the electrical contact and aid in water removal from the catalyst or membrane hydration [3].

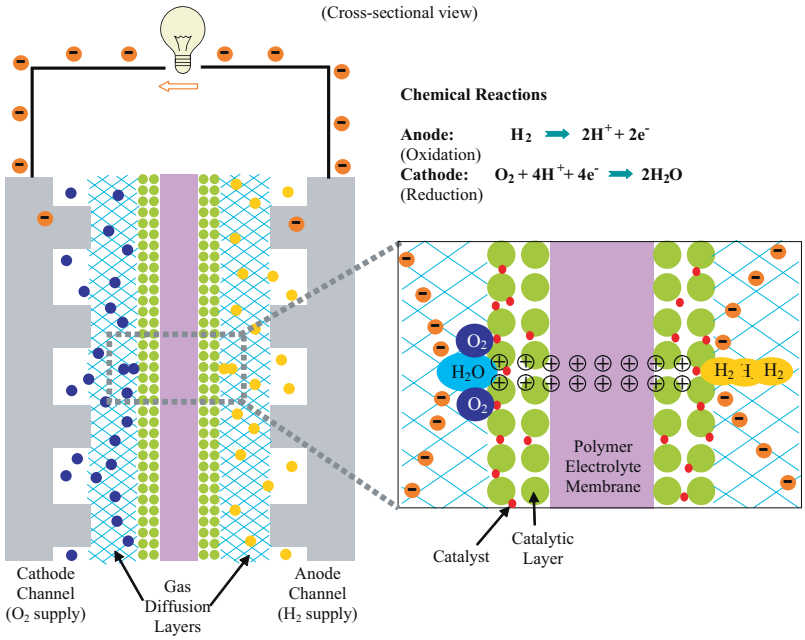

Figure 1.1 Schematic of a PEM fuel cell [4].

The PEM fuel cell was first commercially developed by General Electric in the 1960s for use by NASA on their first manned space vehicles [1]. Over the decades, there have been great technical advances in cost, performance and durability. For example, the early version of the PEMFC used in the NASA Gemini spacecraft had a lifetime of only about 500 h; that was, however, sufficient for those limited early missions. As a comparison, the DOE currently targets 5000 h for fuel cell lifetime in automotive applications [2]. Also, the early catalysts used 28 mg cm^{-2} of platinum. This high rate led to a widely held myth that platinum is a major contributor to the cost of a PEMFC. In recent years, the usage has been reduced to around 0.2 mg cm^{-2} with substantial power increase. At such loadings, the basic raw material cost of the platinum in a 1-kW PEMFC would be about $10, a small proportion of the total system cost ($47 in 2012 [5]).

1.1 Overview of Applications and Peer Technologies

The major application of PEM fuel cells (low temperature fuel cells) is in transportation due to the fast start-up/shutdown feature and zero emission of greenhouse gases. Major motor companies work solely with PEM fuel cells due to their high power density and excellent

dynamic characteristics. Fuel cell vehicles (FCVs) have been developed and demonstrated, e.g., GM Hydrogen 1, Ford Demo IIa (Focus), Daimler NeCar4a, Honda FCX-V3, Toyota FCHV, Nissan XTERRA FCV, VW Bora HyMotion, and Hyundai Santa Fe FCV [6]. Plans for commercializing FCVs by 2015 have been announced by Toyota, Honda, Hyudai, Daimler, and General Motors. Distributed PEM fuel cell power systems primarily focus on small-scale applications (50–250 kW for decentralized use or $<$10 kW for households). The high cost of PEM fuel cells in $/Kw, as compared to solid oxide fuel cell, remains a barrier that prohibits their wide application in residential power supply. Nevertheless, several auxiliary power units like Plug Power GenSys® and Ballard FCgen™ 1020 ACS fuel cell systems are deployed in many locations, particularly banks and telecommunication companies where the costs associated with power breakdowns are extremely high. Another promising application is in portable power supplies, since the fast-growing energy demand of modern portable devices such as laptops, cell phones and military radio/communication devices may be restricted by the energy capacity of batteries. The power supply from PEM fuel cell, in contrast, remains as long as hydrogen is available, although the feasibility greatly depends on the hydrogen storage technology. Major electronics companies, such as Toshiba, Sony, Motorola, LG, and Samsung, have in-house research and development units for portable fuel cells [6].

Generally, size, weight, and thermal and water management are barriers to the commercialization of low-temperature fuel cell technology [7]. In transportation applications, these technologies face more stringent cost and durability hurdles. The cost of fuel cell power systems must be reduced before they can be competitive with conventional technologies. For example, the costs for internal combustion engine power plants are about $25–$35/kW; for transportation applications, a fuel cell system needs to cost $30/kW for the technology to be competitive. The DOE Hydrogen and Fuel Cells Program Record shows that the cost of an 80-kW automotive PEM fuel cell system based on 2011 technology and operating on direct hydrogen is projected to be $49/kW, in which the Balance of Plant (BOP) contributes $26/kW [8]. Although the durability of fuel cell systems has not been established for transportation applications, they will be naturally required to achieve the same level of durability and reliability as current automotive engines, i.e., 5,000-hour lifespan and the ability to function over the full range of vehicle operating conditions (subzero to ambient temperatures) [7].

As a comparison, the major applications of medium- and high-temperature fuel cells, primarily molten carbonate fuel cells (MCFC) and solid oxide fuel cells (SOFC), focus on stationary power generation systems. These fuel cells are typically part of a combined heat and power (CHP) system since the high temperature exit gases and cooling fluids are a

valuable source of heat for nearby buildings, processes, and facilities. One representative application is in fuel cell/gas turbine hybrid system as the high-temperature exit gases and cooling fluids can be used to drive turbines that can drive generators, producing further electricity [1]. One major advantage over the low-temperature fuel cell is that the electrochemical reactions proceed much more quickly, and, therefore, noble metal catalysts are usually not needed. Furthermore, the temperatures are high enough to facilitate the extraction of hydrogen from other, more readily available fuels (typically natural gas) by on-site reforming. These high-temperature fuel cells, however, can rarely be used in transportation applications.

1.1.1 Peer Technology – Redox Flow Battery

In grid-scale applications, researchers and engineers have focused on a variety of sustainable power-generation and energy-storage technologies that may be advantageous in both cost and durability. Essentially, a fuel cell is solely a power-generation device, which requires separate energy (hydrogen) storage units to support uninterrupted reaction. The consumption of hydrogen is not a reversible process within the fuel cell, and the optimization of hydrogen storage subsystem becomes critical to reduce the size and cost of the whole fuel cell system. Advancements in fuel cell and hydrogen storage technologies have to be coupled. Therefore, in stationary applications such as grid-scale energy storage, fuel cell system is not the first option for both cost and durability. A redox flow battery (RFB) as state-of-the-art power-generation and energy-storage device becomes a promising candidate.

RFBs are attractive for grid-scale energy storage to level out the energy fluctuation from renewable resources such as wind and solar energies, due to their primary advantages of flexible layout (separation of power and energy components), rapid response, zero emission, and high efficiency [9]. RFBs utilize the redox states of various chemical couples to cycle between charge and discharge efficiently; typical couples including iron-chromium, all-vanadium and zinc-bromine. Extensive research and development have been performed on RFB systems to improve performance and durability and to reduce cost, with an ultimate goal of wide application in grid-scale energy storage [9, 10, 11]. The all-vanadium system perhaps is closest to commercialization among all types of RFBs. For example, in China, which owns 11.6% of world's vanadium resources, commercial all-vanadium RFB systems up to 100KW/200KWh have been used in national grids since 2009 [12, 13]. The high material cost for vanadium RFB, unfortunately, does not lead to satisfactory power density and efficiency, restricting its wide-spread adoption. A hydrogen/bromine system was thus

proposed since the reactants are earth-abundant and inexpensive, and, as shown recently at Lawrence Berkeley National Laboratory (LBNL), high performance with high efficiency is obtainable [14]. Nevertheless, it is essential to show that high performance and efficiency are still achievable at a stack level with H_2/Br_2 system while maintaining competitive capital and cycle life costs [15]. In the H_2/Br_2 system, the durability concern is changed since it is unnecessary to apply Pt in the cathode; a porous carbon electrode leads to satisfactory performance due to the fast kinetics of bromine reduction in the cathode [14]. In the charging cycle, however, the carbon and Pt may still experience degradation since the anode potential could be increased to beyond 1 V depending on the charge rate. In addition, there exists an instability of the cell coming from the absorption of bromide on the anode platinum (i.e., Pt poisoning) [16], so that development of a membrane with low crossover of bromide is underway at LBNL [17].

1.1.2 Peer Technology – ACAL Fuel Cell System

ACAL Energy Ltd. in the UK has developed low-cost PEM fuel cell systems powered by the company's proprietary FlowCath® platinum-free, liquid cathode technology [18]. The concept of FlowCath® was proposed in 2008, and their 1-3 KW demonstrators were developed and optimized in 2010. Their innovative design is still under active research and improvement, with a goal of commercialization initially in small stationary power and ultimately in automotive applications. Their system is essentially a fuel cell but shares a H_2/Br_2 RFB feature of cathode solution-based recirculation. Therefore, we still regard it as a peer to the traditional fuel cell system that typically applies anode recirculation.

The basis of the FlowCath® technology is that an aqueous solution-based redox approach is used for the cathode, instead of oxygen. A system schematic is shown in Fig. 1.2. The cell consists of an anode flow field, electrode and membrane which are very similar to the conventional anode and membrane. The difference is on the cathode side, where there is no conventional Pt/C catalyst. Instead, the membrane is in contact with the aqueous solution, called the catholyte solution. The solution passes through a porous electrode, a typical electrode material being carbon. The solution contains dissolved species which carry out the redox processes. The mediator is initially oxidized on entry into the cell and is reduced at the electrode. A proton migrates from the membrane to balance the charge as the mediator takes on an electron. The solution is circulated to a regenerator, where the mediator is reoxidized, and oxygen from air is brought into contact with the solution. A soluble catalyst reacts with the oxygen and protons to oxidize the mediator and form the water.

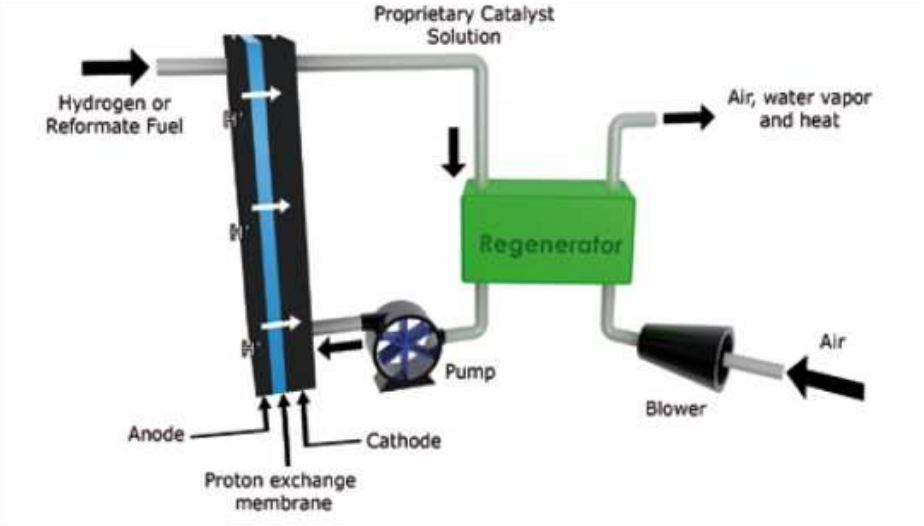

Figure 1.2 Schematic diagram of the ACAL energy fuel cell technology [18].

In a conventional PEM fuel cell, peroxide formed under certain operating conditions can dissolve Pt, and also damage the membrane. Crossover oxygen to the anode can also produce similar damaging effects on the electrode and membrane [19, 20]. In an ACAL system, the reaction between catalyst, mediator and oxygen occurs in the regenerator; thus, peroxy species can not contact the membrane or electrode. In addition, oxygen is consumed by the catholyte without any crossover to the anode. As the catholyte is always in contact with the membrane, the hydration is controlled by the catholyte. The membrane no longer experiences any RH cycling as in a conventional PEM fuel cell. There is no Pt in the cathode; instead, the polyoxometallate family based on vanadomolybdates is the catalyst for oxidizing the mediator. For these reasons, an ACAL system exhibits a durability advantage that conventional PEM fuel cell technology can hardly achieve. Moreover, the flowing catholyte acts a cooling circuit; hence, extra cooling is not required.

Although the system has demonstrated advantages for small stationary applications, the cost of reliability in automotive applications, particularly when the power requirement is scaled up, is still unclear. The durability of the membrane and electrode is improved; however, the degradation of the catholyte and sealing material could be a concern.

1.2 Dead-Ended Anode (DEA) vs. Flow-Through Anode (FTA)

Flow-through operations are used on both the anode and cathode of most laboratory or experimental hydrogen PEM fuel cell systems. However, the fuel utilization of a flow-

through anode (FTA) operation is too low for commercial system, which normally uses a re-circulation anode (RCA) to re-cycle excess hydrogen back through the fuel cell stack so that the fuel utilization is increased. The RCA, shown in Fig. 1.3a, requires hydrogen-grade plumbing and hardware such as an ejector/blower, water separator, and hydrogen humidification. Water must be removed from the gas exiting the anode before it goes to the ejector and then the dry fuel supplied to the anode must be re-humidified to prevent over-drying of the membrane. These BOP components are necessary but add weight, volume, and expense to the system [21, 8].

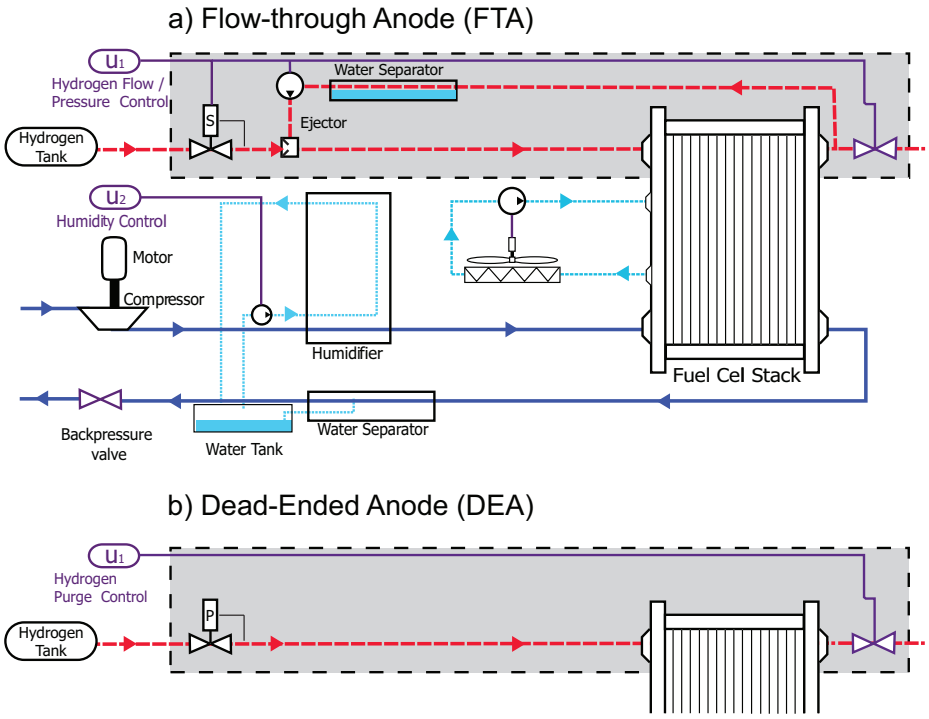

Figure 1.3 Schematic of fuel cell systems with a flow-through anode versus a dead-ended anode. A DEA operation depends on upstream pressure regulation instead of mass flow control. If the purge interval is minimized, there is less need for hydrogen re-circulation and humidification systems.

Although the RCA subsystem can remove water from the gas stream, purging is still required to handle the nitrogen. The membrane is not an ideal seperator, and a small amount of nitrogen can cross through, driven by the gradient in partial pressure from the cathode air. Over time, this nitrogen accumulates in the anode feed system, which dilutes the hydrogen fuel in the anode [22]. The dilution of H_2 lowers the fuel cell terminal voltage, and hence the thermodynamic efficiency.

In order to reduce the BOP components and simplify the system, a dead-ended anode (DEA) operation of a fuel cell system was proposed and implemented. In a DEA system shown in Fig. 1.3b, anode pressure is regulated to supply exactly the amount hydrogen needed to support the reaction (anode stoichiometry ratio one). Unlike a RCA, the DEA

operation cannot tolerate anode inlet humidification, which would lead to flooding since the water is not removed by the hydrogen flow. The use of a pressure regulator, instead of a mass flow controller, and the removal of hydrogen ejector or blower and anode inlet humidification yields a system with lower cost and volume.

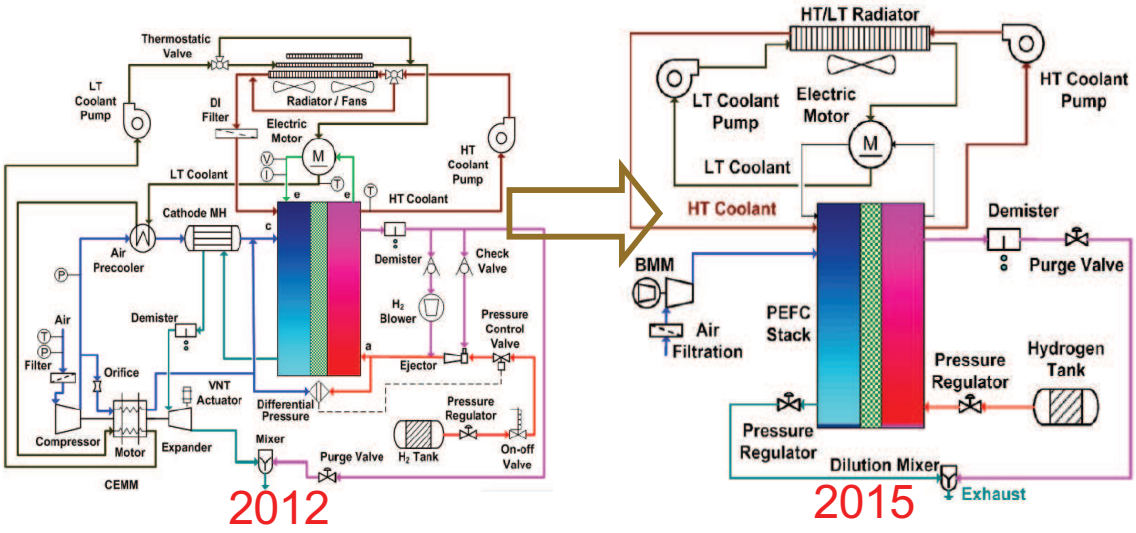

Figure 1.4 Schematic of fuel cell systems proposed by Argonne National Laboratory. A DEA system architecture is expected in 2015 [21].

Figure 1.4 schematically shows the fuel cell systems proposed by Argonne National Laboratory. Comparing the present system in 2012 and a future system in 2015, one can observe that the BOP components, which may take up to 50% of the whole system cost [21], have been greatly reduced. Noticeably, the system in 2015 is exactly a DEA fuel cell system without cathode pressurization. The ejector, blower, and control valve in the anode have been replaced by simply a pressure regulator so that the system cost is reduced. In order to meet the power density requirement for automotive applications, the negative influences on power density from the removal of cathode pressurization and application of DEA architecture need to be minimized. Therefore, advances in both membrane and catalyst technologies are necessary. For example, the future availability of high-temperature electrolyte that does not require that the feed gases be humidified is essential [21].

Similar to the RCA system discussed above, nitrogen and water crossover is a concern in DEA operation. The nitrogen is pushed toward the end of the channel, by the hydrogen flow, where it accumulates. The accumulating N_2 forms a blanket, which completely displaces hydrogen from reaching the catalyst layer, effectively shutting down the power production from the affected region of the cell [23]. Water vapor gradients between the humidified cathode and the dry-fed anode also drive excess water into the anode, which can cause the presence of not only vapor but also liquid water in the CL, GDL, and channel.

The two-phase flow scenario in fuel cell is considered to give complexity in modeling [24] and will be discussed in more detail in Chapter 3. Unlike water vapor whose maximum partial volume is dictated by temperature, liquid can fill the entire free space in the channels, which is referred to as channel plugging.

Due to the nitrogen blanketing and water plugging, the fuel cell terminal voltage decreases with time in galvanostatic DEA operation. To avoid extremely low voltage, an anode purge is necessary to release the accumulated nitrogen and water and to recover the terminal voltage as shown in Fig. 1.5. The voltage threshold for purging the anode depends on specific application. Generally, frequent purging leads to quasi-flow-through operations that may dry the membrane and waste hydrogen, whereas over-delaying a purge gives very small voltage and low thermodynamic efficiency. The purge is implemented by actuating the solenoid valve at the downstream of anode for a certain period. The purge interval is thus controllable, and it is an important control factor to the system efficiency with a detailed discussion in Chapter 3. The evolution of voltage as well as species distribution is very repeatable between two consecutive purges. The repeatable behavior is termed as a cycle in the DEA operation.

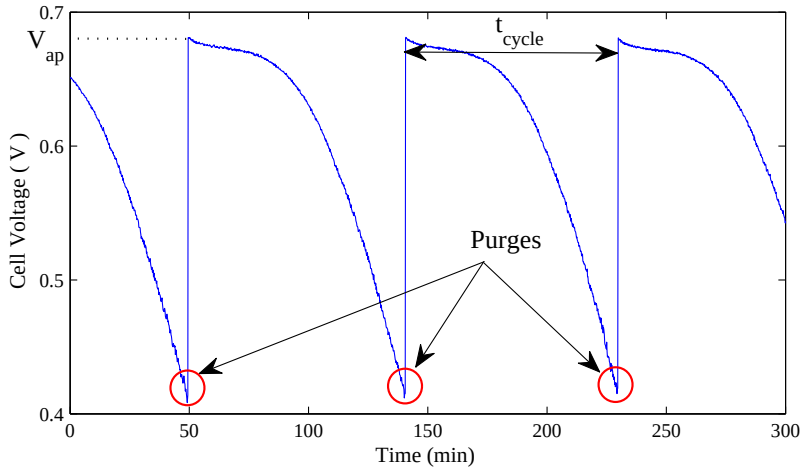

Figure 1.5 Typical voltage evolution during the DEA operation. A purge releases the accumulated nitrogen and water, thereby recovering the voltage. The voltage evolution is very repeatable between two consecutive purges.

1.2.1 Power Density

Due to the nitrogen blanketing and water plugging in the anode which dilutes the hydrogen, the power density of a DEA cell is typically smaller than a flow-through one as shown in Fig. 1.6. Note that the data [25] come from traditional Pt/C catalyst and membrane tech-

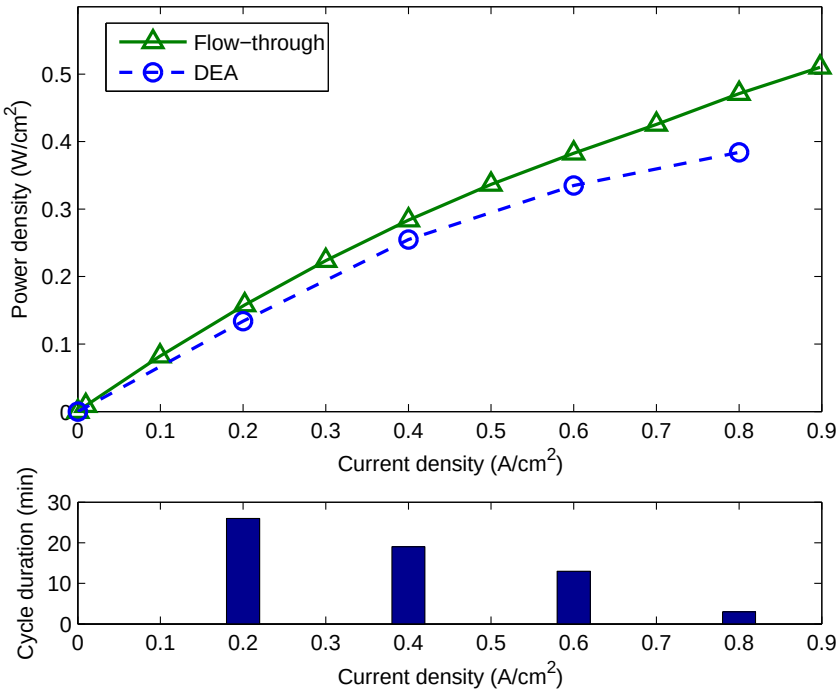

Figure 1.6 The upper subplot shows the power density under a DEA and a flow-through condition from the experiments. For the DEA condition, the cathode supply RH is 100%, cell temperature 60°C, cathode/anode pressure 4.0 psig, and cathode stoichiometry ratio 2.5. The purging was triggered when the voltage reduced to 0.4 V. For the flow-through condition, the cathode/anode supply RH is 100%, cell temperature is 60°C, cathode/anode pressures are 2.5 psig, and anode/cathode stoichiometry ratios are 1.2/2.5. The lower subplot shows the cycle duration for each current load.

nologies; namely, innovations in MEA components that can improve the cell performance under DEA conditions are not considered. As the current density increases, the power density difference between DEA and flow-through conditions enlarges, and the cycle duration of the DEA operation decreases. When the current density is 0.8 A/cm^2, the cycle duration is only 3 min. Although increasing current load appears to improve the power density of a DEA cell, the associated frequent purge leads to substantial amounts of hydrogen loss. Thus, the DEA operation with a higher current load is akin to a flow-through scenario, thereby achieving a larger power density in the range that has been tested with undesired hydrogen loss. Despite the low power density, the DEA system is still attractive in a variety of applications with mild requirement on power density, e.g., auxiliary power units, with the Ballard Nexa fuel cell module being one of the commercial products. Although one approach is the ongoing innovation in MEA components which can increase the power density under DEA conditions, control-oriented modeling and optimization of a DEA fuel cell are also essential for its current applications.

1.3 PEM Fuel Cell Degradation

The degradation of PEM fuel cell components results in performance decay in power output and even system failure. It is generally accepted that all components including the membrane, catalyst layer, gas diffusion layer, sealing gasket and bipolar plate are subject to degradation [26]. The degradation of GDL usually refers to the hydrophobicity loss due to the prolonged exposure of the carbon to the oxidative environment which leads to the formation of carboxyl groups or phenols [27, 28]. The surface of GDL then becomes more hydrophilic and the mass transport loss increases. Nowadays, the bipolar plate is usually made of Al, Ti, Ni, alloys thereof, or stainless steel due to their good electrical conductivities and mechanical properties. The degradation usually refers to the oxide films formed on the surfaces of these metallic plates and the corrosion of the stainless steel plate in the corrosive acid and wet environment, both leading to enhanced contact resistance [29]. Compared with those components, the degradation of electrolyte membrane and Pt/C catalyst is most important because it leads to significant performance decay or even abrupt failure of the cell.

1.3.1 Catalyst Layer Degradation

The catalyst degradation usually pertains to the loss of active Pt surface area, which could be attributed to several reasons including but not limited to sintering or migration of Pt particles, detachment and dissolution of Pt into electrolyte, and corrosion of the carbon support. The well-known Ostwald ripening [30] suggests that small Pt particles may dissolve in the ionomer phase and then re-deposit on the carbon surface. The dissolution of Pt in the ionomer phase may also dramatically degrade the membrane, because reduction of Pt ions by the crossover hydrogen leads to the precipitation in the membrane [31]. On the other hand, the random cluster-cluster collision of Pt particles on the carbon supports may also lead to agglomeration [32], which reduces the active catalytic surface area. Generally, it is accepted that the electrode potential, current density, membrane water content, operating temperature and cycling conditions would determine the rate and dominant mechanism of Pt particle growth [26]. Mathematical models suggest that the oxide layer can protect Pt from dissolution [33, 34]. However, the kinetics of oxide formation are much slower than dissolution; hence, the real effect of oxide coverage is difficult to identify experimentally.

Support carbon corrosion is another important phenomenon pertaining to catalyst layer degradation. It is generally caused by the elevated interfacial potential ($>$0.8 V) between the membrane phase and the metal phase. The elevated potential can be observed during

the startup/shutdown process of the cell due to the formation of H_2/O_2 boundary in the anode [35, 36]. As shown in Fig. 1.7, the local interfacial potential between membrane phase and metal phase at region D is dramatically increased to ~1.6 V. Therefore, support carbon is subject to oxidization and water dissociation may also occur. Nevertheless, under typical operating temperature (65 °C) and interfacial potential (0.6 V), the carbon corrosion rate is negligible [35].

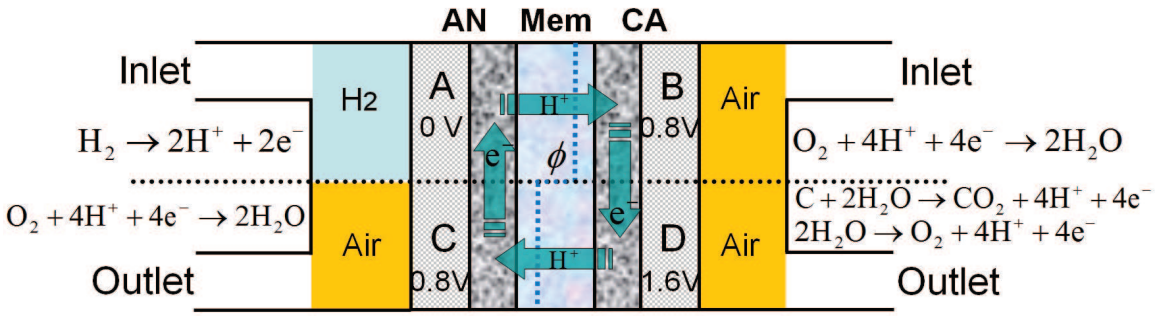

Figure 1.7 Schematic of the carbon corrosion mechanism due to the clear H_2/O_2 boundary, which usually forms during start-up/shutdown of the cell [35, 37].

It is found that, with the presence of electrocatalysts such as Pt, the required potential for carbon corrosion may be reduced to 0.55 V, with respect to reversible hydrogen electrode (RHE), or lower [38]. The exact threshold potential value may depend on the catalyst property and other operating conditions.

Similar to the start-up/shutdown case, local fuel starvation in the anode can result in high interfacial potential and carbon corrosion. In DEA operation, it is the fuel depletion or starvation which significantly affects the durability. The actual degradation scenario is quite complicated due to the mutual influences: the loss of carbon leads to agglomeration of Pt particles and the loss of catalytic surface area reduces the kinetics of carbon corrosion.

1.3.2 Degradation during DEA Operation

In DEA operation, both membrane and catalyst layer degradations have been observed experimentally in our extended DEA fuel cell testing under 0.4 A cm^{-2}current, 100% cathode supply RH and 60 °C cell temperature [39]. As shown in Fig. 1.8, substantial catalyst layer thinning had been observed at the cathode outlet region, whereas the membrane delamination with the catalyst layer observed at the inlet region. Pin-hole failure of the membrane was also identified by the low open circuit voltage (OCV) and substantial hydrogen crossover.

As the carbon occupies the majority of catalyst layer volume, the observed catalyst layer thinning can be interpreted as carbon corrosion at the cathode outlet region, followed

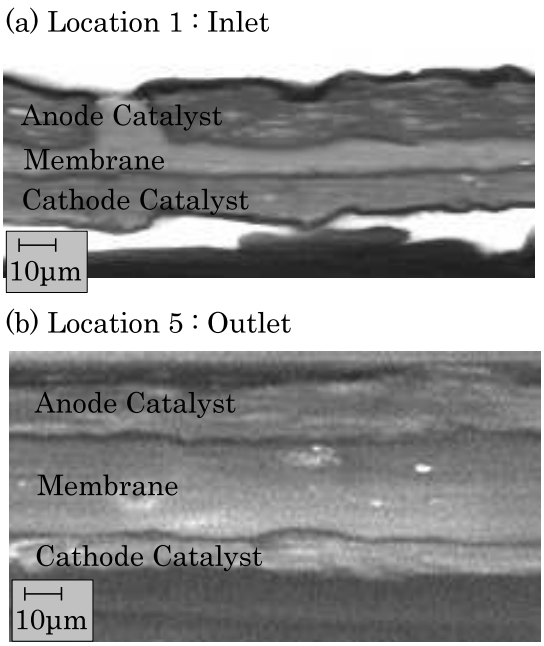

Figure 1.8 Representative SEM image of the MEA cross-section in an aged DEA cell [39]. The inlet region shows membrane thinning whereas the outlet region shows cathode catalyst layer thinning.

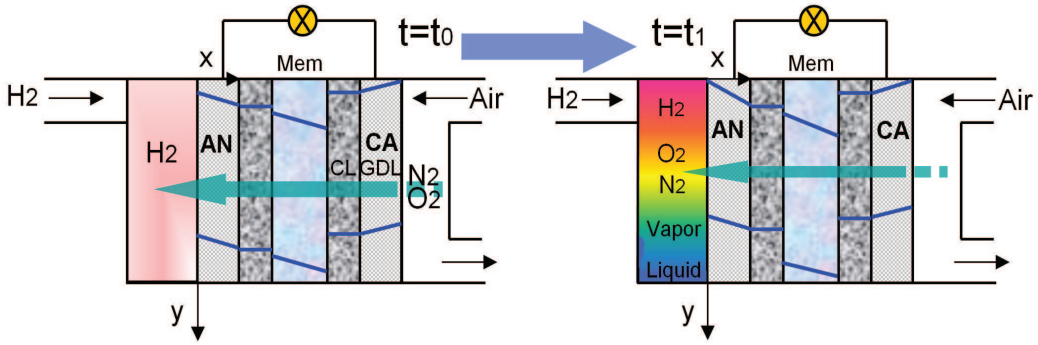

Figure 1.9 The spatiotemporal evolution of species distribution in the anode during DEA operation (not to scale).

by collapse of the porous structure. The spatiotemporal evolution of species in the anode during DEA operation is schematically shown in Fig. 1.9. With the accumulation of nitrogen and water, the fuel depletes along the anode channel as time evolves, and it is the channel-end region that shows the most severe fuel starvation. Correspondingly, the cathode outlet region bears highest interfacial potential and carbon corrosion rate.

During extended DEA operation, the membrane degradation tends to occur in the inlet region [39, 25]. The observation of membrane thinning at the inlet region can be probably explained by the dry fuel supply, since low gas RH and membrane water content accelerate

both the chemical decomposition [40, 41] and physical dissolution [42]. In DEA operation, liquid water accumulates in the channel end region with the front propagating towards the inlet region that is in contact with dry fuel. A purge, however, clears the water in the channel, after which the membrane in the inlet region is being dried until substantial water has accumulated again. Such RH cycling on the membrane in the inlet/middle region along the channel, together with the high local current, tends to trigger membrane crack, delamination, and/or pin-hole failure. Note that the local current distribution is uneven with the inlet region much higher than the outlet region, due to the fuel depletion along the channel. For example, in a DEA operation with a 0.2 A cm^{-2} current load, the local current reaches as high as 0.38 A cm^{-2} in the inlet region whereas it decreases to zero at the channel-end region as shown in Fig. 4.7.

The spatiotemporal evolution of species, membrane water content and local current results in more severe degradation in a DEA fuel cell as compared to a RCA one. The DEA architecture simplifies the system and reduces the cost, but needs to handle the stringent durability issue. This scenario is not unusual in an engineering innovation. It is anticipated that an engineering optimization of the purging scheme can reduce or eliminate the durability concern in DEA operation while maintaining its benefits.

1.4 Methodologies

In this dissertation work, modeling and simulation are the primary methodologies. Fuel cell models are used to understand and predict fuel cell behavior. Simple models can explain the basic trends, e.g., how cell voltage changes when temperature increases or pressure decreases. Sophisticated models can guide the engineering design, e.g., what happens when the gas diffusion layer thickness is reduced from 500 to 100 μm. Some of the operating parameters that interest fuel cell engineers are difficult to measure. For example, special sensors and/or circuits must be utilized/designed to measure the local current density and temperature [43, 44, 45]; in-situ measurement of membrane water content generally requires neutron imaging [46] or magnetic resonance imaging (MRI) techniques [47]. Under such circumstances, fuel cell modeling provides a more convenient way to investigate these parameters from a physics-based approach. The modeling results can, in turn, guide the experimental design. Since all fuel cell models incorporate assumptions, validation against experimental data is required to verify fidelity. The validation can be either direct or indirect, meaning that a readily measurable parameter, such as the terminal voltage, is usually used for comparison with the corresponding model output.

1.4.1 Computational Fluid Dynamics Modeling

The computational fluid dynamics (CFD) numerical method has been extensively developed to simulate fuel cell behavior since the early 1990s. Modern fuel cell models are generally CFD-based so that detailed investigation and visualization of transport phenomena, including mass, charge and heat, can be achieved. Pioneer modeling efforts by Bernardi and Vebrunge [48] and Springer et al. [49] are fundamental to understand PEM fuel cells. They both developed a one-dimensional, isothermal model of the MEA. Bernardi and Vebrunge focused on the net water flux through the membrane whereas Springer et al. studied the membrane hydration. Fuller and Newman [50] developed a two-dimensional (2D) model to study the water and thermal management. Their model uses concentrated solutions theory for transport in the membrane. Nguyen and White [51] studied the effects of gas humidification on cell performance and reported that back diffusion of water from the cathode to anode is insufficient to keep the membrane hydrated at high current density. They consequently concluded that the fuel and oxidant should both be humidified for satisfactory performance.

More recently, Gurau et al. [52] developed the first real 2D model for the flow channels and MEA. This along-the-channel model studied the effects of composition change of the reactants. Um et al. [53] developed a 2D transient, along-the-channel model to study the evolution of current density with changing cell potential. Um and Wang [54] extended the work to the third dimension and also studied the effects of flow channel geometry and layout. Wang's group at Pennsylvania State University developed a large-scale CFD model [55, 56] and started to model the two-phase transport in the fuel cells [57, 58]. The two-phase transport in fuel cell is critical to water management and hence is under extensive numerical study. Two-phase flow behavior has been investigated in different fuel cell regions: catalyst layer and GDL [57, 59, 60], and flow channels [61]. In recent years, the fuel cell modeling has extended to multi-dimensional and multi-phase framework to study the more complicated physical and electrochemical processes in the fuel cell. For example, a three-dimensional and multi-phase model has been developed to simulate the cold start processes in a PEM fuel cell [62, 63]. The effects of water freezing in the membrane electrolyte, non-equilibrium mass transfer in the catalyst layer, and operating conditions on the success of cold start were investigated.

The advances in modeling have led to more thorough presentations of the electrochemical reaction and transport phenomenon, and more accurate prediction of the fuel cell performance. Meanwhile, more demanding computational resources are required. Normally, only a section of the entire cell is considered in a 3D approach due to the computational requirement [64]. The trade-off between model accuracy and computational

complexity is a difficult engineering challenge for most PEMFC research and development.

1.4.2 Control-Oriented Modeling

In this dissertation, a 1+1D (along-channel+through-membrane), isothermal, transient and two-phase model has been developed to estimate the cell lifetime and perform the purge optimization. Due to the along-channel stratified patterns in the DEA operation and the vertical orientation of the DEA cell, multi-dimensional modeling is not necessary to capture the voltage behavior and species distribution along the channel. The extensive computational resources needed to simulate multi-dimensional model are not suitable for control-oriented applications. One ultimate goal of this work is to control the purging cycle to reduce degradation and maximize efficiency. The 1+1D approach is a good compromise between model complexity and accuracy since the local current density captures some of the along the channel effects without increasing the computational complexity. The modeling of water transport through the GDL to the anode channel completes the along-channel model framework with some accuracy, as the transport of two-phase flow within the porous GDL is captured in only one dimension. The liquid accumulation in the anode channel is finally modeled by tracking the liquid volume fraction along the channel. Another benefit of the reduced-dimension modeling is that the water transport and voltage submodel can be parameterized easily using analytical tools, as shown in a prior publication from our group [65].

The model in this dissertation is developed based on the prior framework by Siegel et al. [66, 65], which captures the nitrogen front evolution via a 1D along-channel model and liquid accumulation via a lumped-channel approach. The model prediction agrees well with the experimental data [67]. The present model captures the liquid transport and accumulation via a distributed-channel approach together with the 1+1D feature connecting the channel and GDL. Modeling the liquid distribution in the channel is necessary to predict the purge flow and hydrogen loss accurately. The carbon corrosion kinetics are also incorporated to predict the voltage degradation, which requires the anode distribution of an additional species, oxygen, to be modeled. The membrane degradation and Pt dissolution are not considered in the model in order to avoid too many states and parameters subject to tuning. Nevertheless, the model is used under conditions with minimum membrane degradation, and the loss of active catalytic sites is assumed to be proportional to the remaining carbon mass as compared to the original mass (see Chapter 2). The tuned model can capture the voltage degradation in DEA operation with satisfactory accuracy, as shown in Chapter 3.

1.5 Summary of Contributions

Based on the prior framework, the DEA model has been extended to capture the carbon corrosion behavior. To accurately account for the liquid water crossover and accumulation in the anode, a distributed 1+1D (along-channel+through-membrane) and two-phase model framework has been finally reached. The model has been tuned using experimental data of along-channel species distribution, liquid water mass in the anode, and voltage evolution within a cycle and voltage degradation over multiple cycles. Three groups of parameters, i.e., the species transport, the reaction kinetics, and the carbon corrosion related parameters, have been tuned. The tuned model shows predictability on specie distribution and cell voltage in wider ranges of current and cathode supply RH.

The present model is used for evaluation of a DEA cell such as in hydrogen utilization, durability, and efficiency. It can also be incorporated into a system-level model including BOP components to examine system performance and cost.

The lifetime simulation of a DEA cell has been performed for the first time to capture the voltage degradation in both multiple DEA cycles with purging and DEA equilibrium operation without purging. The simulation represents an alternative way to study fuel cell durability with little experimentation requirement, as compared to accelerated stress testing (AST) which is a general approach [26, 2]. In addition, lifetime simulation captures the actual degradation mechanism in the fuel cell operation whereas AST cannot. It is designed to test the material properties in an accelerated manner.

The feasibility of DEA operations has been confirmed by showing that a satisfactory lifetime efficiency can be achieved by purge scheduling. Alternatively stated, the negative influences from cathode carbon corrosion and hydrogen loss during the purge are limited with careful purge scheduling. The reduced system complexity and cost for DEA fuel cell become more attractive when the degradation problem is resolved.

Finally, the existence of an equilibrium in DEA operation has been identified. Operating a DEA cell under equilibrium is possible, which features minimum requirements on power regulation hardware and purge optimization efforts, as long as the degradation due to the extended operation under fuel starvation can be alleviated by novel cell design.

1.6 Thesis Organization

As discussed in Section 1.3, DEA architecture simplifies the system and reduces the cost, but introduces a potential degradation issue. Motivated by this fact, the model was developed to quantify the degradation rate and identify the influences of design/operating

parameters on the degradation. Finally, it is aimed to develop the control strategy that can reduce the degradation in DEA operations. For this purpose, the carbon corrosion due to DEA operation will be discussed in Chapter 2 of the thesis, which primarily comes from our paper entitled 'Carbon Corrosion in PEM Fuel Cell Dead-Ended Anode Operations' and published in the *Journal of the Electrochemical Society* [68]. The model has been tuned against the species concentration in the anode channel and the voltage evolution within a cycle (Section 2.6).

The modeling results lead to a general conclusion that, to minimize the cathode carbon corrosion, the purge should be scheduled before the fuel starvation occurs in the anode channel-end region. A short cycle duration or frequent purging is therefore preferred for reducing degradation. Such purge scheduling tends to make the DEA operation akin to flow-through mode, and there is unavoidable hydrogen loss during the purge. Since high hydrogen utilization is another benefit of DEA operation, it is of interest to elucidate the trade-off between degradation and hydrogen loss. To this end, the DEA cell lifetime efficiency is defined to study the impacts from two design variables, purge interval and cycle duration, in DEA operation. This optimization of lifetime efficiency becomes Chapter 3 of the thesis, which is primarily from our paper 'Optimization of Purge Cycle for Dead-Ended Anode Fuel Cell Operation' published in the *International Journal of Hydrogen Energy* [69]. The model has been extended to capture the liquid water transport and accumulation in the DEA cell, so that the purge flow can be predicted more accurately. The model is further tuned against the liquid water mass in the anode channel and the voltage degradation over cycling (Section 3.4).

Finally, the purge optimization motivated a further consideration of disabling the purge, namely, whether the decreasing voltage with the purge disabled eventually evolves toward a shutdown or an equilibrium of the DEA cell, and what are the operating conditions for reaching that equilibrium. The tuned model is used to identify the existence of equilibrium and to investigate the characteristics of equilibrium. The DEA system can be operated under equilibrium if the power output is reasonable, so that the necessity of power regulation and efforts in purge optimization can be greatly reduced. This study is Chapter 4 of the thesis, primarily from our paper 'Experimental Validation of Equilibria in Fuel Cells with Dead-Ended Anodes' presented at the European Control Conference 2013 [70]. The modeling results of voltage evolution toward equilibrium and degradation under equilibrium are validated with the experimental data (Section 4.5). The dissertation will end with conclusions and recommendations.

1.7 Nomenclature

The nomenclature of the thesis is summarized in the following two tables.

Table 1.1 Table of nomenclature

Local current density	$i, A\ cm^{-2}$
Average current density	$i_{fc}, A\ cm^{-2}$
Number of cycles	k
Scale factor for oxygen/nitrogen permeance	k_{O_2/N_2}
Time	$t, second$
Mass	$m, g\ cm^2$
Channel length	l, cm
Channel width	w, cm
Channel depth	h, cm
Molar fraction	n
Radius of agglomerate	$r_{agg}, \mu m$
Reactive/Crossover flux (through membrane) per unit depth	$r, mol\ m^{-3}s^{-1}$
Liquid water volume fraction	s
Tunable power factor for remaining carbon	q
Gas velocity	$u, m\ s^{-1}$
Convective velocity	$v, m\ s^{-1}$
Diffusivity	$D, m^2\ s^{-1}$
Cell voltage	E_{cell}, V
Faraday's constant	$F, C\ mol^{-1}$
Catalyst/Carbon loading	$L, g\ cm^2$
Molar fraction	M
Total gas flux (along channel)	$N_t, mol\ m^{-2}s^{-1}$
Henry's law constant	$H, L\ ATM\ mol^{-1}$
Diffusive flux (along channel)	$J, mol\ m^{-2}s^{-1}$
Gas permeance	$K, mol\ m^{-1}s^{-1}Pa^{-1}$
Gas constant	$R, J\ K^{-1}mol^{-1}$
Temperature	T, K
Pressure	P, Pa
Hydrogen amount	$Q, mole$
Gas constant	$R, J\ K^{-1}mol^{-1}$
Area	S, cm^2
Metal phase potential	V_m, V
Coefficient matrix in Stefan-Maxwell diffusion (Chapter 2)	W
Volumetric flow rate (Chapter 3)	W, m^3s^{-1}

Table 1.2 Table of nomenclature cont.

Greek	
Transfer coefficient	α
Tunable parameter for hydrogen reaction	β
Electrochemical area	$\gamma, cm^2\ g^{-1}$
Membrane water content	λ
Kinematic viscosity	$\nu, m^2 s^{-1}$
Efficiency (Chapter 3)	η
Over-potential (The other chapters)	η, V
Membrane phase potential	ϕ, V
Scaler function in Stefan-Maxwell diffusion	ψ
Porosity (Section 2.4.1)	ε
Effective factor for remaining carbon (elsewhere)	ε
Thickness of ionomer film	$\delta, \mu m$
Shorthand/Subscript/Superscript	
Anode	AN
Balance of plant	BOP
Cathode	CA
Flow channel	CH
Full-order model	FOM
Catalyst layer	CL
Dead-ended anode	DEA
Gas diffusion layer	GDL
Flow-through	FT
Fuel cell	FC
Membrane	MEM
Operating condition	OPC
Relative humidity	$RH = P_V / P_{sat}$
Reduced-order model	ROM
Saturation	sat
Stoichiometry ratio	SR

Chapter 2

Carbon corrosion in PEM fuel cell dead-ended anode operations

In the DEA operation, the fuel depletion or even starvation in the anode due to the nitrogen blanketing and water plugging can result in carbon corrosion in the cathode. To evaluate the overall performance of a DEA fuel cell as compared to a recirculation anode fuel cell, the durability should be considered in addition to the power output and hydrogen utilization.

This chapter investigates the effects of DEA operation on the electrode carbon corrosion of the PEM fuel cell. A reduced order isothermal model is developed focusing on the species concentration along the channel and associated membrane phase potential. This model explains, and can be used to quantify, the carbon corrosion behavior during DEA operation of a PEM fuel cell. The presence of oxygen in the anode channel, although normally less than 5% in molar fraction, creates a H_2/O_2 front as N_2 and water accumulate at the end of the channel and hydrogen is depleted along the channel. The presence of oxygen in the anode channel also results in a gradual drop of the membrane phase potential, promoting carbon corrosion in the cathode. The corrosion rate is driven by the local species concentration in the anode, which varies in space and time. In a co-flow configuration, the large spatiotemporal patterns of hydrogen starvation in the end of the anode channel induce the highest carbon corrosion, which, in turn, is shown to be moderated by the decreasing terminal voltage during galvanostatic operation. Although not fully calibrated, the model shows good agreement with preliminary in situ observations.

2.1 Introduction

The simplified balance of plant (BOP) and enhanced hydrogen utilization in the DEA operation unfortunately come with a major concern. The accumulation of nitrogen and liquid water in the anode channel during DEA operation may lead to local fuel depletion or starvation, and the associated carbon corrosion in the catalyst layer becomes a problem.This

accumulation also causes a gradual, but recoverable, drop in cell voltage over time. When operating in galvanostatic mode, purges are necessary to remove nitrogen/water from the anode and to recover the voltage. This periodic purging event causes voltage cycling in DEA operation, with a cycle defined as the duration between two consecutive purge events. The evolution of the cell voltage and the concentration of the species is very repeatable from cycle to cycle, because liquid water and inert gas accumulate at the end of the vertically oriented straight anode channels [67].

The hydrogen flow in a re-circulated anode makes convection a dominant force that determines the variation in channel gas composition. Convection is equally important in the DEA operation [71, 23] despite the very low anode flow rates that have led to the use of the continuous stirred reactor (CSTR) methodology in fuel cell with open channels [72]. When operating with a DEA both convection and diffusion influence the distribution of gasses in the channel. Convection dominates transport at the channel inlet, pushing hydrogen, nitrogen, oxygen and water towards the end of the channel. Gasses and water crossover from the cathode to the anode and accumulate at the end of the anode channel, blocking hydrogen from reaching this region. The hydrogen depleted region grows, reaching back toward the inlet as nitrogen accumulation continues during DEA operation. The presence of oxygen in the end region of the anode channel, where hydrogen is depleted, is of particular concern for cathode carbon corrosion.

The carbon corrosion in the catalyst layer is a major degradation source in operating a PEM fuel cell [26, 2]. The carbon catalyst support in PEM fuel cell is itself thermodynamically unstable due to its low equilibrium potential of 0.207 V with respect to reversible hydrogen electrode (RHE) at 25°C. Fortunately, under typical operating temperature (65°C) and interfacial potential (0.6 V) between membrane phase and metal phase, the carbon corrosion rate is considered negligible [35]. However, it is also reported that electrocatalysts such as Pt may lower the safe interfacial potential to 0.55 V or lower [38]. Hence the threshold potential may depend on the catalyst performance and operating conditions.

This chapter combines various mathematical models necessary for quantifying the carbon corrosion behavior in an operating cell with a DEA. In previous work [66, 65], a model of the nitrogen blanketing and water plugging effects was developed for DEA operation. The model predicts the fuel depletion observed in the experiments. Fuel depletion in the anode channel not only results in cell voltage decrease but also triggers carbon corrosion. As hydrogen is no longer sufficient to maintain the current (in galvanostatic operation), the equilibrium of

$$O_2 + 4H^+ + 4e^- \leftrightarrow 2H_2O$$

would move backwards due to the lack of hydrogen ions. Thus, at the location of fuel deple-

tion, oxygen could be generated from water dissociation, in addition to the general source of oxygen crossover through membrane. The amount of oxygen in the anode is negligible whenever there is sufficient hydrogen (proton) supply since it would be instantaneously reduced to water. The insufficiency of hydrogen also promotes:

$$C + 2H_2O \rightarrow CO_2 + 4H^+ + 4e^-$$

although it proceeds at a slower rate compared with water dissociation.

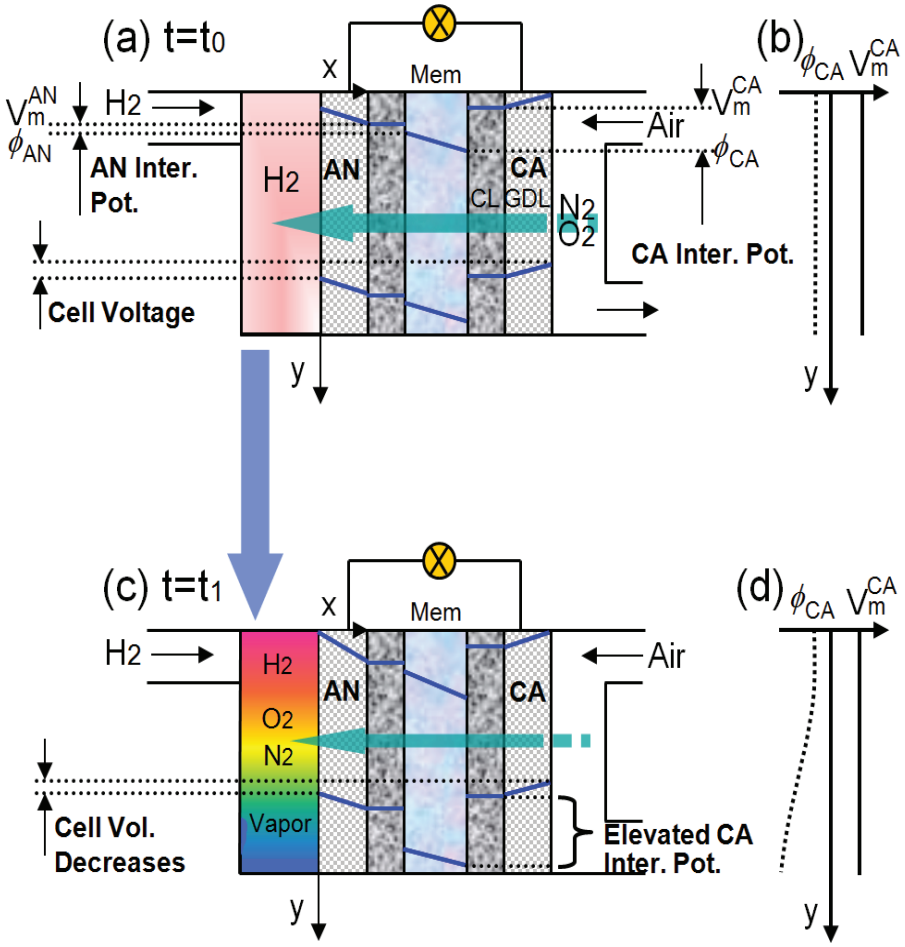

Figure 2.1 Scenario of carbon corrosion in DEA operation (not to scale). Subfigure (a) Shows the initial reactant distribution (uniform hydrogen) immediately after an anode purge. Subfigure (c) shows the reactant distribution and resulting change in interfacial potential at the end of the channels right before an anode purge. Subfigures (b) and (d) are the cathode membrane/metal phase potentials corresponding to subfigures (a) and (c), respectively. The differences between V_m^{AN} and ϕ_{AN}, V_m^{CA} and ϕ_{CA} are termed interfacial potentials at anode and cathode, respectively. The magnitude of interfacial potential directly determines the carbon corrosion rate. The difference between V_m^{CA} and V_m^{AN} is the cell voltage.

The scenario of carbon corrosion in DEA operation is as follows. As shown in Fig. 2.1a,

initially ($t = t_0$), when hydrogen completely occupies the anode after a purge, the membrane exhibits uniform potential along y direction. The uniform potential is slightly negative (~-0.01 V) as the anode metal potential is zero.

As time evolves ($t = t_1$), hydrogen depletion in the anode occurs (see Fig. 2.9) due to the nitrogen/oxygen crossover and the water flooding. The presence of oxygen in the anode is crucial, which leads to the membrane phase potential drop in the area of hydrogen depletion. Thus anode and cathode interfacial potentials increase compared with $t = t_0$ (see Fig. 2.12).

A special case of carbon corrosion caused by the development of a H_2/O_2 boundary in the anode that occurs during the start-up/shutdown process of the cell has been studied both numerically [35, 73, 74] and experimentally [37, 75, 76, 77, 78]. The corrosion mechanism for this case can be illustrated by Fig. 1.7, where the dotted line indicates the H_2/O_2 boundary. In this case, the complete hydrogen starvation in the rear part of the anode channel leads to high interfacial potential (~1.6 V) at the cathode. The cathode carbon can be completely oxidized within hours under such potential. Start-up/shutdown procedures have been proposed to alleviate such carbon corrosion issues [79, 80].

In this chapter we employ a 1-D along-channel model to study DEA operation. Multi-dimensional modeling is not necessary to capture the observed voltage behavior due to the along-channel stratified patterns [81]. A carbon corrosion model is developed based on the corrosion mechanism in Ref. [36] and then incorporated into our prior model which predicts the nitrogen accumulation [66, 82]. The important parameter to capture by modeling is the oxygen concentration in the anode, and the associated voltage degradation due to carbon corrosion. In the following section, the model equations are presented and discussed. The model is then validated in Section 3 with simulation results discussed in Section 4.

2.2 Model Overview

In DEA operation diffusion prevents the development of a sharp interface between fuel and oxidant in the anode channel, which is different from the start-up/shutdown case with H_2/O_2 boundary. Nitrogen, oxygen and water can cross through the membrane in either direction, however the convective flux due to hydrogen consumption causes the accumulation of inert and product gasses at the end of the channel.

With these features and other simplifications, the major assumptions in the present model are: 1) the model is simplified to one dimension along the channel direction. 2) The effects of liquid water are not considered in the model. 3) The electrochemical loss

of Pt [33, 34] is not modeled. The particle size of Pt and formation of PtO layer affect the carbon reaction rate, but we control the cell potential in both simulation and experiments to avoid high interfacial potential (<1.5V) at cathode, thus the electrochemical loss of Pt is minimized. The loss of active Pt sites, however, is reflected in the present model via a correlation with the remaining carbon in the catalyst layer. 4) The membrane degradation, such as chemical decomposition of the polymer, also contributes to the cell voltage decay [41, 40, 83]. The present model assumes a good membrane condition. Correspondingly, the operating conditions for simulations in this dissertation are chosen so that a humidified membrane and small pressure difference across membrane can be maintained. The model is not appropriate to be used with dry cathode supply (see Subsection 3.4.2). 5) We consider only the carbon corrosion in the catalyst layer, and do not include any impacts from the instability of the GDL material [2]. 6) The carbon corrosion is a dynamic process which can alter the transport and electrochemical characteristics of the catalyst layer, namely, the values of physical and geometrical parameters used in the modeling. For simplicity, these parameters remain unchanged during the dynamic process and all effects from carbon corrosion is lumped into a tunable parameter q (see Section 2.4).

There are six dynamic states in the model: the molar fractions of N_2, O_2 and vapor ($n_{N_2,O_2,V}$) in the anode channel, the partial pressure of O_2 ($P_{O_2,CA}$) in the cathode channel, the mass of carbon support in the cathode catalyst layer per cm^{-2} (m_C), and the membrane water content (λ). Meanwhile, there are two variables which satisfy algebraic constraints: the membrane phase potential at the anode (ϕ_{AN}) and cell voltage (E_{cell}).

2.3 Reaction Kinetics

Three electrochemical reactions take place in the anode:

$$H_2 \leftrightarrow 2H^+ + 2e^- \tag{2.1}$$

$$O_2 + 4H^+ + 4e^- \leftrightarrow 2H_2O \tag{2.2}$$

$$C + 2H_2O \rightarrow CO_2 + 4H^+ + 4e^- \tag{2.3}$$

The oxygen reduction reaction Eq. 2.2 and carbon corrosion reaction Eq. 2.3 are very small compared with the hydrogen dissociation reaction Eq. 2.1 in terms of current density (at least 1000-fold difference); nevertheless, such current density corresponds to sub-

stantial carbon loss in DEA operation. The carbon corrosion shown in 2.3 is generally considered an irreversible reaction in aqueous systems [84]. Recent experimental observations [85, 86, 87] have shown carbon loss in the anode, which supports the inclusion of the anode carbon reaction in the model development despite being less severe than the cathode. In the cathode, only the reactions in Eqs. 2.2 and 2.3 are considered.

The local distributed current density in the anode i_{AN} is the summation of the main reaction and two partial reactions:

$$i_{AN} = i_{H_2,AN} + i_{O_2,AN} + i_{C,AN} \tag{2.4}$$

For the cathode, there are reactions of oxygen and carbon. The crossover hydrogen is assumed to be completely consumed at the cathode catalyst layer, the accumulation effects are ignored due to the cathode flow-through:

$$i_{CA} = i_{O_2,CA} + i_{C,CA} \tag{2.5}$$

Two algebraic variables in the present model, membrane phase potential at the anode (ϕ_{AN}) and cell voltage (E_{cell}), correspond to the following two equations:

$$i_{AN} + i_{CA} = 0 \tag{2.6}$$

$$i_{fc} = \frac{1}{L}\int_0^L i_{AN} dy \tag{2.7}$$

Equation 2.6 represents the local conservation of charge, the total anode local current is equal to the cathode. We assume that the in-plane proton current can be neglected. This assumption is valid due to the low ionic conductivity of the membrane relative to the high electronic conductivity of the current collector [36]. Note that the anodic current (releasing protons) is defined positive and cathodic (consuming protons) negative. Equation 2.7 specifies the average (apparent) current density drawn from the cell which is a model input. It is important to note that every term in Eqs. 2.6 and 2.7 can be expressed as a function of ϕ_{AN} and/or E_{cell}. Thus Eqs. 2.6 and 2.7 constitute the constraints for these two variables.

The reaction kinetics of each partial reaction in Eq. 2.4 are described by the Bulter-

Volmer relation:

$$i_{H_2,AN} = \gamma_{Pt} i_{0,H_2} L_{Pt} \Big\{ \frac{P_{H_2}^{CL}}{P_{H_2}^*} \exp\Big[\frac{\alpha_{a,H_2} F}{RT}(V_m^{AN} - \phi_{AN} - V_{H_2}^{eq})\Big] - \frac{P_{H_2}^{CL}}{P_{H_2}^*} \exp\Big[\frac{-\alpha_{c,H_2} F}{RT}(V_m^{AN} - \phi_{AN} - V_{H_2}^{eq})\Big]\Big\} \tag{2.8}$$

$$P_{H_2}^{CL} = P_{H_2}^{CH} - \frac{i_{H_2,AN}\delta_{GDL} RT}{2F D_{H_2}} \tag{2.9}$$

$$i_{O_2,AN} = \gamma_{Pt} i_{0,O_2} L_{Pt} \Big\{ \frac{P_{V,AN}}{P_{V,AN}^*} \exp\Big[\frac{\alpha_{a,O_2} F}{RT}(V_m^{AN} - \phi_{AN} - V_{O_2}^{eq})\Big] - \left(\frac{P_{O_2,AN}}{P_{O_2,AN}^*}\right)^{\beta_{O_2}} \left(\frac{P_{H_2}}{P_{H_2}^*}\right)^{\beta_{H_2}} \times \exp\Big[\frac{-\alpha_{c,O_2} F}{RT}(V_m^{AN} - \phi_{AN} - V_{O_2}^{eq})\Big]\Big\} \tag{2.10}$$

$$i_{C,AN} = \gamma_C i_{0,C} L_C \frac{P_{V,AN}}{P_{V,AN}^*} \exp\Big[\frac{\alpha_{a,C} F}{RT}(V_m^{AN} - \phi_{AN} - V_C^{eq})\Big] \tag{2.11}$$

where γ_* ($*$=Pt or C) is the active platinum or carbon surface area per unit mass and L_* is the loading of platinum or carbon. γ_{Pt} is measurable and widely known as electrochemical surface area (ECSA). ϕ_{AN} is the membrane phase potential at the anode catalyst layer/membrane interface. D_{H_2} is the hydrogen diffusion coefficient in the GDL. Equation 2.9 represents the effect of hydrogen diffusion through the GDL. Note in Eq. 2.10, the oxygen partial reaction (water dissociation) depends on both hydrogen and oxygen concentrations, which is different from a normal cathode scenario where hydrogen ion supply is considered sufficient. Also note that ideally, hydrogen ion concentration should be used rather than hydrogen partial pressure, which is a simplification in the model. A similar approach is used in Refs. [56] and [62].

For the cathode, the Bulter-Volmer relations are similar:

$$i_{O_2,CA} = \varepsilon_C \gamma_{Pt} i_{0,O_2} L_{Pt} \Big\{ \frac{P_{V,CA}}{P_{V,CA}^*} \exp\Big[\frac{\alpha_{a,O_2} F}{RT}(V_m^{CA} - \phi_{CA} - V_{O_2}^{eq})\Big] - \left(\frac{P_{O_2,CA}^{CL}}{P_{O_2,CA}^*}\right)^{\beta_{O_2}} \left(\frac{P_{H_2}}{P_{H_2}^*}\right)^{\beta_{H_2}} \times \exp\Big[\frac{-\alpha_{c,O_2} F}{RT}(V_m^{CA} - \phi_{CA} - V_{O_2}^{eq})\Big]\Big\} \tag{2.12}$$

$$P_{O_2}^{CL} = P_{O_2}^{CH} + \frac{i_{O_2,CA}\delta_{GDL}RT}{4FD_{O_2}} \tag{2.13}$$

$$i_{C,CA} = \varepsilon_C \gamma_C i_{0,C} L_C \frac{P_{V,CA}}{P^*_{V,CA}} \exp\left[\frac{\alpha_{a,C}F}{RT}(V_m^{CA} - \phi_{CA} - V_C^{eq})\right] \tag{2.14}$$

where ε_C is a fraction factor of remaining carbon defined by Eq. 2.17 to reflect the influences of carbon loss on the reaction kinetics and cell voltage. A similar power factor was also used in [88] to account the decreasing rate of carbon corrosion over time observed in the experiment.

There are different approaches in modeling the carbon corrosion rate since the mechanism is still not fully understood. The corrosion rate has been shown to drop with time at potential [84], which suggests that the Bulter-Volmer equation may not give an accurate prediction of the corrosion rate. This chapter focuses on the impact of distributed concentration and reaction rates along the channel associated with DEA operation and presents a way to quantify the carbon/voltage loss. Any model of carbon corrosion, such as the one reviewed in Ref. [84] may be incorporated into our modeling framework. A similar drop in carbon corrosion rate over time is captured by the model through the loss of active platinum sites in Eq. 2.17, with the parameter ε_C. The power factor in Eq. 2.17 is a tuned parameter which may be studied and tuned in the future.

Cell voltage and local current are used to connect the metal/membrane phase potentials at anode (V_m^{AN}) and cathode (V_m^{CA}):

$$V_m^{CA} = V_m^{AN} + E_{cell} + R_{GDL} i_{AN} \tag{2.15}$$

$$\phi_{CA} = \phi_{AN} - R_{mem} i_{AN} \tag{2.16}$$

2.4 Carbon Corrosion

As carbon corrodes, the electrode becomes thinner and the active catalytic area decreases. In Eqs. 2.12 and 2.14, ε_C is an effective factor to account for the influence of carbon loss

on the cathode reaction kinetics [89, 88]:

$$\varepsilon_C(y,t) = \left[\frac{m_C(y,t)}{m_{C,0}}\right]^q \tag{2.17}$$

where $m_{C,0}$ is the initial carbon loading per unit area and m_C is the carbon mass per unit area. The influences of carbon loss on the effective catalytic area are thus reflected, although a more complicated model of Pt loss (such as dissolution and mitigation [33, 34]) has not been included in this work. Incorporating ε_C in Eq. 2.14 also leads to an asymptotic drop of corrosion current with constant potential, although this drop is associated with Pt loss proportional to the carbon corrosion. Anode carbon loss is negligible compared with cathode (as shown in Fig. 2.11), therefore the effective factor accounting for carbon loss is not incorporated in Eqs. 2.8-2.11.

For Eq. 2.17, Ref. [89] uses a power factor q=4 to account for the influence of carbon corrosion on the loss of catalytic sites and therefore the reaction kinetics for both carbon corrosion and oxygen reduction. However, the authors state that the value of q is assumed rather than fitted or derived. The reaction kinetics decrease (increase) as the carbon is being consumed if q is positive (negative). Generally, the overall trend of reaction kinetics is decreasing as the carbon corrosion continues due to the loss of catalytic sites. However, it is likely to observe an increasing trend of carbon corrosion rate within a short period of time due to the non-homogeneous property of carbon. The properties of the carbon determine the value of parameter q and therefore the evolution trend. If the composition of carbon is homogeneous, the corrosion rate tends to decrease with time. If the composition of carbon is non-homogeneous, the most vulnerable part will be corroded followed by the more resistant region. It has been reported that the amorphous core of the carbon particle is corroded first followed by the graphitic shell, which is more resistant to corrosion for a conventional carbon support [88]. This process corresponds to a positive value of q. In this dissertation work, a positive q is assumed, which yields consistent voltage evolutions from modeling and experiments.

As the carbon corrosion proceeds, the morphological structure and the physical properties of the catalyst layer will change. Generally, the size of of carbon particle agglomerate increases, the porosity of electrode decreases, and the thickness of catalyst layer reduces [90, 91]. The oxygen diffusion is diminished significantly since the surface of catalyst layer becomes hydrophilic due to the carbon oxide species that form on carbon particles, leading to an increased mass transport resistance [92]. From the EIS diagnosis, it is also found that the charge transfer resistance enlarges dramatically, suggesting higher activation loss [92, 93]. Therefore, physical parameters such as K_{O_2} in Eq. 2.42 and i_{0,O_2}

in Eq. 2.12 are dynamically changing with the carbon corrosion process, which is not captured by the modeling. As an approximation, the effective factor ε_C shown in the oxygen reduction (Eq. 2.12) lumps in all those effects from carbon corrosion.

The local carbon loss m_C is related to the carbon reaction rate at cathode $i_{C,CA}$:

$$\frac{\partial m_C}{\partial t} = -\frac{M_C i_{C,CA}}{4F} \tag{2.18}$$

where F is the Faraday constant and M_C is the molar mass of carbon.

2.4.1 Agglomerate Model

In this subsection, the focus is to use the agglomerate model framework, as an alternative to the power law model shown in prior sections, to study the carbon corrosion and associated voltage degradation.

The agglomerate model captures the influences of oxygen dissolution and transport on the reaction kinetics by simulating the realistic catalyst layer three-phase environment, whereas it does not particularly describe the kinetics of cathode carbon corrosion. Utilizing the agglomerate model framework, the influences of carbon corrosion on the voltage degradation are captured by changing the relevant geometrical parameters of the catalyst layer. In the relevant literature, it has been reported that the carbon corrosion may start from the center of the agglomerate if the shell is more graphitized [88, 94], and a hollow structure can form, which eventually collapses with decreased porosity [90, 95]. It has been recently reported, however, that structural collapse and accompanying loss of porosity were not observed; rather, the wettability of the catalyst layer changes as the carbon corrosion proceeds [92, 96]. Modeling such a complicated process is beyond the scope of a macro-scale model such as the agglomerate model.

In the agglomerate model the volumetric current density is defined as [97, 98]:

$$\bigtriangledown \cdot i = 4F\frac{P_{O_2}}{H}\left[\frac{1}{E_r k_c(1-\varepsilon_V^{CL})} + \frac{(r_{agg}+\delta_{agg})\delta_{agg}}{a_{agg} r_{agg} D_{O_2}}\right]^{-1} \tag{2.19}$$

where P_{O_2} is the oxygen partial pressure in the pore of catalyst layer, ε_V^{CL} is the porosity (volume fraction of pore) in the catalyst layer, r_{agg} is the radius of each agglomerate, δ_{agg} is the thickness of ionomer thin film on the surface of sphere agglomerate, H is the Henry

constant (ATM m^3/mol), and E_r is an effective factor defined by:

$$E_r = \frac{1}{\phi_L}\left[\frac{1}{tanh(3\phi_L)} - \frac{1}{3\phi_L}\right] \tag{2.20}$$

where the Thieleos modulus, ϕ_L, for a spherical agglomerate is given by:

$$\phi_L = \frac{r_{agg}}{3}\left[\frac{k_c}{D_{O_2}\varepsilon_{ino}^{agg\,1.5}}\right]^{0.5} \tag{2.21}$$

The reaction constant, k_c, is given by:

$$k_c = \frac{A_v i_{0,O_2}}{4FC_{O_2}^{ref}(1-\varepsilon_V^{CL})}\left[exp(-\frac{\alpha F}{RT}\eta) - exp(\frac{(1-\alpha)F}{RT}\eta)\right] \tag{2.22}$$

where A_v=$\frac{A_0 m_{Pt}}{L}$ is the total catalytic area for ORR per unit volume of cathode catalyst layer, A_0 is the measureable ECSA (m^2Pt/g), m_{Pt} is the Pt loading in mg/cm^2, and L is the cathode catalyst layer thickness. The cathode overpotential η is expressed as:

$$\eta = V_m^{AN} + E_{cell} + R_{GDL}i_{ave} - (\phi_{AN} - R_{mem}i_{ave}) - V_{eq}^{O_2} = E_{cell} - (R_{GDL} + R_{mem})i_{ave} - V_{eq}^{O_2}. \tag{2.23}$$

Since $\int_0^L \bigtriangledown \cdot i$ dy=L $\bigtriangledown \cdot i$=i_{ave}, we have obtained the correlation between i_{ave} and E_{cell} that can be used to generate the polarization curve. Note that the anode overpotential is neglected.

Some catalyst design parameters are used to calculate the related physical parameters. The mass ratio between Pt and Pt+Carbon, Pt|C, is used to calculate the solid volume fraction in the catalyst layer:

$$\varepsilon_S^{CL} = \frac{(\frac{1}{\rho_{Pt}} + \frac{1-Pt|C}{Pt|C\rho_C})m_{Pt}}{L}. \tag{2.24}$$

Similarly, the mass ratio between the ionomer and ionomer+carbon, I|C, is used to calculate the ionomer volume fraction in the catalyst layer:

$$\varepsilon_{ion}^{CL} = \frac{m_{ion}}{\rho_{ion}L} = \frac{\frac{m_{Pt}(1-Pt|C)I|C}{Pt|C(1-I|C)}}{\rho_{ion}L} \tag{2.25}$$

where m_{ion} is the mass loading of ionomer (mg/cm^2). Then the pore volume fraction, or

porosity, of the catalyst layer is simply:

$$\varepsilon_V^{CL} = 1 - \varepsilon_S^{CL} - \varepsilon_{ion}^{CL}. \tag{2.26}$$

The total amount of agglomerate in the catalyst layer, n, can be calculated by:

$$n = \frac{LA\varepsilon_S^{CL}}{\frac{4}{3}\pi r_{agg}^3(1-\varepsilon_{ion}^{agg})} \tag{2.27}$$

where ε_{ion}^{agg} is the volume fraction of ionomer in the agglomerate. A constant ε_{ion}^{agg} is assumed in the model.

The effective surface area usable to dissolve oxygen into the agglomerate per unit volume of the catalyst layer a_{agg} is calculated by:

$$a_{agg} = 4n\pi(r_{agg} + \delta_{agg})^2\varepsilon_V^{CL}. \tag{2.28}$$

There is a correlation between ECSA (cm^2/g), A_0, and the Pt|C ratio obtained from a least squares fit to the empirical data [98, 99], although A_0 is also measurable:

$$A_0 = 2.2779\times10^6(Pt|C)^3 - 1.5857\times10^6(Pt|C)^2 - 2.0153\times10^6 Pt|C + 1.5950\times10^6. \tag{2.29}$$

It is not clear that whether this correlation holds for a specific type of Pt/C. Thus, direct measurement of ECSA is still preferred.

The total catalytic area for ORR per unit volume of the catalyst layer, A_v, is written as:

$$A_v = A_0\frac{m_{Pt}}{L}. \tag{2.30}$$

Unlike in the power law model, the remaining carbon mass, m_C, is not used in the agglomerate model. However, if a CO_2 analyzer is available at the downstream of the cathode to obtain the real-time corrosion rate, we can calculate m_C assuming that all the carbon loss is in the form of CO_2:

$$m_C(t-\tau) = m_{C,0} - \frac{Pv\pi r_p^2}{RT}\int_0^t ppm_{x=L}(t')dt' \tag{2.31}$$

where τ is the resident time of CO_2 in the pipeline, t is any time later than τ, and r_p is the radius of the pipeline. The spatial variability should be avoided by using high stoichiometry ratios in both anode and cathode during the measurement. The CO_2 analyzer data can also be used to tune $i_{0,C}$ in the power law model, which is planned as a future work.

2.4.2 Model Parameters

There are many physical and geometrical parameters in the agglomerate model. One important feature of the agglomerate model is to capture the influences of geometrical parameters on the dissolution and transport of oxygen towards the catalytic sites. For accurate modeling results, these parameters need to be determined appropriately. Table 2.1 summarizes how these parameters can be determined for a agglomerate-based carbon corrosion modeling.

Parameter	How to determine	Value at BOL
$m_C(t)$	Calculated from CO_2 ppm, Eq. 2.31	$m_{C,0}$ from supplier, or measured
ε_V^{CL}	Measured	$\varepsilon_{V,0}^{CL}$ measureable
$L(\varepsilon_V^{CL})$	Calculated from ε_V^{CL}, Eqs. 2.24-2.26	L_0 from supplier
$Pt\|C(m_C)$	Calculated from m_C	Initial Pt|C from supplier
I|C	Assumed to be constant	Initial I|C from supplier, or assumed
$r_{agg}(m_C)$	To be tuned to match polarization data	$r_{agg,0}$ tunable
δ_{agg}	Assumed to be constant	$\delta_{agg,0}$ from literature
ε_{ion}^{agg}	Assumed to be constant	$\varepsilon_{ion,0}^{agg}$ assumed
$n(m_C)$	Calculated, Eq. 2.27	n_0 calculated
$a_{agg}(m_C)$	Calculated, Eq. 2.28	$a_{agg,0}$ calculated
$A_0(m_C)$	Calculated, Eq. 2.29	Initial A_0 calculated
$A_v(m_C)$	Calculated, Eq. 2.30	Initial A_v calculated
H	From literature	
P_{O_2}	From cathode partial pressure of O_2	
i_{0,O_2}	From literature	

Table 2.1 Summary of model parameters

2.4.3 Power Law Model

Revisiting the power law model [89, 88, 68], the Butler-Volmer equation is used to describe the cathode overpotential:

$$i_{ave} = (\frac{m_C}{m_{C,0}})^q i_{0,O_2} A_{Pt,0} m_{Pt,0} \left[exp(-\frac{\alpha F}{RT}\eta) - exp(\frac{(1-\alpha)F}{RT}\eta) \right] \tag{2.32}$$

where $A_{Pt,0}$ is the initial ECSA (m^2/g) and $m_{Pt,0}$ is the initial Pt loading (mg/cm^2). The overpotential η is related to the cell voltage E_{cell} by Eq. 2.23.

2.4.4 Comparison of Two Approaches

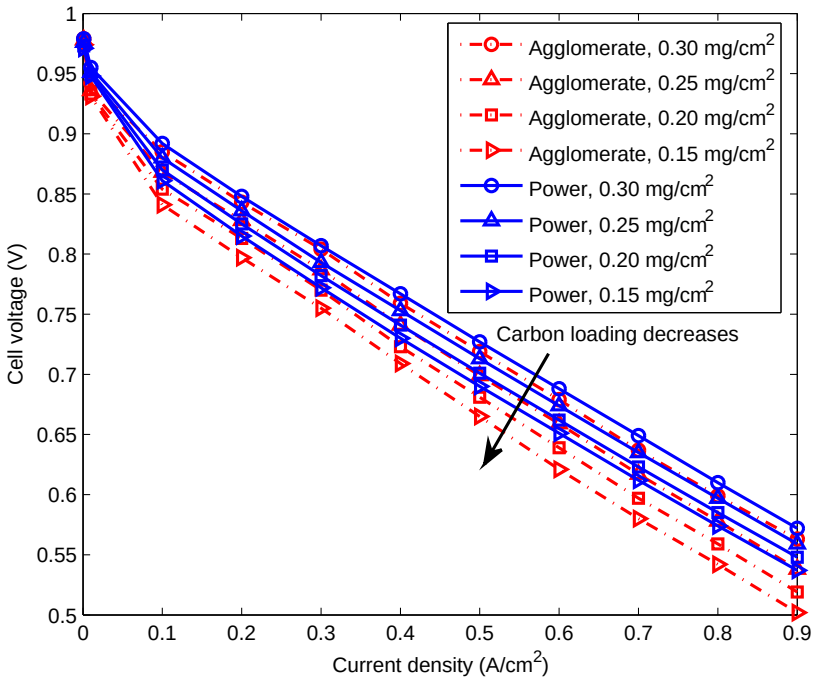

Figure 2.2 The polarization curves from both agglomerate and power law models with the ongoing carbon corrosion. Cell temperature 70°C and cathode O_2 partial pressure 0.252 ATM are used in the simulation.

The carbon corrosion is a very complicated process and normally coupled with the Pt agglomeration, dissolution/redeposition, and oxidation. In the present model, the Pt is assumed to remain in its original state. As the carbon corrosion proceeds, the size of the agglomerate will be reduced first, until the cathode collapses, which will lead to a decreased porosity, reduced catalyst layer thickness, and increased size of the agglomerate [90]. The present model cannot capture the whole dynamic process. Instead, it is aimed to capture the changes of several key parameters as the carbon corrosion continues and show how these changes influence the polarization.

Figure 2.2 shows the polarization curves obtained from both the agglomerate model and the power law model, as the carbon corrosion proceeds (m_C decreases). The values of m_C are chosen to represent the different stages in the corrosion process, as shown in the first subplot of Fig. 2.4. There are two tuned parameters, L and r_{agg}, in order to match the

four polarization curves from the agglomerate model in Fig. 2.2 to those from the power law model. These two parameters dictate the geometrical changes of the catalyst layer with ongoing carbon corrosion. The sensitivity of the agglomerate model to these two parameters is shown in Fig. 2.3. Indeed, the polarization presents an apparent decreasing trend as r_{agg} increases or L decreases due to the ongoing carbon corrosion, which is consistent with the experimental observations [90].

In the seventh subplot of Fig. 2.4, the values of m_C and L are used to calculate ε_V^{CL} by Eq. 2.24-Eq. 2.26. With the tuned parameter r_{agg} shown in the third subplot, a_{agg} can be determined by Eq. 2.28 and n determined by Eq. 2.27. Finally, the polarization curves for each approach are obtained from Eq. 2.23 and Eq. 2.32, respectively.

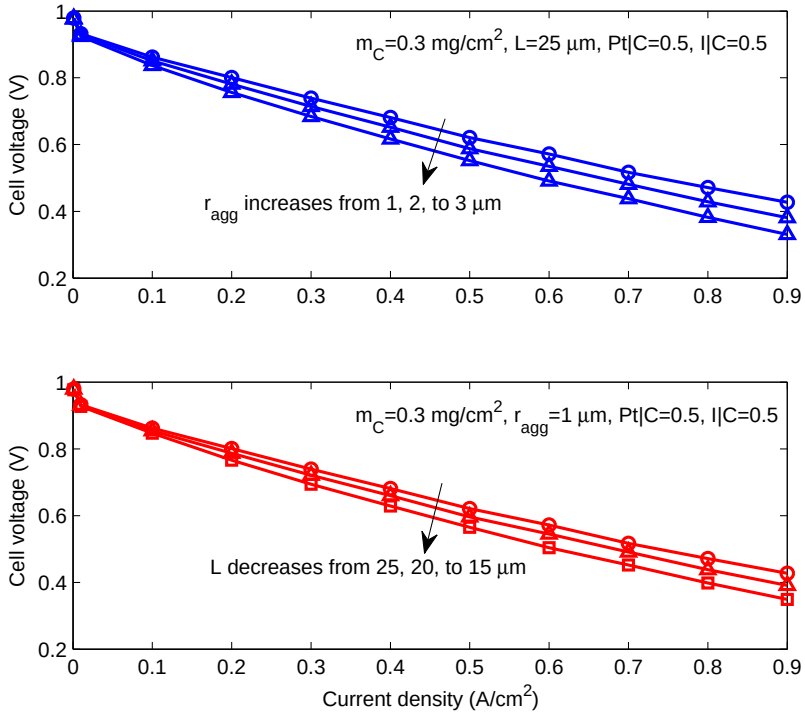

Figure 2.3 The sensitivity of agglomerate model to the parameter values of r_{agg} and L. Cell temperature 70°C and cathode O_2 partial pressure 0.252 ATM are used in the simulation.

With tuned L and r_{agg}, the agglomerate model can be approximated by the power law model, as shown in Fig. 2.2, which indicates the fidelity of power law model for carbon corrosion. Noticeably, the agglomerate model predicts lower cell voltage than the power law model as the carbon corrosion continues. The power law model does not capture any physical parameters relevant to the catalyst layer. Nevertheless, it features only two tunable parameters (q and $i_{0,C}$) and outputs similar polarizations, therefore more appropriate for a control-oriented model and for parameterization given an unknown catalyst. As a compar-

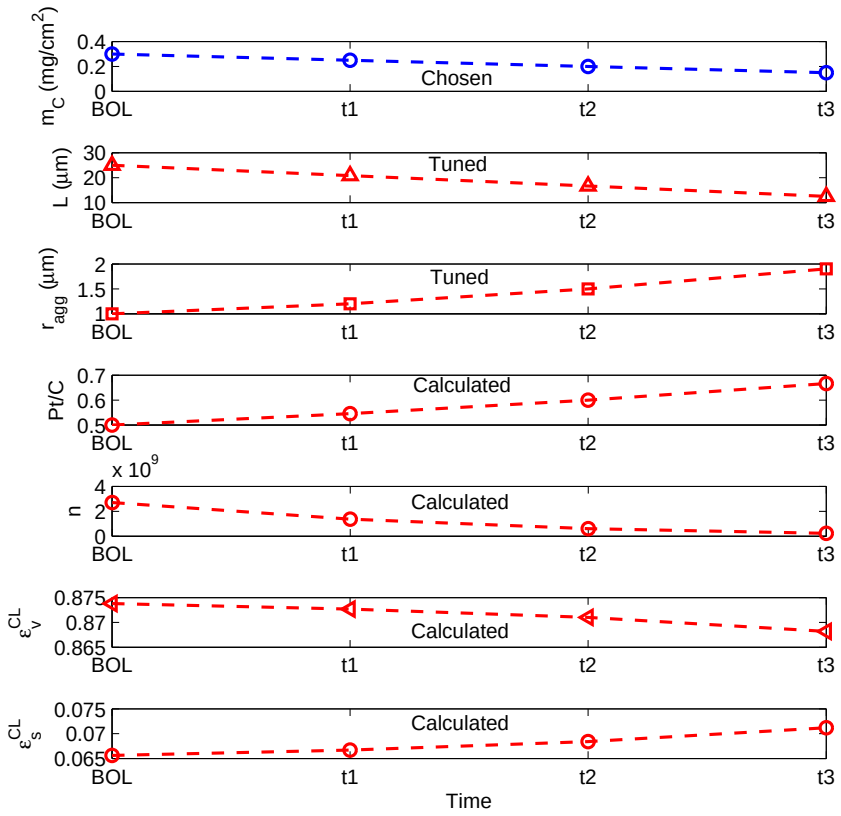

Figure 2.4 The parameter values in the agglomerate model, either from assumption or calculation, as the carbon corrosion proceeds.

ison, the agglomerate model is more sensitive to the loss of carbon mass in terms of the voltage degradation at the same current density. The effect of mass transport loss becomes apparent in agglomerate model, which predicts lower voltages at elevated current densities. The tuning of multiple physical parameters shown in Table 2.1, however, requires detailed information from the catalyst supplier and/or elaborate experimental setup. In addition, the tuning itself may become a multi-variable optimization problem that is difficult to solve.

2.5 Along-Channel Mass Transport

Extending the prior model framework of a ternary system (H_2, N_2, H_2O) [82], the time-dependent composition in the anode is modeled using Stefan-Maxwell equations for a quaternary system (H_2, O_2, N_2, H_2O) and solved by spatial discretization and numerical time integration. The model describes the mass conservation (for the gas phase only)

including convection, diffusion, and source terms in the anode channel:

$$\frac{P_{an}}{RT}\frac{\partial n_i}{\partial t} = -\frac{\partial}{\partial y}(J_i + n_i N_t) + r_i \tag{2.33}$$

for $i = [1,2,3,4] = [N_2, H_2O, O_2, H_2]$, where N_t is the total convective gas flux, J_i is the diffusive flux, and r_i denotes the source terms (reactive and/or crossover fluxes per unit channel height). All fluxes discussed in this chapter have a unit of $mol\ m^{-2}s^{-1}$. Only three of the four components are independent in this modeling framework. We choose to model the mole fractions of nitrogen, n_{N_2}, water vapor, n_{H_2O} and oxygen, n_{O_2}, as our dynamic states. The hydrogen molar fraction can be calculated from the other three since $\Sigma n_i = 1$. The anode pressure, P_{an}, is assumed to be constant since it is set by an upstream pressure regulator during the DEA operation.

The causal formulation for the quaternary Stefan-Maxwell diffusive fluxes can be summarized as:

$$J_i = -\frac{P_{AN}}{RT\psi(n)} W \frac{dn_i}{dy} \tag{2.34}$$

where ψ is a scalar function of the species molar fractions and W is a 4 by 4 coefficient matrix (refer to [100]).

Assuming the outlet flow is given by $N_t(L) = N_{out}$, then conservation of total mass (gas mixture) allows solving of Eq. 2.33 for $N_t(x)$. Since $\Sigma J_i = 0$ by definition, the equation for mass conservation can be written as:

$$\frac{\partial N_t}{\partial y} = \Sigma r_i \tag{2.35}$$

Then the convective flux along the channel can be found by:

$$\begin{aligned} N_t(y) = N_t(L) + \int_y^L [&r_{H_2,rct}(\tilde{y}) + r_{H_2,crs}(\tilde{y}) + r_{N_2,crs}(\tilde{y}) \\ &+ r_{H_2O,crs}(\tilde{y}) + r_{H_2O,rct}(\tilde{y}) + r_{O_2,crs}(\tilde{y}) + r_{O_2,rct}(\tilde{y})] d\tilde{y} \end{aligned} \tag{2.36}$$

The expressions for $r_{H_2,rct}$, $r_{N_2,crs}$, $r_{H_2O,crs}$ are given below without further explanation since details are available in [66]:

$$r_{H_2,rct} = \frac{i_{H_2,AN}}{2F h_{ch,an}} \tag{2.37}$$

$$r_{N_2,crs} = -K_{N_2}\frac{P_{N_2,CA} - P_{N_2,AN}}{\delta_{mb} h_{ch,an}} \tag{2.38}$$

$$r_{H_2O,crs} = -\frac{\lambda_{CA} - \lambda_{AN}}{R_{mb} h_{ch,an}} + n_d \frac{i_{AN}}{F h_{ch,an}} \tag{2.39}$$

where R_{mb} is the resistance to membrane transport defined in Ref. [66] and n_d is the electro-osmotic drag coefficient.

Given the fast reaction kinetics of crossover hydrogen at the cathode catalyst layer, the partial pressure of hydrogen at cathode is assumed to be zero. Thus the hydrogen crossover flux is a function of hydrogen pressure at anode P_{H_2} only:

$$r_{H_2,crs} = K_{H_2} \frac{P_{H_2}^{CL}}{\delta_{mb} h_{ch,an}} \tag{2.40}$$

in which the permeance of hydrogen through the membrane K_{H_2} is a function of membrane water content and temperature [101]:

$$K_{H_2} = (0.29 + 2.2 f_v) \times 10^{-14} \exp\left[\frac{E_{H_2}}{R}(\frac{1}{T_{ref}} - \frac{1}{T})\right] \tag{2.41}$$

Similarly for $r_{O_2,crs}$, $r_{O_2,rct}$ and $r_{H_2O,rct}$:

$$r_{O_2,crs} = -K_{O_2} \frac{P_{O_2,CA}^{CL} - P_{O_2,AN}}{\delta_{mb} h_{ch,an}} \tag{2.42}$$

$$r_{O_2,rct} = -\frac{i_{O_2,AN}}{4F h_{ch,an}} \tag{2.43}$$

$$r_{H_2O,rct} = \frac{i_{O_2,AN}}{2F h_{ch,an}} \tag{2.44}$$

where $P_{O_2,CA}/P_{O_2,AN}$ is the partial pressure of oxygen in the cathode/anode and δ_{mb} is the thickness of membrane. For simplicity it is assumed that oxygen only accumulates in the gas phase and not in the ionomer phase due to the large volume difference between the channel and membrane. The expression for $i_{O_2,AN}$, the anode partial current density of oxygen reaction, is given by Eq. 2.10. The permeance of oxygen through membrane K_{O_2} (mol $Pa^{-1}m^{-1}s^{-1}$) in Eq. 2.42 is correlated with temperature and membrane water content [101]:

$$K_{O_2} = k_{O_2}(0.11 + 1.9 f_v) \times 10^{-14} \exp\left[\frac{E_{O_2}}{R}(\frac{1}{T_{ref}} - \frac{1}{T})\right] \tag{2.45}$$

where k_{O_2} is a scale factor for tuning the oxygen crossover flux, E_{O_2}=20 kJ/mol [102], and

f_v is the volume fraction of water in membrane defined by:

$$f_v = \frac{\lambda V_w}{V_m + \lambda V_w} \tag{2.46}$$

where V_w is the molar volumes of water in membrane, and $V_m = EW/\rho_{mb,dry}$ the molar volume of dry membrane (equivalent weight by density). Similarly, the permeance of nitrogen, K_{N_2}, is calculated by [101]:

$$K_{N_2} = k_{N_2}(0.0295 + 1.21 f_v - 1.93 f_v^2) \times 10^{-14} \exp\left[\frac{E_{O_2}}{R}(\frac{1}{T_{ref}} - \frac{1}{T})\right]. \tag{2.47}$$

In the cathode, the material balance for oxygen is established considering diffusion, convection, reaction, and crossover. The nitrogen partial pressure can then be obtained since the cathode system pressure is assumed to be constant. The oxygen partial pressure in the cathode channel is the last state in the model:

$$\frac{1}{RT}\frac{\partial P_{O_2,CA}}{\partial t} = -\frac{D_{O_2}}{RT}\frac{\partial^2 P_{O_2,CA}}{\partial y^2} + \frac{1}{RT}\frac{\partial (P_{O_2,CA} u_{ca,in})}{\partial y} - \frac{i_{O_2,CA}}{4F h_{ch,ca}} + \frac{K_{H_2} P_{H_2}^{CL}}{2\delta_{mb} h_{ch,ca}} + \frac{r_{O_2,crs}}{h_{ch,ca}} \tag{2.48}$$

where D_{O_2} is the Fickian diffusivity of O_2, h the channel depth, and $u_{ca,in}$ the gas velocity at the cathode inlet (assumed constant along the channel for simplicity):

$$u_{ca,in} = \frac{SR_{ca} i_{fc} L_{ca,ch} RT (w_{ch,ca} + w_{rib,ca})}{4F S P_{O_2,CA,in} h_{ch,ca} w_{ch,ca}} \tag{2.49}$$

where SR_{ca} is the stoichiometry ratio in the cathode and S the total MEA area.

Note that Eqs. 2.33 and 2.48 correspond to the four states in the model ($x_{N_2,O_2,V}$ and $P_{O_2,CA}$), and 2.48 is coupled with Eq. 2.12.

The six dynamic states together with two algebraic variables are solved simultaneously using Matlab ODE15s solver. The central difference scheme is used for discretizing spatial derivatives. The parameter values of the present model are summarized in Table 2.2.

2.6 Model Parameterization

There are three tunable parameters: i_{0,O_2}, β_{H_2} and k_{O_2} (see Eqs. 2.10, 2.12 and 2.45). i_{0,O_2} and β_{H_2} impact the local kinetics of the oxygen reaction in the anode and k_{O_2} impacts the oxygen crossover rate from cathode to anode. The tuning is aimed to minimize the value

Quantity	Value
Geometrical parameters	
Active MEA area S	50 cm^2
Anode channel depth $h_{ch,an}$	0.18 cm
Cathode channel depth $h_{ch,ca}$	0.10 cm
Cathode channel/Rib width $w_{ch/rib,ca}$	0.07/0.08 cm
Channel length l	7.27 cm
Membrane thickness δ_{mb}	25 μm
GDL thickness δ_{GDL}	300 μm
Physical parameters	
Catalyst loading L_{Pt}	$0.3/2 \times 10^{-3}$ $g\ cm^{-2}$
Electrochemical area of Pt γ_{Pt}	6×10^5 $cm^2\ g^{-1}$
Electrochemical area of carbon γ_C	6×10^6 $cm^2\ g^{-1}$
Concentration parameter for hydrogen β_{H_2}	1.2
Concentration parameter for oxygen β_{O_2}	1.0
Anodic transfer coefficient for hydrogen reaction α_{a,H_2}	1.0
Cathodic transfer coefficient for hydrogen reaction α_{c,H_2}	1.0
Anodic transfer coefficient for oxygen reaction α_{a,O_2}	0.6
Cathodic transfer coefficient for oxygen reaction α_{c,O_2}	1.0
Anodic transfer coefficient for carbon corrosion $\alpha_{a,C}$	0.25
Exchange current density of hydrogen reaction i_{0,H_2}	$1.7 \times 10^{-3} A\ cm^{-2}$
Exchange current density of oxygen reaction i_{0,O_2}	$2.6 \times 10^{-9} A\ cm^{-2}$
Exchange current density of carbon corrosion $i_{0,C}$	$2.5 \times 10^{-10} A\ cm^{-2}$
Equilibrium potential for hydrogen reaction $V_{H_2}^{eq}$	0 V
Equilibrium potential for oxygen reaction $V_{H_2}^{eq}$	1.23 V
Equilibrium potential for carbon corrosion V_C^{eq}	0.21 V
Scale factor for oxygen crossover k_{O_2}	0.72
Scale factor for nitrogen crossover k_{N_2}	2.0
Initial carbon loading per unit MEA area $m_{C,0}$	0.002 g cm^{-2}
Anode reference pressure $P_{i,AN}^*$, i=[H_2,O_2,vapor]	1.2755×10^5 Pa
Cathode reference pressure $P_{i,CA}^*$, i=[O_2,vapor]	1.2355×10^5 Pa
Number of meshes in numerical computation N	51
Operating parameters	
Cell temperature T	50°C
Inlet pressure at anode P_{AN}	4.5 psig
System pressure at cathode P_{CA}	4 psig
Duration of a cycle t	1020 s

Table 2.2 Geometrical, physical and operating parameters

of the following function:

$$f(i_{0,O_2}, \beta_{H_2}, k_{O_2}) = \sqrt{\frac{w_1 \Sigma_1^M (n_i^{sim} - n_i^{exp})^2}{M n_{ref}^2} + \frac{w_2 \Sigma_1^N (E_{cell}^{sim} - E_{cell}^{exp})^2}{N E_{ref}^2}} \tag{2.50}$$

where n_i^{sim}/n_i^{exp} and $E_{cell}^{sim}/E_{cell}^{exp}$ are the species molar fraction and cell voltage data from simulation and experiment, respectively. M/N indicates the amount of molar fraction/voltage data used for tuning, n_{ref}/E_{ref} is molar fraction/voltage reference (range of the tuned parameter), and w_1 and w_2 are weight factors because the tuning focuses on both molar fraction and voltage. Ideally, an optimization should be performed for Eq. 2.50 to find the optima. In this dissertation, however, a factorial study was conducted for simplicity by varying the three tunable parameters jointly to find the combination that gives the smallest value of Eq. 2.50. Refer to Table 2.3 for the tunable ranges and tuned values for i_{0,O_2}, β_{H_2}, k_{O_2}. The tuned i_{0,O_2} is close to the one in Ref. [36].

It is found that $i_{0,C}$ has very limited influence on the species concentration and cell voltage, although it directly affects the carbon corrosion rate. We do not have sufficient experimental data for tuning $i_{0,C}$ at this time. It should be ideally tuned against the CO_2 evolution rate, or concentration at the downstream of the cathode. The value of $i_{0,C}$ is taken from Ref. [36].

Quantity	**Range for tuning**	**Value**
Exchange current density of oxygen reaction i_{0,O_2}	10^{-5} – $10^{-12}\,A\,cm^{-2}$ [26, 35, 36]	$2.6 \times 10^{-9} A\,cm^{-2}$
Concentration parameter for hydrogen reaction β_{H_2}	0.5-1.5	1.2
Scale factor for oxygen crossover k_{O_2}	0.5-2.0	0.72
Power factor for remaining carbon q	0-4.0 [89]	1.5

Table 2.3 Tuned parameters

2.6.1 Experimental Setup

The experimental data of species molar fractions were collected using a gas chromatograph [66]. The setup is schematically shown in Fig. 2.5. A heated capillary tube was inserted into the last anode channel near the edge of the cell (3 cm from the bottom corner), it was then connected to an electrically actuated six-port rotational valve. A sample valve placed downstream from the six-port valve, once open, allowed for filling of the sample loop. After a sample was collected the six-port valve was rotated to close, and the high pressure carrier gas helium pushed the sample into the GC for analysis. The sample valve was opened for 1 s, during which ~300 μL of gas was removed from the anode channel. A

second Solenoid Valve, shown in the lower right hand corner of Fig. 2.5, was used to purge all of the N_2 from the cell. The flow rate during the purge was approximately 0.5 SLPM, and the purge duration was around 1 s in order to ensure that all of the accumulated water and nitrogen are removed from the channels. More details about the setup and experimental results can be found in [66].

The experimental results for comparison were obtained under the following conditions: the anode is dead ended and the cathode is flow through. The operating conditions for each case are indicated in the captions of the figure (i: current density in A cm^{-2}, T: temperature in °C, SR: cathode stoichiometry, RH: relative humidity of cathode supply). The anode/cathode pressure (absolute) is $1.2755\times10^5/1.2355\times10^5$ Pa for all cases. These operating conditions are also used to obtain the simulation results. The selected portions of the data to validate the model (Figs. 2.6-2.8) start from t_0=57495 s, 73786 s and 82940 s, respectively (see [66] for the entire data set). For each case, the membrane water content and local current density profiles at three locations (0.2, 0.5 and 0.9 fractional channel length) are plotted. The fractional channel length of 0.9 corresponds to the GC sample location, where the experimental data of molar fractions were collected.

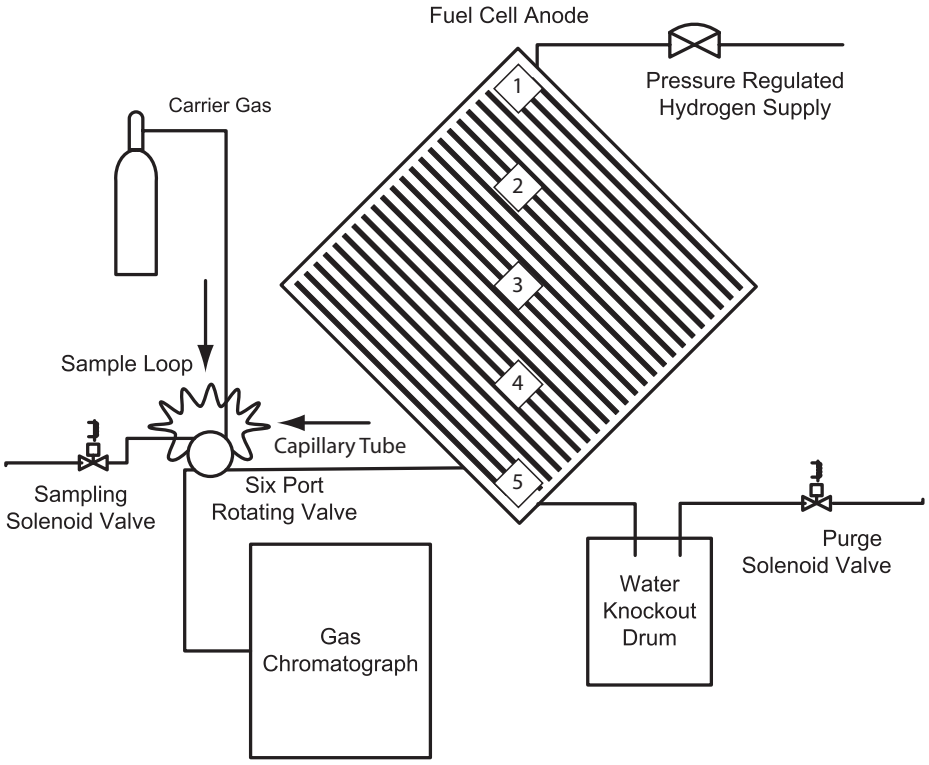

Figure 2.5 Illustration of the GC setup with six-port rotating valve. The marked locations 1 to 5 (from inlet to outlet) designate the positions of MEA samples which were used for SEM diagnosis, refer to [39] for more details of the degradation test.

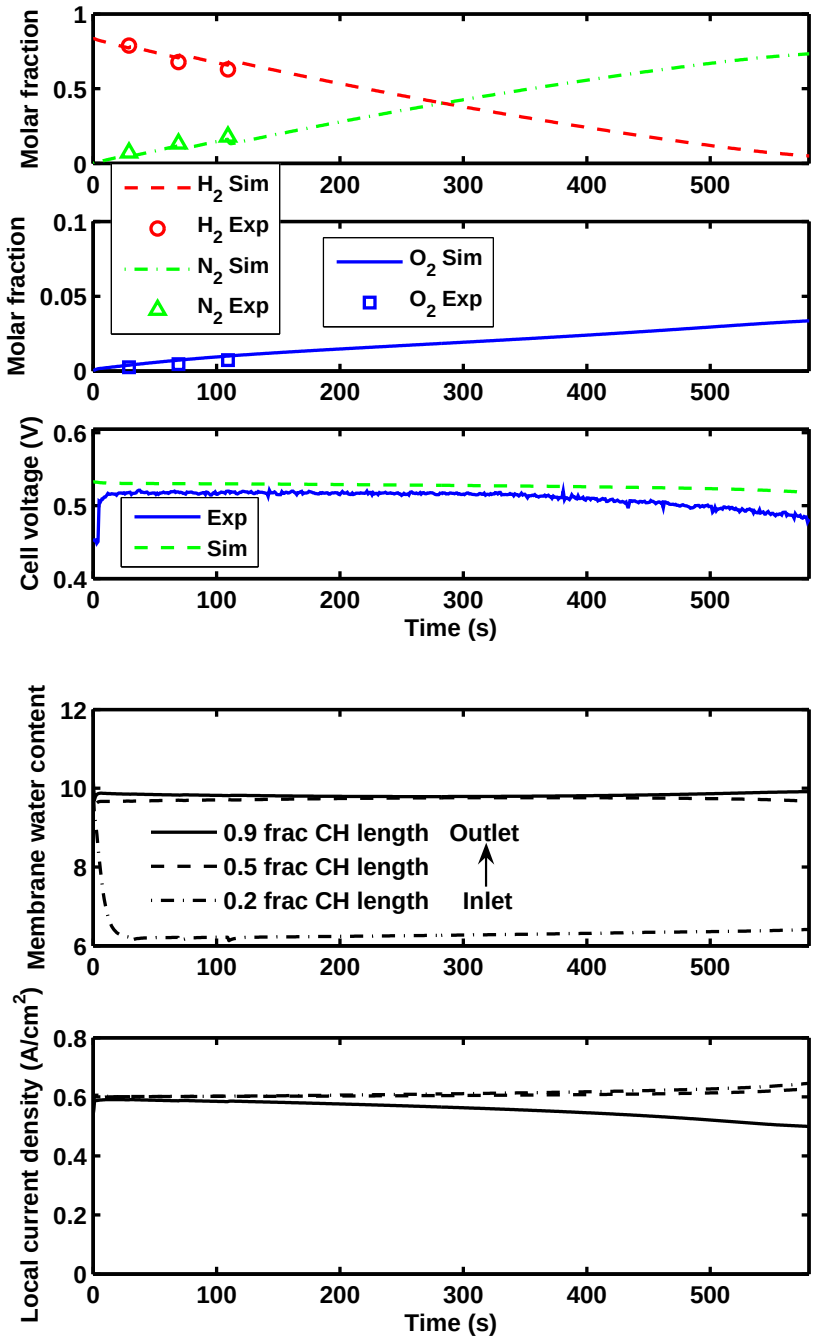

Figure 2.6 Top: Comparison of case 1: t_0=57495s, OPC: i0.6-T60-SR2-RH75. For molar fractions, markers are from experimental measurements and lines from simulation results. For cell voltage, blue solid line is from experimental measurements and green dashed line from simulation results. Bottom: Model predicted membrane water content and local current evolutions at selected channel locations (solid line represents GC sample location) for case 1.

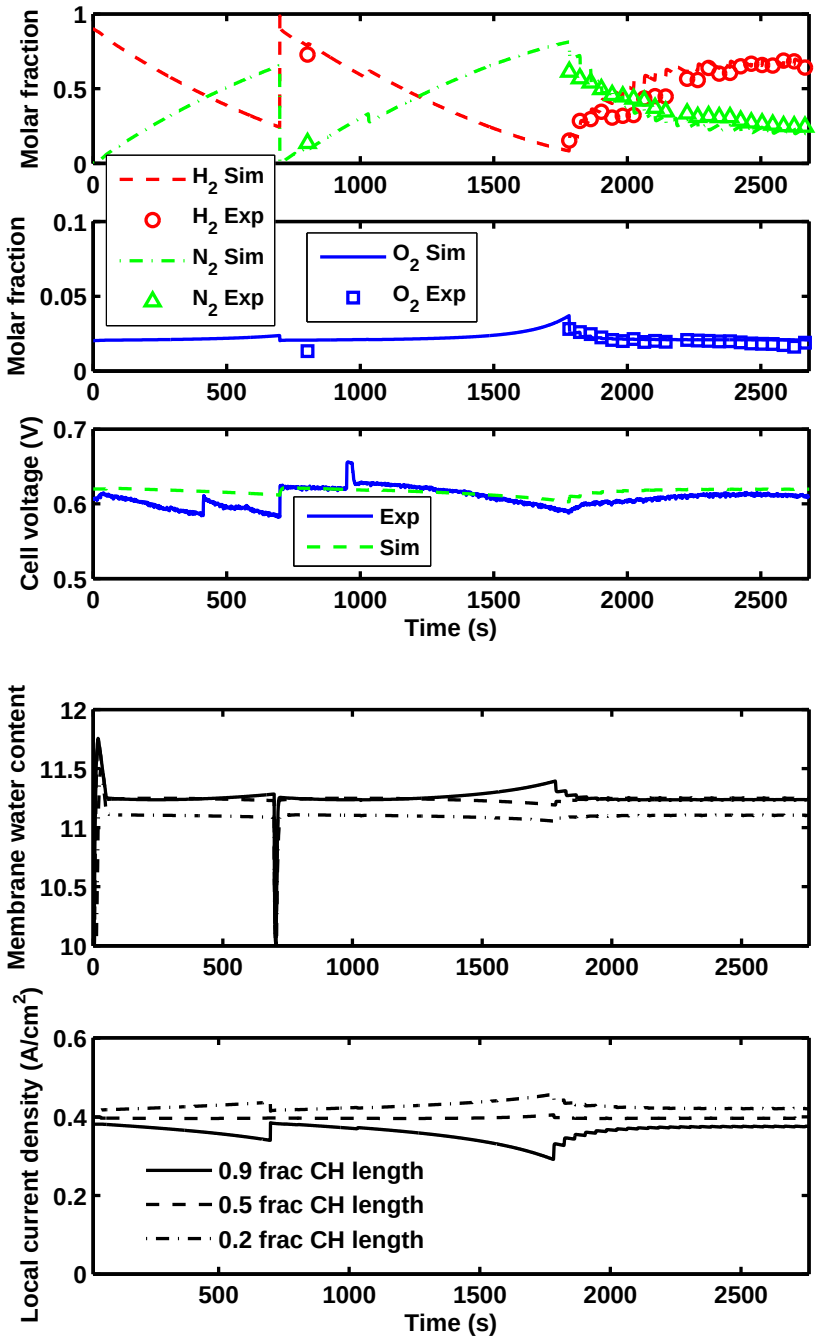

Figure 2.7 Top: Comparison of case 2: t_0=73786s, OPC: i0.4-T50-SR3-RH90. For molar fractions, markers are from experimental measurements and lines from simulation results. For cell voltage, blue solid line is from experimental measurements and green dashed line from simulation results. Bottom: Model predicted membrane water content and local current evolutions at selected channel locations (solid line represents GC sample location) for case 2.

2.6.2 Calibration Results

The simulated along-channel species concentrations agree well with the experimental data. In all three cases the model slightly over-estimates the cell voltage. This may be attributed

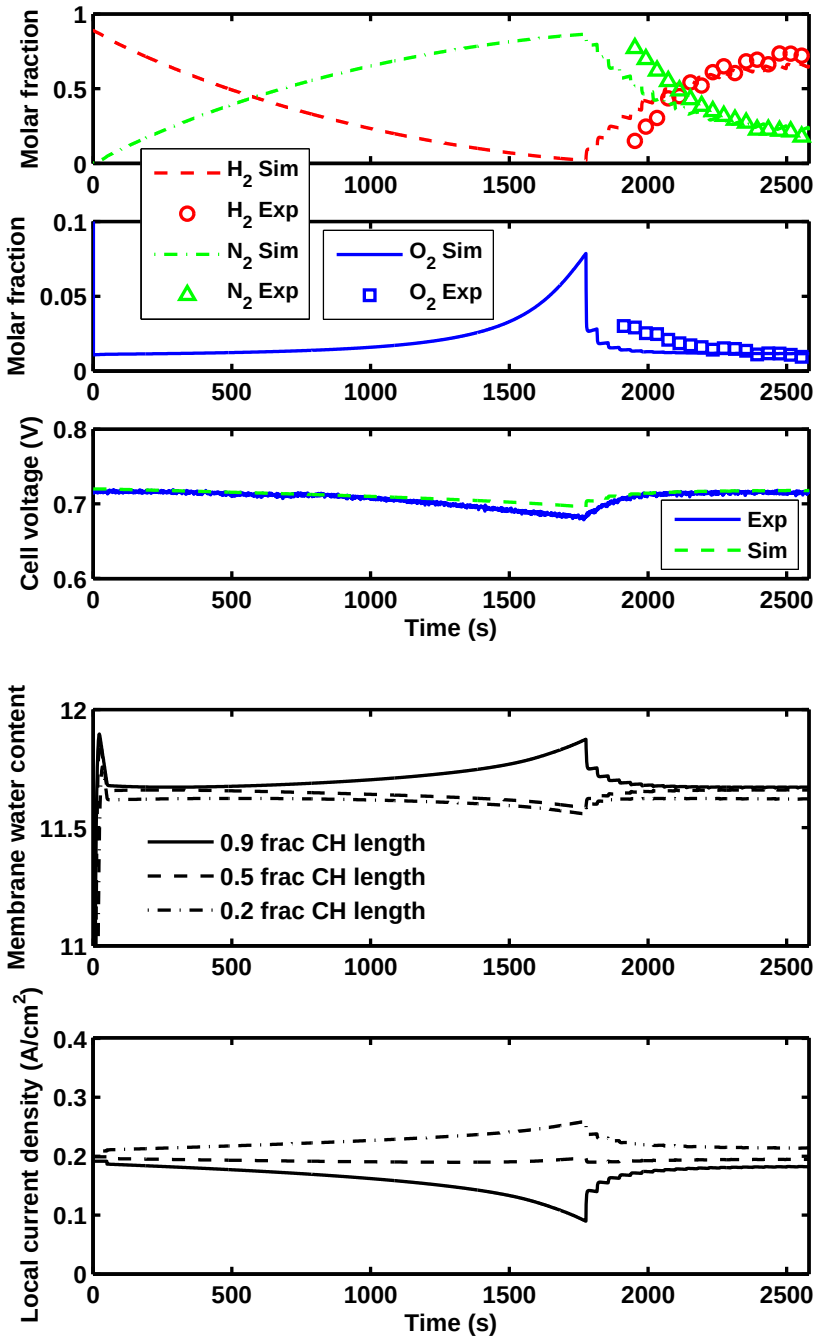

Figure 2.8 Top: Comparison of case 3: t_0=82940s, OPC: i0.2-T50-SR3-RH95. For molar fractions, markers are from experimental measurements and lines from simulation results. For cell voltage, blue solid line is from experimental measurements and green dashed line from simulation results. Bottom: Model predicted membrane water content and local current evolutions at selected channel locations (solid line represents GC sample location) for case 3.

to the influence of liquid water on the mass transport loss in calculating the cell voltage,

which is not captured by the present model. In cases 2 and 3, there exists discrepancies of nitrogen molar fraction at ~2000 s, which might be due to the liquid water plugging in the channel-end regions. Nitrogen does not participate in any reaction, however its transport can still be influenced by water plugging. Liquid water may block the outlet purge flow and prevent gas from entering the sample loop, resulting in measurement error. As time evolves over a cycle, the model predicts uneven local current distribution and membrane water content illustrated by the bottom plots of 2.8. The best agreement between simulation and experiments are observed for case 2 with current load of 0.4 A cm^{-2}. This result may be attributed to the relatively uniform local current and water distribution under this operating condition. Thus, the same operating conditions are used for discussion of the simulation results in the next section. The most uneven membrane water content distribution is observed in case 1, which is the result of high current load and low cathode inlet RH.

2.7 Simulation Results

In this section, we use the conditions of case 2 to investigate the spatiotemporal variation of species concentration and partial current density. The operating conditions are as follows: the temperature is fixed at 50°C, and the total current drawn from the stack is 20A (0.4 $A\,cm^{-2}$). The dead ended anode is supplied with dry (RH=0) H_2 and the cathode humidified air (RH=0.90) at a stoichiometry of 3. The tuned values in Table 2.3 and other parameter values in Table 2.2 are used for simulation. Every 1020 seconds, the solenoid valve at the anode outlet opens for 1 s to recover the cell voltage by releasing the accumulated nitrogen and water. The results reported in this section are obtained in one complete cycle from a fresh start following a purge (100% hydrogen in anode) up until the next scheduled purge at ~1020 s. Note that in the simulation, complete hydrogen starvation does not occur even in the channel end, because the anode is purged every 1020 seconds. This purge schedule is consistent with the validated case 2 shown in Fig. 2.7, in which the system is purged before severe fuel depletion occurs.

2.7.1 Species Concentration

The simulation results for the species molar fractions in both anode and cathode at selected times (100 s, 500 s and 1000 s) are shown in 2.9. At t=1000 s, severe hydrogen depletion ($<$5%) is observed within the bottom 20% of the channel in the anode, as hydrogen con-

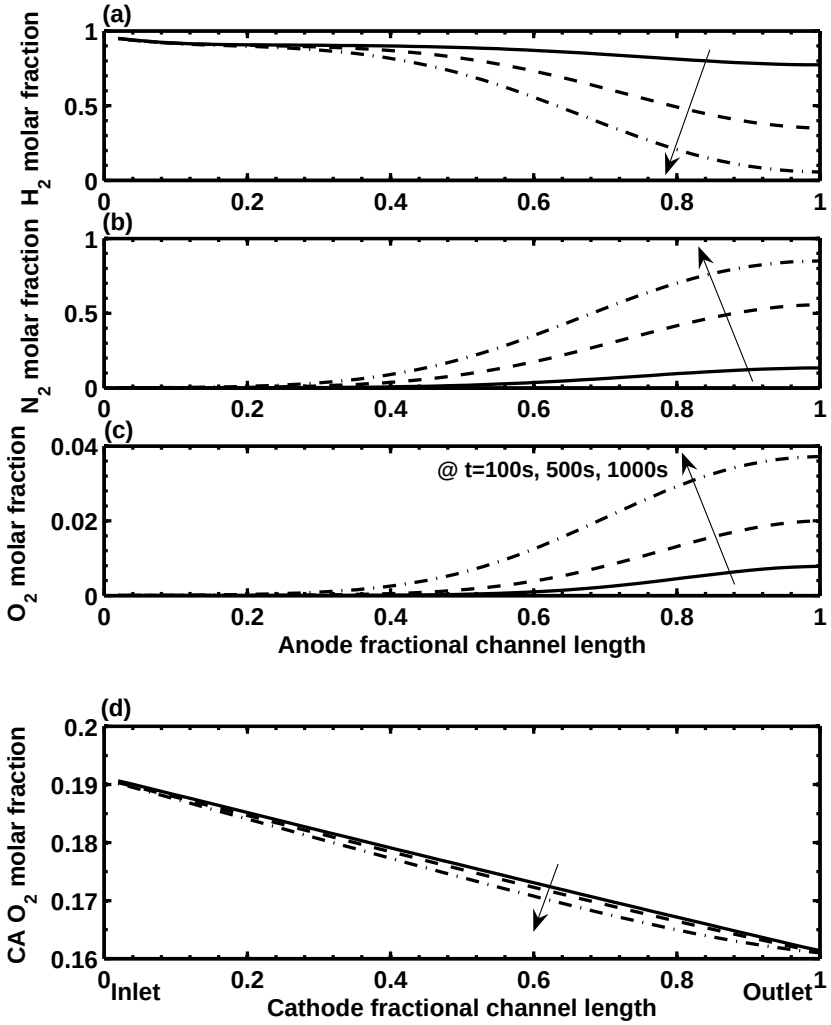

Figure 2.9 Molar fraction evolutions of (a)hydrogen/(b)nitrogen/(c)oxygen in the anode channel and (d) oxygen in the cathode channel.

sumed in reaction is displaced by gases and liquid water which cross over from the cathode. These effects have been discussed in our previous work [67, 66]. In this chapter the oxygen crossover, accumulation and its effect on carbon corrosion are emphasized. Overall, the molar fraction of oxygen is low ($<$5%) and it increases along the channel due to convection. There are two sources for oxygen in the anode: crossover from the cathode and water dissociation in the anode. 2.10 shows both the reactive and crossover fluxes of oxygen in the anode at selected times. The negative value of reactive fluxes indicates that the net effect of $O_2 + 4H^+ + 4e^- \leftrightarrow 2H_2O$ is moving forward and generating water (see also Fig. 2.11b). As indicated by the absolute values of reactive/crossover fluxes, the average rate of oxygen crossover is higher than oxygen consumption in the anode. The simulation therefore suggests that crossover oxygen reduces the rate of water dissociation, because the

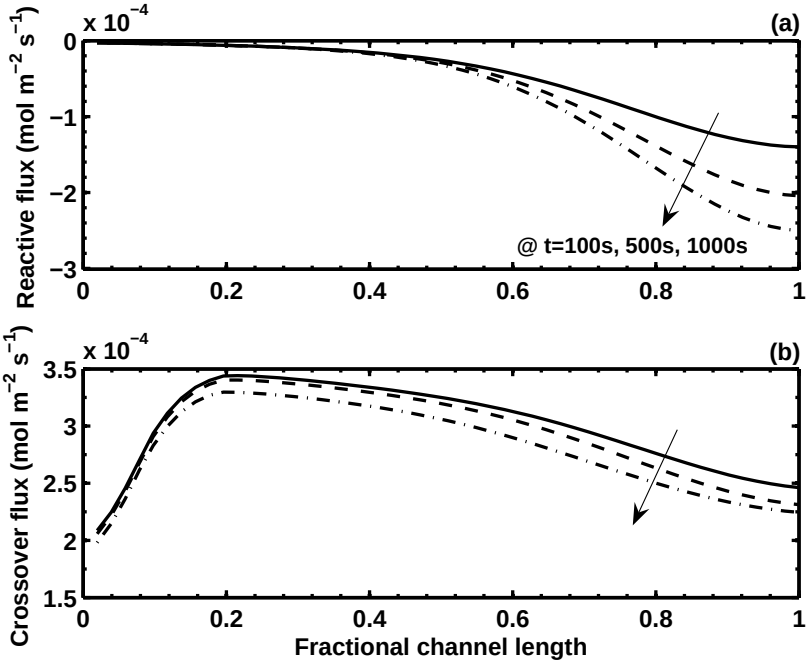

Figure 2.10 Evolutions of (a) reactive and (b) crossover fluxes of oxygen in the anode.

additional oxygen moves the equilibrium towards the direction of water generation. This increases the rate of carbon corrosion in the anode, since hydrogen ions are further consumed in the region of fuel depletion. However, the calculated carbon corrosion rate in the anode is still negligible, as shown in Fig. 2.11.

Examining the cathode molar fraction plot (subplot (d) in Fig. 2.9) we observe that the oxygen profile is almost linear at t=100 s, being a result of relatively uniform local reaction rates. At t=1000 s, the curve shows non-linear behavior due to the uneven local current.

The partial current density evolutions are shown in Fig. 2.11. As expected, the current density of hydrogen reaction is decreasing with time at the channel-end region, because accumulated nitrogen and water displace hydrogen. The local current profile becomes more uneven as time evolves. The magnitude of $i_{C,AN}$ (~$10^{-7} A/cm^2$) from the simulation indicates that carbon corrosion at the anode is negligible. The cathode carbon corrosion rate is much higher, see Fig. 2.13 and discussion therein.

2.7.2 Interfacial Potentials

The variation of membrane phase potential in the anode is a direct result of the presence of oxygen. In the model, the membrane phase potential at anode/cathode enters into the Bulter-Volmer expression for the kinetic of each partial reaction (Eqs. 2.8-2.11). Fig-

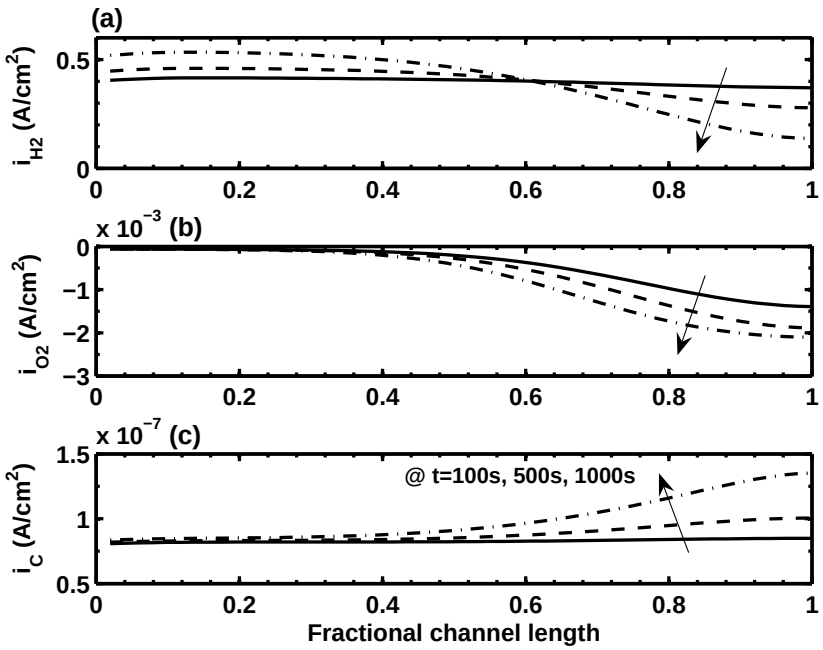

Figure 2.11 Anode partial current density evolutions of (a) hydrogen, (b) oxygen and (c) carbon reactions.

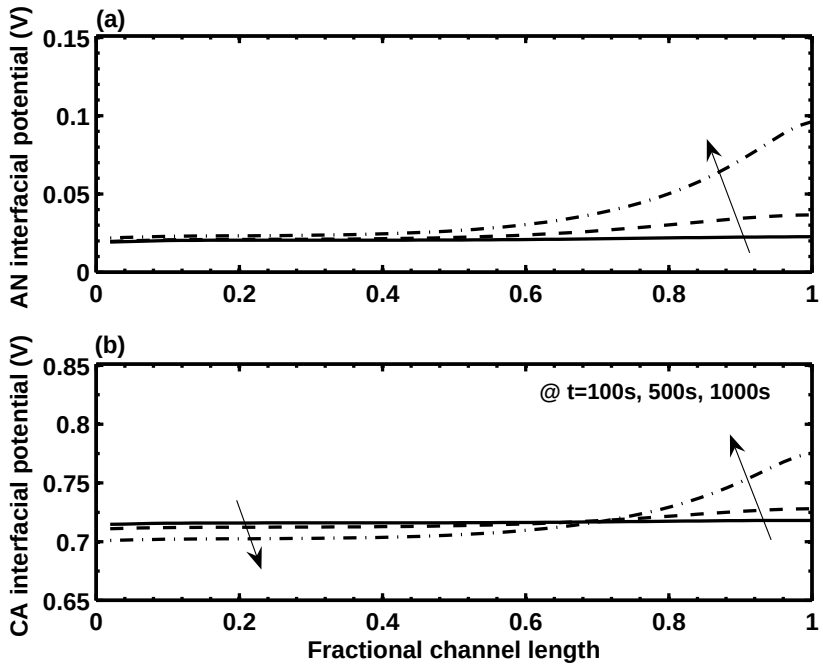

Figure 2.12 Evolutions of (a) anode and (b) cathode interfacial potentials. The cathode interfacial potential decreases near the channel inlet because of the increase current density in this region (Fig. 2.11(a)). The increase at the outlet is due to the anode side potential shift in the same region.

ure 2.12 shows the evolution of both anode and cathode interfacial potentials. The anode interfacial potential is equal to the absolute value of membrane phase potential at the anode, whereas the cathode potential depends on the overall cell voltage (see 2.15 and 2.16). During normal operation, with sufficient hydrogen supply everywhere, ϕ_{AN} should be slightly negative (very close to zero). After 1000 s, ϕ_{AN} decreases to approximately -0.1 V in the end region. The decrease of ϕ_{AN} along the channel promotes the water dissociation and carbon corrosion reactions at the anode. The drop is continuous over the whole channel length, as opposed to the sudden drop due to a H_2/O_2 boundary induced during start-up/shutdown [35]. Similar hydrogen molar fraction and ϕ_{AN} profiles, featuring a gradual drop, were reported by Weber [103], except that the end region was completely out of fuel.

Membrane phase potential at the cathode (Eq. 2.16) is not plotted since the potential drop through membrane is only ~0.01 V (estimated by $i\delta_{mb}/k_{mb}$, i=0.4 $A\,cm^{-2}$). The interfacial potential at the cathode, $V_m^{CA} - \phi_{CA}$, is shown in Fig. 2.12. This interfacial potential directly determines the carbon corrosion rate at the cathode. The predicted interfacial potentials are not as large as in start-up/shutdown case [35] for two reasons. First, the cell voltage in an operating cell is lower than the open circuit voltage due to thermodynamic losses. Therefore, the resulting metal phase potential at the cathode is normally less than 1 V (see Eq. 2.15). The cell voltage is decreasing during a cycle of DEA operation, which offsets the effect of the decreasing membrane phase potential. Therefore, a cell under operation, either with flow through or DEA, would normally experience much less severe carbon corrosion compared with an idle one in which H_2/O_2 boundary builds up. The second reason is that in simulation the anode is purged before complete fuel starvation. A postponed purge may lead to higher cathode interfacial potential and carbon corrosion rate.

2.7.3 Carbon Corrosion

The predicted local cathode corrosion rates in selected cycles are plotted in Fig. 2.13(a). As hydrogen becomes depleted in the anode end region, the cathode end region endures the highest corrosion rate, which is caused by the increased cathode interfacial potential in this region (see Fig. 2.12). The cathode carbon corrosion rate at the end region is twice as large as the inlet right before the purge. However, when the hydrogen depletion is mild, the corrosion rate is much more uniform. The carbon corrosion rate predicted by the model is higher than other rates found in the literature [88, 104]. Unfortunately, a further analysis becomes impossible since the specifications of carbons used in those works are not disclosed.

but the carbon corrosion rate in the model has not been rigorously tuned. It can be tuned

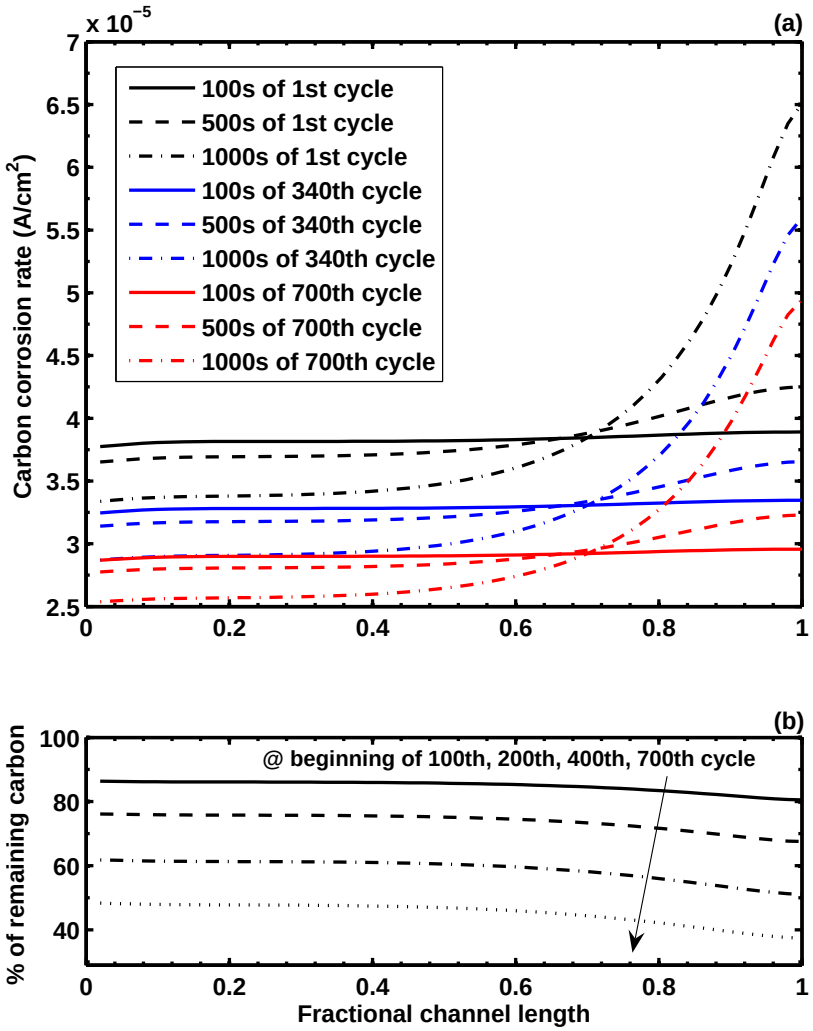

Figure 2.13 (a) Evolution of the cathode carbon corrosion rate in the 1st, 340th and 700th cycle, respectively. The overall corrosion rate decreases with time due to the loss of catalytic sites. (b) The remaining carbon evaluated locally by the percentage of initial loading after 100, 200, 400 and 700 cycles, respectively.

by the parameters q in Eq. 2.17, $i_{0,C}$ and $\alpha_{a,C}$ in Eq. 2.14 once more data are collected, particularly the measurement of CO_2 concentration at the cathode.

The relationship between reactant distribution and carbon corrosion during DEA operation is captured by this physics based and tunable model. Since the connection between carbon loss and voltage drop over time is included in the model, it can be used to develop control laws to prolong stack life. The percentage of remaining carbon is shown in Fig. 2.13(b). The initial carbon loading is assumed to be uniform. The uneven corrosion rate leads to increased carbon loss along the length of the channel. The non-uniformity of remaining carbon along the channel is not as severe as the local corrosion rate before the

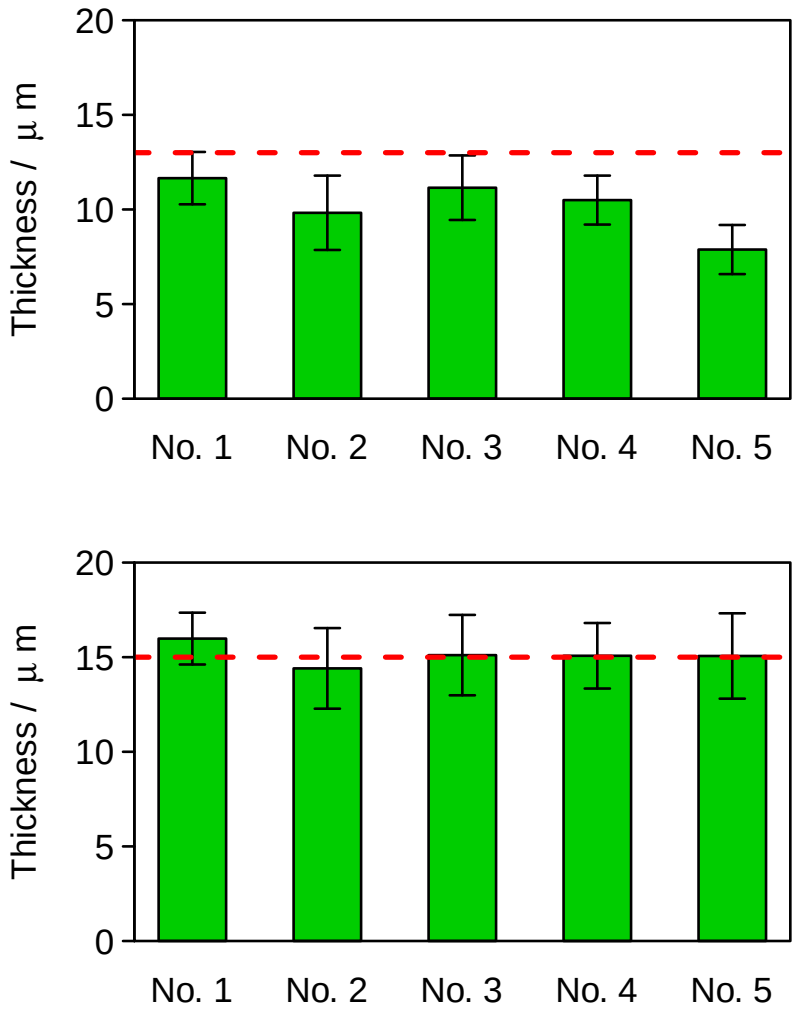

Figure 2.14 Measured electrode thickness of the aged MEA, top: cathode and bottom: anode. The dotted red lines denote the original thickness of electrodes at cathode and anode. Numbers 1 to 5 refer to the sample positions shown in Fig. 2.5. More details of the degradation test are available in [39].

purge because the local corrosion rate does not increase until a nitrogen blanketing front in the anode channel begins to develop. If the cell could be purged before the corrosion rate at the end region starts to spike, then the catalyst durability may be greatly improved.

The local percentage of remaining carbon at the beginning of 100th cycle is consistent with our experimental measurement of the aged MEA shown in Fig. 2.14. The data shown in Fig. 2.14 also confirm that the anode carbon corrosion is negligible compared with cathode. The trend at location 2 seems to be inconsistent with the model prediction. This could be attributed to measurement error and/or other degradation mechanisms not included in the model. More experimental data are being collected to clarify the spatial variability, and

initial results are reported in [39]. Nevertheless, the carbon corrosion rate can be independently tuned since it has negligible influence on the species transport, because the current density of carbon corrosion is at least 1000 times smaller than the main reaction (Eq. 2.1).

2.8 Conclusions

In this chapter, we developed an along-channel model to predict the carbon corrosion in DEA operation. The membrane phase potential in the DEA mode exhibits a gradual drop along the channel, as compared to the start-up/shutdown case where the sharp boundary between fuel and oxidant develops in the anode channel. Therefore different modeling equations for the gas transport in the channels are required to describe the corrosion behavior. This model captures the effect of nitrogen accumulation and current density distribution on carbon loss. The carbon loss is related to a decrease in the number of active catalytic sites via a power law correlation of the amount of carbon remaining in the catalyst layer. The model predicts the non-recoverable voltage loss during DEA operation associated with decrease in carbon corrosion rate as the catalyst layer is thinned.

Experimental data including GC samples and cell voltage are compared with the model prediction and demonstrate satisfactory agreement at low current loads. A snapshot of the temporal evolution right before the purge, shows that the carbon corrosion rate at the end channel region is at least twice as large as the inlet region. The time evolving terminal cell voltage directly affects the interfacial potential at the cathode. Fortunately, the gradual voltage decay, associated with higher local hydrogen current density, during DEA operation reduces the cathode carbon corrosion rate.

In the future the model can be improved by including the effects of liquid water, Pt sintering, mass transport limitations due to changes in catalyst layer composition, and membrane degradation. The addition of these factors may improve the model prediction of non-recoverable voltage drop over time, particularly at high operating current. The present model captures the effect of nitrogen accumulation and current density distribution on carbon loss. The carbon loss is related to a decrease in the number of active catalytic sites via a power correlation of the amount of carbon remaining in the catalyst layer. The model predicts the non-recoverable voltage loss during DEA operation associated with decrease in carbon corrosion rate as the catalyst layer is thinned. The voltage prediction can be used to develop better purge scheduling and closed loop estimation. If the cell is purged before the corrosion rate at the end region starts to spike, then the catalyst durability may be greatly improved. Purge scheduling that accounts for carbon corrosion through a well calibrated

model can balance the hydrogen loss occurring during a purge with the durability issues associated with delaying a purge event. Future work includes collecting data on cell voltage and CO_2 evolution to further validate and tune the actual carbon corrosion rate.

Chapter 3

Optimization of purging cycle for dead-ended anode fuel cell operation

Generally, in order to reduce the cathode carbon corrosion, severe anode fuel starvation should be avoided by increasing purge frequency and duration, which may lead to substantial loss of hydrogen fuel and system efficiency. An optimization of the DEA fuel cell operating scheme, considering both durability and hydrogen economy, is thus necessary.

Optimization of the purge interval and cycle duration, for a given operating power, can increase the fuel cell efficiency which depends on three interrelated objectives, namely, the hydrogen loss during the purge, the average voltage output between the purges, and the voltage decrease due to the carbon corrosion caused by hydrogen starvation over the life-time of the DEA operation.

In advancing past results, this chapter shows how the purge cycle can be optimized for better efficiency in DEA operation by considering the impact of carbon corrosion. For this optimization, a model capturing the liquid water and nitrogen accumulation in the anode is needed to accurately describe the evolution of corrosion rate and the amount of hydrogen wasted during the purge. The optimization process is first defining a target range of purge intervals based on the physical constraints of the actuator and the model-based prediction of the species concentration distributions. The search of optima is performed then by scanning the target domain to quantify the trade-off between wasted hydrogen and reducing the corrosion rate over a long time horizon.

3.1 Introduction

During DEA operation, nitrogen and liquid water accumulate in the anode channel, causing a gradual drop in cell voltage over time [66, 105]. Purging of the anode channel recovers the voltage by removing the accumulated nitrogen and water. A cyclic voltage behavior can thus be observed when a periodic purge schedule is applied, as illustrated in Fig. 3.1.

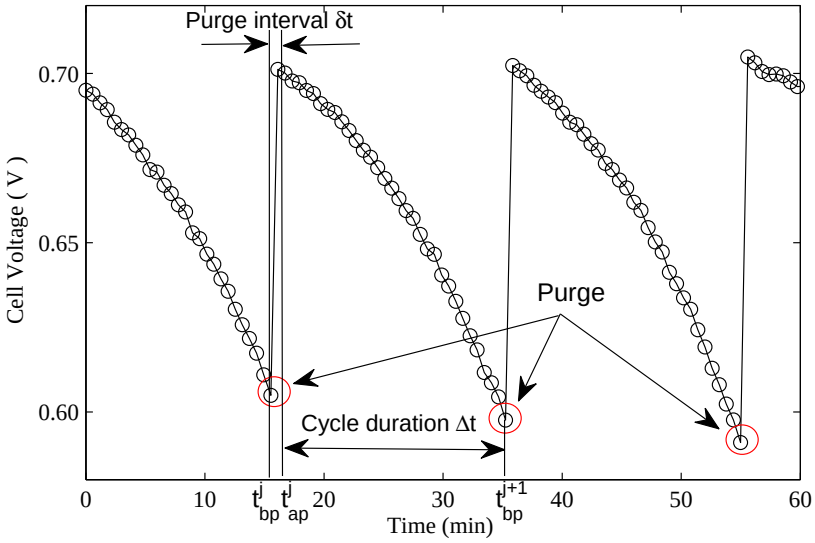

Figure 3.1 Representative voltage cycles during the DEA operation. t^j_{bp} is the end of the jth DEA cycle (the moment right before the jth purge) and t^j_{ap} is the beginning of the $(j+1)$th cycle (the moment right after the jth purge). Purge interval δt, which equals to t^j_{ap}-t^j_{bp}, is controlled by a solenoid valve downstream of the fuel cell anode. Cycle duration, Δt, is the amount of time between the end of the proceeding purge, t^j_{ap} and the start of the subsequent purge, t^{j+1}_{bp}. The accumulation of nitrogen and liquid water in the anode channel between purges is responsible for the recoverable voltage loss in a DEA cycle.

If allowed to continue without purging, the accumulation of nitrogen and liquid water in the anode channel during DEA operation would lead to local fuel depletion or starvation, triggering corrosion of the carbon as catalyst support in the cathode. Cathode carbon corrosion is a concern because it causes irreversible loss of fuel cell voltage and decreases the stack lifetime. In our recent work [68] the spatio-temporal carbon corrosion rate due to the elevated cathode interfacial potential during DEA operation has been studied via simulation. In addition, the uneven local current and membrane water content during DEA operation may expedite membrane degradation including crack/tear, pin-hole and polymer decomposition [41, 40]. The impact of degradation on cell terminal voltage and therefore efficiency over the entire lifetime of the cell, is an important consideration for purge scheduling. In this chapter, we aim to elucidate the connection between purge scheduling, degradation and efficiency over the entire cell lifetime.

There are many prior publications in fuel cell optimization [106]. Some focus on the component design such as flow field [107, 108] and electrode [109, 110] and some on the operating schemes [111, 112]. Usually, the objective of optimization is to maximize energy output or efficiency [113, 114]. These prior works are based on flow-through operation of the fuel cell. For DEA operation, early works mainly focus on reducing hydrogen loss

or increasing power output via optimization of a specific operating parameter. Hikita et al. [115] investigated the optimum humidification for a DEA cell according to current density, as well as the influence of operating pressure on the power generation characteristics. Dumercy et al. [116] developed a stack model to calculate the optimal purge frequency for a three-cell stack with DEA in order to achieve satisfactory power output. Himanen et al. [117] studied the influences of hydrogen pressures, humidification conditions and purge valve duty cycles on the performance of an anodic dead-end mode PEM fuel cell with free-breathing cathode. In a recent study of DEA operation by Choi et al. [118], hydrogen pulsation is utilized to reduce the vapor partial pressure in the anode, thereby minimizing the purge frequency and associated hydrogen loss. The dynamic performance of a stack with near-dead-ended anode in a vehicular drive system was modeled by Dehn et al. [119]. They found that an increase in anode pressure is beneficial for near-dead-ended anode operation and does not lower the efficiency of the fuel cell system. Yang and Shi [120] designed a six cell stack, with dead-ended anode and air-breathing cathode, to achieve uniform stack performance and high efficiency. Mokmeli and Asghari [121] investigated the proper purge time to achieve the minimum pressure fluctuations, minimum voltage loss and minimum hydrogen waste by mathematical modeling and analysis. Their work, however, does not focus on the cell efficiency in DEA operation. These early works aim to improve either the power output or the hydrogen loss; however, the connection between these two factors has not been studied thoroughly. Finally, the degradation of a stack with DEA, which is critical for automotive application, has not been investigated in these works.

The objective of this chapter is to optimize the efficiency of a DEA fuel cell via purge scheduling while considering the performance degradation due to carbon corrosion. The optimization is performed on the purge interval and cycle duration shown in Fig. 3.1. Operating conditions such as current load also influence both fuel cell efficiency and degradation; however for a portable application these conditions are usually determined by the power requirement and thus considered parameters in this study. The optimization is performed based on the simulation results using a validated two-phase, 1+1D model, which gives more accurate prediction of the purge flow behavior compared with those early models in literature. In the following sections, we will define the cost function and target range for purge interval, present the model, and investigate the influences of purge interval and cycle duration on the cathode carbon corrosion, power output, hydrogen loss, and lifetime efficiency of a DEA cell.

3.2 Objective for Optimization (Cost Function)

The objective of this work is to find the purge interval and duration that maximize the efficiency η for a given power level. The DEA cell efficiency, which considers the hydrogen loss during the purge but excludes the BOP components, can be described by:

$$\eta = \frac{\int_0^{t_{tot}} E_{cell} iA dt}{\Sigma_1^m \Delta h_f (Q_{rxt}^{H_2} + Q_{loss}^{H_2})} \tag{3.1}$$

where Δh_f is the enthalpy of formation of hydrogen fuel in J/mol. The cell is operated under a galvanostatic load condition so that the current is constant. The cell voltage E_{cell} is decreasing with time as shown in Fig. 3.1, therefore integration over a cycle is needed to evaluate the total energy output. The voltage drop within a cycle is reversible, which can be recovered by a purge. The irreversible voltage decay due to carbon corrosion is also captured since the total operating time, t_{tot}, represents multiple cycles (Section 3.4.1). Specifically, t_{tot} equals to $m\Delta t$, where m is the number of DEA cycles. By using different m values, one can either evaluate the efficiency from a single cycle and the subsequent purge (Section 3.5.3), or multiple cycles to reflect the influence of cell degradation (Section 3.5.4). The efficiency η is therefore defined on the lifetime of a DEA cell.

3.2.1 Effects of Cycle Duration and Purge Interval on Efficiency

The DEA cell efficiency is adversely affected by the amount of hydrogen fuel expelled during the purge. The hydrogen loss during the purge depends on many factors, including the anode pressure, temperature, purge interval and the condition of channel flooding and nitrogen blanketing.

The hydrogen loss in mol at every purge event is calculated by:

$$Q_{loss}^{H_2} = \int_{t_{bp}^j}^{t_{ap}^j} \frac{W_{total}(t,L) n_{H_2}(t,L) P_{AN}}{RT} dt \tag{3.2}$$

where n_{H_2} is the hydrogen molar fraction at the end of anode channel (y=L). The functional dependence of W_{total}(y=L) on time is implicit, since W_{total} is expressed as a function of gas composition at the channel end as shown in Eq. 3.21.

The purge interval can be controlled to achieve $Q_{loss}^{H_2} = 0$, that is, the purge only releases accumulated water and nitrogen at the channel end and it stops when or before the hydrogen front (y_{H_2} in Fig. 3.2) reaches the channel end. However this purge schedule may not give the best overall efficiency due to remaining trapped nitrogen and water in the an-

ode channel. The optimization methodology developed in this chapter can elucidate which purge interval and cycle duration will give the best efficiency.

The 2nd term in the denominator in Eq. 3.1 represents the total hydrogen consumed during a cycle in mol and is calculated from the current density setpoint:

$$Q_{rxt}^{H_2} = \frac{iA}{2F}\Delta t \tag{3.3}$$

where i is the current density in A cm^{-2}, A is the effective MEA area, and F is the Faraday constant. If the hydrogen loss is not considered, i.e., $Q_{loss}^{H_2}$=0, Eq. 3.1 represents the thermodynamic efficiency, that is, the efficiency of the fuel cell electrochemical conversion.

The efficiency defined in Eq. 3.1 depends on the current setpoint, or the power output in a DEA cycle, which is defined by:

$$P_{DEA} = \frac{1}{\Delta t}\int_{t_{dp}^{j}}^{t_{bp}^{j+1}} E_{cell} iA dt \tag{3.4}$$

where the right-hand-side integral represents the total energy output in a DEA cycle. Due to the carbon corrosion and associated voltage degradation, the power/energy output in a cycle decreases with time. The power output P_{DEA} is defined on the initial cycle when the system reaches periodic equilibrium. Other operating conditions such as cathode pressure, relative humidity and stoichiometry ratio can also affect the power output by changing the voltage evolution over time.

3.2.2 Target Range for Purge Interval

In DEA operation, a stratified channel distribution with water and nitrogen in the end is expected for a vertically oriented (inlet at the top) cell. As shown in the upper graph of Fig. 3.2, there is accumulated nitrogen and water in the channel end right before the purge, which leads to local (end of channel) hydrogen starvation and voltage decay. The minimum purge interval, δt_1, places the hydrogen starvation front (y_{H_2}) right at the channel end, i.e., hydrogen becomes available in the whole channel after the purge without any hydrogen loss during the purge. As illustrated in the lower graph of Fig. 3.2, with an increasing purge interval the hydrogen concentration in the channel becomes higher after the purge, and the power output in the subsequent cycle would be larger, although there is some hydrogen loss during the purge. Finally, the maximum purge interval, δt_2, should fully restore the hydrogen in the channel, i.e., the hydrogen molar fraction (n_{H_2}) exactly reaches unity in the whole channel, leading to the highest power output in the subsequent cycle.

These minimum and maximum purge intervals (δt_1 and δt_2) constitute the target range for a purge.

The purge is performed by a solenoid valve at the downstream of the anode outlet. There is physical opening/closing time for the solenoid valve; hence δt_1 needs to be further constrained by a minimum operating time constant t_{SV} of the solenoid valve. In practice, this physical opening/closing time is between 0.01 and 0.5 second. A small value 0.02 s is chosen for t_{SV} in this chapter to illustrate the optimization results. The practical target range for purge interval becomes [max(t_{SV}, δt_1), max(t_{SV}, δt_2)].

It is necessary to demonstrate the significance of target range for purge interval. Fig. 3.3 shows the efficiency as a function of purge interval spanning from 20 ms (t_{SV}) to 900 ms for two selected cycle durations. In the enlarged view, the efficiencies within the target range are presented. It can be seen that the efficiency exhibits very small variation within the target range, as well as a non-monotonic change with increasing purge interval. The efficiency reaches maxima with the target range but drops rapidly as the purge interval increases beyond the target range. Therefore, identifying the target range is an important step for optimizing efficiency.

3.3 Model Presentation

In previous work [66, 68], we have developed a 1-D (along-channel), single-phase transient model to study the nitrogen front evolution and associated carbon corrosion in DEA operation. The model predicted spatio-temporal evolutions of species concentration and carbon corrosion rate have been tuned using the gas chromatography [66] and electrode thickness measurement [39]. The physics based model can also predict the cell equilibrium observed during DEA operation [122]. In this chapter we extend our model to capture the liquid water accumulation in the channel end. A model of the channel liquid water is needed because the water impedes the flow of gases during the purge, and a longer purge interval is required to clear the channel when liquid is present.

The model inputs are the nominal current I, cathode inlet relative humidity (RH), and cathode stoichiometry ratio (SR). The cell temperature T and Anode(AN)/Cathode(CA) inlet pressures P_{ca}/P_{an}, are fixed parameters in the model but may be adjusted prior to simulation for different experimental conditions. The model outputs are cell voltage, local current density, molar fraction of each species in the anode, membrane water content, anode/cathode liquid saturation in the catalyst layer, liquid water volume fraction in the anode channel, and the liquid front location in the anode/cathode GDL. The cell voltage is a scalar

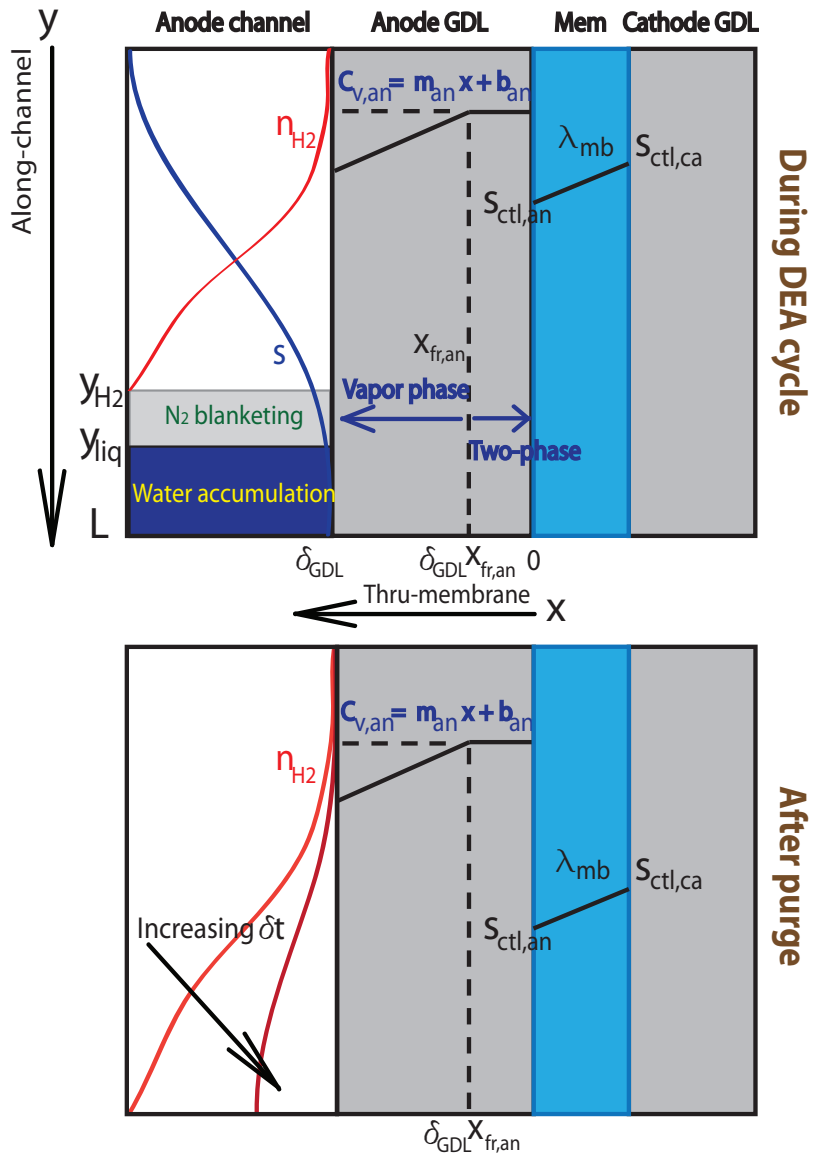

Figure 3.2 A schematic illustrating the modeling domain (not to scale). Species molar fraction (n_i), liquid volume fraction in the channel (s), liquid front in the GDL ($x_{fr,an}$, $x_{fr,ca}$), membrane water content (λ_{mb}) and liquid saturation in the catalyst layer ($s_{ctl,an}$, $s_{ctl,ca}$) are the distributed states along the channel. The liquid water fully occupies the channel when the volume fraction reaches unity. Nitrogen blanketing also contributes to the hydrogen starvation in the channel end. A purge can release the accumulated water and nitrogen, thus restoring the hydrogen concentration in the channel. Increasing purge interval leads to higher average hydrogen concentration right after the purge.

quantity while the other outputs represent the vector of distributed values along the channel (y direction). Fig. 3.2 illustrates the modeling domain; the cathode channel is not modeled for simplicity. Since the model is developed based on our published works [66, 65, 68],

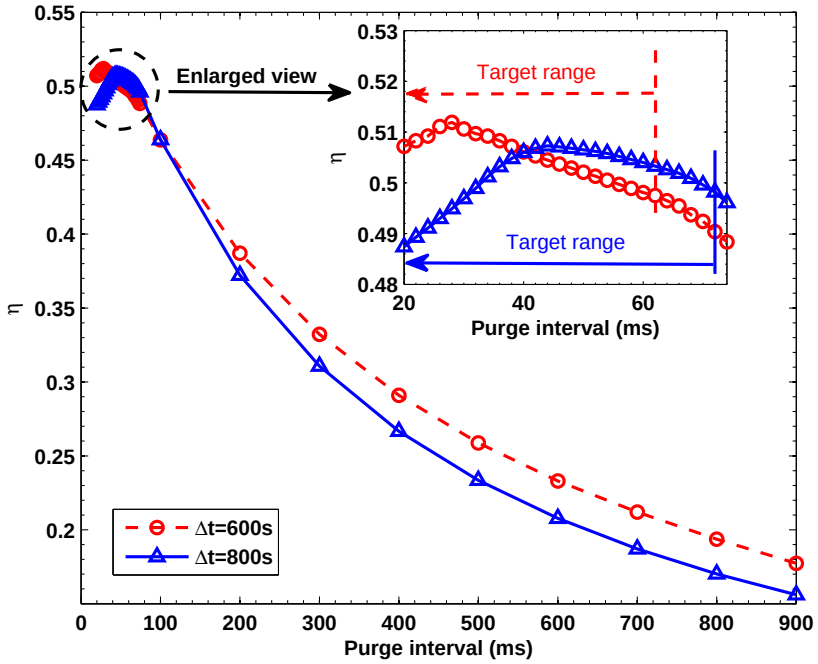

Figure 3.3 The lifetime efficiency with different purge intervals at two selected cycle durations. The definition of lifetime is discussed in Section 3.4. The operating conditions are: current density 0.6 A/cm^2, cell temperature 50 °C, cathode stoichiometry ratio 3, and RH 100%. Monotonic and rapid drop of efficiency has been observed as the purge interval increases beyond the target range.

those equations from prior model framework are summarized in Tables 3.1 and 3.2 with references.

The initial model assumptions can be summarized as: 1) the model is isothermal; 2) 1+1 D (along-channel + through-membrane); 3) the cell degradation is solely due to carbon corrosion in the cathode. More detailed assumptions on each subsystem are discussed in associated subsections.

In Eq. 3.5 in Table 3.1, the volume fraction term, $1-s$, is introduced to account for the change of mass due to the volume change from liquid accumulation. When s=0, this equation reduces to the single phase equation of material balance. A similar approach to handle the water phase change in the transport equation can be found in [62, 123]. Only three of the four gas components are independent in this modeling framework. We chose to model the mole fractions of nitrogen (n_{N_2}), oxygen (n_{O_2}) and water vapor (n_V) as our dynamic states. The anode pressure, P_{an}, is assumed to be constant since it is set by an upstream pressure regulator during the DEA operation.

The impact of carbon corrosion on the exchange current density in the Butler-Volmer equation is captured by the effective factor, ε_C in Eq. 3.18, which models the catalytic site

Table 3.1 Summary of modeling equations

State/Variable	Governing Equation	Reference	
n_i	$\frac{P_{an}}{RT}\frac{\partial(1-s)n_i}{\partial t} = -\frac{\partial}{\partial y}(J_i + n_i N_t) + r_i$ for $i \in [\mathrm{N_2}, \mathrm{O_2}, \mathrm{Vapor}]$	[66, 68]	(3.5)
s	$\rho_w \frac{\partial s}{\partial t} = \rho_w D_s \frac{\partial^2 s}{\partial y^2} - \rho_w \frac{RT}{P_{AN}} \frac{\partial [f(s) N_t(y)]}{\partial y} + M_w (r_{V,cond} + \frac{N_{l,an}(x = \delta_{GDL})}{d_{ch}})$		(3.6)
λ_{mb}	$\frac{\partial \lambda_{mb}}{\partial t} = \frac{EW}{\rho_{mb}\delta_{mb}}(N_{w,ca,mb} - N_{w,an,mb})$	[65]	(3.7)
x_{fr}	$\frac{\partial x_{fr,an}}{\partial t} = K_L N_{l,an}$	[65]	(3.8)
m_C	$\frac{\partial m_C(y,t)}{\partial t} = -\frac{M_C i_{C,CA}}{4F}$	[68]	(3.9)
$s_{ctl,an}$	$\lambda_{an} = (1 - s_{ctl,an})\lambda^* + s_{ctl,an}\lambda_{max}$	[65]	(3.10)
E_{cell}, ϕ_{AN}	$i_{AN} + i_{CA} = 0, i_{fc} = \frac{1}{L}\int_0^L i_{AN} dy$	[68]	(3.11)

loss. The power factor q is a tuned parameter in [68]. Incorporating ε_C in carbon corrosion kinetics leads to an asymptotic drop of corrosion current with constant potential. A more complicated model of Pt loss (such as dissolution and mitigation [33, 34]) has not been included in this work, and the carbon corrosion is considered as the sole degradation source.

3.3.1 Liquid Water Transport in the Anode Channel

In literature, there are two common ways to track the two-phase water transport in the channel and GDL: the multi-phase mixture (M^2) [56] and two-fluid models [123]. In this chapter, the two-fluid approach is used to track the liquid volume fraction along the channel. Rather than calculating the gas phase velocity from the momentum equation, the total gas flux N_t can be readily converted to velocity, then an interfacial drag coefficient f(s)

Table 3.2 Physical, transport and kinetic properties

Quantity	Value	Ref.
Diffusive flux	$J_i = -\frac{P_{AN}}{RT\psi(n)} W \frac{dn_i}{dy}$	[100] (3.12)
Convective flux	$N_t(y) = N_t(L) - \int_y^L \Big[r_{H_2,rct}(\tilde{y}) + r_{H_2,crs}(\tilde{y}) + r_{N_2,crs}(\tilde{y}) + r_{V,crs}(\tilde{y}) + r_{V,rct}(\tilde{y}) + r_{V,cond}(\tilde{y}) + r_{O_2,crs}(\tilde{y}) + r_{O_2,rct}(\tilde{y}) + \frac{P_{AN}}{RT}\frac{\partial s}{\partial t} \Big] d\tilde{y}$	[68] (3.13)
Water condensation source term	$r_{V,cond} = max\left[0, K_{cond}\frac{(n_V P_{AN} - P_{sat})(1-s)}{RT}\right]$	(3.14)
Metal potential at cathode	$V_m^{CA} = V_m^{AN} + E_{cell} + R_{GDL} i_{AN}$	[68] (3.15)
Membrane potential at cathode	$\phi_{CA} = \phi_{AN} - R_{mem} i_{AN}$	[68] (3.16)
Cathode carbon corrosion	$i_{C,CA} = (1 - s_{ctl,ca})\varepsilon_C \gamma_C i_{0,C} L_C \frac{P_{V,CA}}{P^*_{V,CA}} \times \exp\left[\frac{\alpha_{a,C} F}{RT}(V_m^{CA} - \phi_{CA} - V_C^{eq})\right]$	[68] (3.17)
Effective factor	$\varepsilon_C(y,t) = \left[\frac{m_C(y,t)}{m_{C,0}}\right]^q$	[89] (3.18)

between liquid and gas phase velocities is used to obtain the liquid phase velocity [123].

Taking into account diffusion, convection and source term, the liquid water volume fraction along the channel is described by the following PDE:

$$\rho_w \frac{\partial s}{\partial t} = \rho_w D_s \frac{\partial^2 s}{\partial y^2} - \rho_w \frac{RT}{P_{AN}} \frac{\partial [f(s) N_t(y)]}{\partial y} + M_w \left(r_{V,cond} + \frac{N_{l,an}(x = \delta_{GDL})}{d_{ch}} \right) \tag{3.19}$$

where ρ_w is the density of water in Kg/m^3, M_w is the molar mass of water in Kg/mol, and

D_s is the liquid diffusivity in the channel in m^2/s. There are two contributions to the source term in Eq. 3.19: The first is local vapor condensation ($r_{V,cond}$) in the channel and the other is liquid water flux from the GDL to the channel. The latter, $N_{l,an}$, is zero when the GDL liquid front stays inside the GDL, i.e., not at the GDL/channel interface. Details of the GDL model can be found in [65].

The convective term $\rho_w \frac{RT}{P_{AN}} \frac{\partial[f(s)N_t(y)]}{\partial y}$ drives the liquid water towards the channel end. As the liquid droplets are carried by gas flow, the corresponding interfacial drag coefficient f(s) is assumed to be a linear function of liquid water volume fraction [123]:

$$f(s) = K_{slip} s \tag{3.20}$$

where K_{slip} is the physical velocity slip ratio between liquid and gas, which is a tunable parameter in the model. Eq. 3.20 completes the liquid PDE formulation, Eq. 3.19.

Due to the high stoichiometry ratio at the cathode, most of the liquid water could be removed by the air flow. Therefore the effect of cathode channel liquid is not included in the model for simplicity.

3.3.2 Purge Flow

The exact amount of gas leaving the channel at the purge event is critical to determine the fuel efficiency and voltage recovery. The volumetric flow rate at the outlet (channel end) is described by [124]:

$$W_{total} = A_o \left(C_{turb} \left[\frac{2}{\rho} \Delta p + \left(\frac{\nu R_t}{2 C_{turb} D_h} \right)^2 \right]^{0.5} - \nu \frac{R_t}{2 D_h} \right) \tag{3.21}$$

where C_{turb} = 0.61 is the dimensionless discharge coefficient under turbulence condition, D_h is the hydraulic diameter of the orifice, A_o is the area of the orifice (solenoid valve port), R_t=9.33 is the critical purge parameter from [124]. Also, ρ is the density of the mixture flow (liquid water and multiple gas species); ν, defined as μ/ρ, is the kinematic viscosity of the mixture flow, and Δp is the differential pressure across the orifice. Since the local species molar fraction varies with the channel length and thus purge time, integrating W over the purge interval gives the volumetric displacement of accumulated gas at the channel end. The total outlet flow is assumed to be evenly distributed between the parallel channels, therefore $W_{chan} = W_{total}/k$ where k is the number of parallel channels in the anode. The factor $1/k$ scales the total outlet flow for simulations are performed on a single channel.

Since the purge interval is very short (in a scale of ms), the profiles of molar fractions

(n_i) and flow rate (W_{chan}) at the end of a DEA cycle are assumed to move along the channel direction during the purge without the diffusion effects, which is a typical plug flow behavior.

The density ρ and viscosity ν at the outlet are dependent on the gas composition and liquid volume fraction. The density ρ can be defined by:

$$\rho(y) = (1-s)\rho_g + s\rho_w \tag{3.22}$$

$$\rho_g(y) = \rho_{N_2} n_{N_2} + \rho_V n_V + \rho_{O_2} n_{O_2} + \rho_{H_2}(1 - n_{N_2} - n_V - n_{O_2}) \tag{3.23}$$

in which ρ_w is the density of liquid water, and ρ_g is the density of gas mixture. The viscosity is defined similarly. Since the local gas composition varies along the channel, the density/viscosity of the gas mixture is a function of y.

3.4 Model Validation and Simulation Results

The above DEA oriented two-phase fuel cell model is tuned and validated with the experimental data. The details of the experiment are described in a prior publication [66]. The parameters relevant to the gas species distribution along the channel have been tuned against the GC sample data in our prior work [68]. Table 3.3 summarizes the parameter values used in the along-channel model. There are two steps in implementing the model: the coupled multi-state PDE system representing the DEA cycle is solved first, followed by the purge flow submodel which calculates the hydrogen loss and redistributes all states as the initial condition of the subsequent DEA cycle. This two-step implementation repeats for 100-1200 times depending on the cycle duration to simulate the cell lifetime. Finally, the efficiency is evaluated after finishing the simulation and collecting the data. The coupled PDE system is solved using a variable step solver, Matlab ODE15s, with a relative tolerance of $1e^{-4}$. The channel is discretized using a 2nd order approximation of the spatial derivatives on a 51 point grid.

The data set with high current load (0.6 A/cm^2) and high cathode RH (100%), which leads to sufficient liquid water accumulation in the anode, is selected for simulation. Fig. 3.4 compares the tuned model and experiment. The purge was triggered as the cell voltage reduced to 0.4 V in the experiment, hence the cycle duration varies from ~700 s to ~900 s. The cell voltage experienced an abrupt drop as the cathode stoichiometry ratio was reduced from 3 to 2.

Table 3.3 Geometrical, physical and operating parameters

Quantity	**Value**
Catalyst loading L_{Pt}	$3 \times 10^{-4}\ g\ cm^{-2}$
Electrochemical area of Pt γ_{Pt}	$6 \times 10^{5}\ cm^{2}\ g^{-1}$
Electrochemical area of carbon γ_C	$6 \times 10^{6}\ cm^{2}\ g^{-1}$
Anodic transfer coefficient for carbon corrosion $\alpha_{a,C}$	0.25
Exchange current density of oxygen reaction i_{0,O_2}	$6.1 \times 10^{-9} A\ cm^{-2}$
Exchange current density of carbon corrosion $i_{0,C}$	$2.5 \times 10^{-10} A\ cm^{-2}$
Equilibrium potential for carbon corrosion V_C^{eq}	0.21 V
Anode metal potential V_m^{AN}	0 V
Initial carbon loading per unit MEA area $m_{C,0}$	0.002 g cm^{-2}
Cathode reference pressure $P_{i,CA}^{*}$, i=[O_2,vapor]	1.2355×10^{5} Pa
Anode inlet pressure P_{AN}	4.0 psig
Cathode system pressure P_{CA}	3.6 psig
Cell temperature T	323 K
Hydrogen enthalpy of formation Δh_f	-242 $\times 10^{3}$ J/mol
Discharge coefficient C_{turb}	0.61
Critical value for purge flow model R_t	9.33
Area of purge orifice A_o	0.37 mm^2
Hydraulic diameter of purge orifice D_h	1.9 mm
Tunable power factor for remaining carbon, q	4.0
Effective MEA area A	50 cm^2
Number of anode channels k	25
Density of hydrogen ρ_{H_2}	0.0899 kg/m^3
Density of nitrogen ρ_{N_2}	1.25 kg/m^3
Density of vapor/liquid water ρ_V/ρ_w	0.0829/997 kg/m^3
Viscosity of hydrogen μ_{H_2}	100.1 $\times$ 10^{-6} m^2/s
Viscosity of nitrogen μ_{N_2}	14.2 $\times$ 10^{-6} m^2/s
Viscosity of vapor/liquid water μ_V/μ_w	144.8/0.553 $\times$ 10^{-6} m^2/s
Water transfer coefficient γ_w	5.7 $\times$ 10^{-6} m/s
Molar mass of water M_w	0.018 Kg/mol
Condensation rate constant K_{cond}	1000 1/s
Mass transport coefficient γ	0.1 m/s
Liquid water diffusivity D_s	1 m^2/s
Vapor diffusivity in anode GDL D_v	1.25$\times$ 10^{-4} m^2/s
Slip ratio between liquid and gas K_{slip}	0.6
Number of channel meshes in numerical computation N	51

The model predicted voltage evolution agrees with the experimental data. The liquid effects are captured by $s_{ctl,an}$, $s_{ctl,ca}$ and s. The predicted increasing liquid mass within a

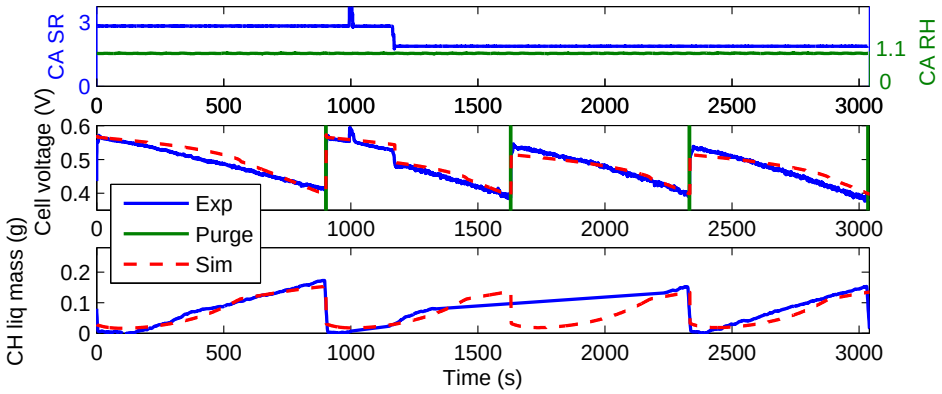

Figure 3.4 Comparison between tuned model and experiments at current density 0.6 A/cm^2, cell temperature 50 °C, anode/cathode pressure 4.0/3.6 psig, cathode stoichiometry ratio 3 and 2, and RH 100%.

cycle is consistent with the experimental data, as shown in the third subplot of Fig. 3.4. The liquid mass from the experiment did not drop at the end of the second cycle, probably due to the droplet plugging in the cell manifold.

Other simulation results are summarized in Fig. 3.5. The simulation starts with a fully humidified membrane ($\lambda_{mb} = 12$) to account for the operation history of the cell. It can be seen that the membrane water content remains at a high level during the whole period. Liquid saturation in the cathode catalyst layer is substantially higher than the anode in the channel inlet and middle regions, which drives the water transport from cathode to anode. The model predicts hydrogen starvation at the 0.9 fractional channel location at t=~770 s. Finally, the seventh subplot indicates that the liquid front stays at the GDL/channel interface only at the channel-end region. In other regions of the channel, liquid water comes from local condensation.

3.4.1 Predicting Carbon Corrosion and Cell Lifetime

The target of a fuel cell lifetime is ~5000 h in automotive applications to compete with the conventional powertrain, and voltage degradation rate of 2-10 μV h^{-1} is generally acceptable with flow-through operations [2]. In this chapter, therefore, we define the occurrence of a 10 mV irreversible voltage drop in DEA operation as the end of "life". The model can be used to predict the cell lifetime under continuous DEA cycling. The carbon loss is captured by Eq. 3.9, which affects the carbon corrosion rate and terminal voltage over time.

Figure 3.6 presents the lifetime simulation results, i.e., the remaining carbon at the channel-end region within 150 continuous DEA cycles, and the voltage and corrosion current evolutions in selected cycles. The cycle duration is 900 s and the purge interval is

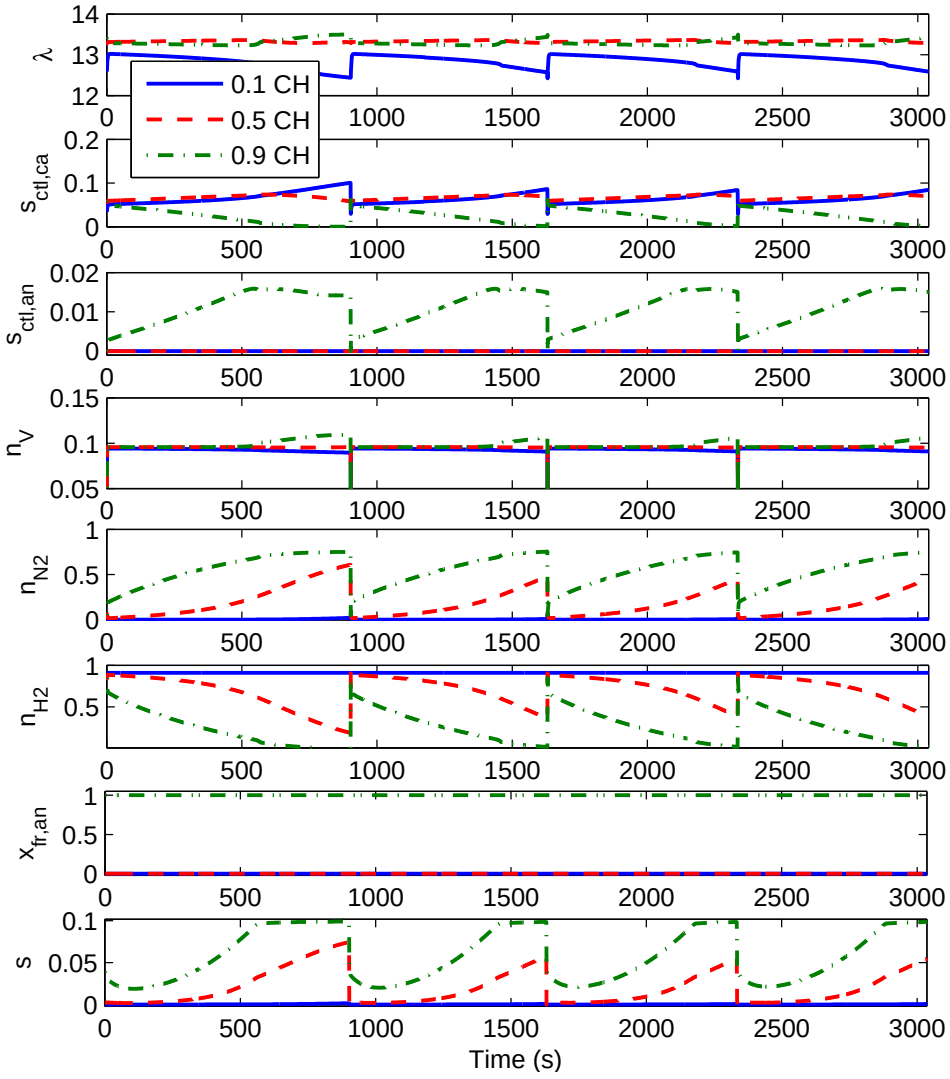

Figure 3.5 Simulation results from the same operating conditions as in Fig. 3.4 (cathode stoichiometry ratio is 3 except stated otherwise). Each subplot shows the evolutions of a specific parameter at the inlet, middle and end regions of the channel. These subplots present the simulation results of membrane water contents, liquid saturation in the cathode and anode catalyst layers, molar fractions of vapor, nitrogen and hydrogen, dimensionless liquid front in the anode GDL, and channel liquid volume fraction, respectively.

54 ms. The time-evolution of the terminal voltage and carbon corrosion current at three representative locations along the channel (inlet, middle and outlet) for the 5 selected DEA cycles are shown in the upper subplots of Fig. 3.6. The operating conditions are the same as the validated case in Fig. 3.4. The cell voltage at the 150th cycle exhibits ~10 mV irreversible voltage loss compared with the initial cycle, corresponding to ~25% carbon loss in the cathode catalyst layer at 0.9 fractional channel location near the end of the channel and ~11% total carbon loss overall. The remaining carbon at the channel end is illustrated

by the second subplot; the cathode carbon corrosion rate at the channel end is substantially higher than other regions due to the local fuel starvation.

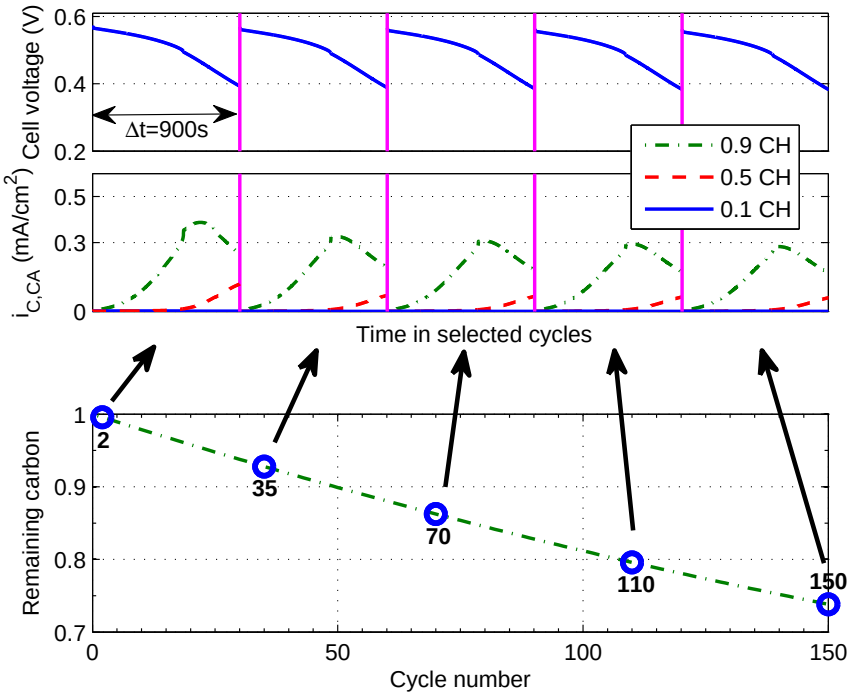

Figure 3.6 Simulation results of 150 continuous DEA cycles. The results from selected DEA cycles, rather than the entire data set, are examined in details as indicated by the arrows. The vertical pink lines represent the purge events. The cycle duration is 900 s and the purge interval is 54 ms. The operating conditions are consistent with the validated case in Fig. 3.4: current density 0.6 A/cm^2, cell temperature 50 °C, cathode stoichiometry ratio 3, and RH 100%. The first subplot shows the cell voltage. The second subplot illustrates the cathode carbon corrosion current in the inlet, middle and end regions of the channel. The third subplot presents the percentage remaining carbon in the cathode catalyst layer at 0.9 fractional channel location throughout the whole lifetime.

3.4.2 Predicting Voltage Degradation

Figure 3.7 illustrates the after-purge voltage degradation over multiple cycles for two cases with different cathode supply RH. The tuned parameters are $i_{0,C}$ and q. The experimental data in Fig. 3.7 come from our lifetime degradation tests for the DEA cell [25]. The details of the test protocol and experimental setup are not reported here, whereas a summary of the MEA specification is given. The MEA consists of two 400 μm thickness (before compression) carbon papers with micro porous layers (MPL, SIGRACET 10BC, SGL), and catalyst coated membrane (CCM, Ion Power) with 25 μm-thick membrane (Nafion,

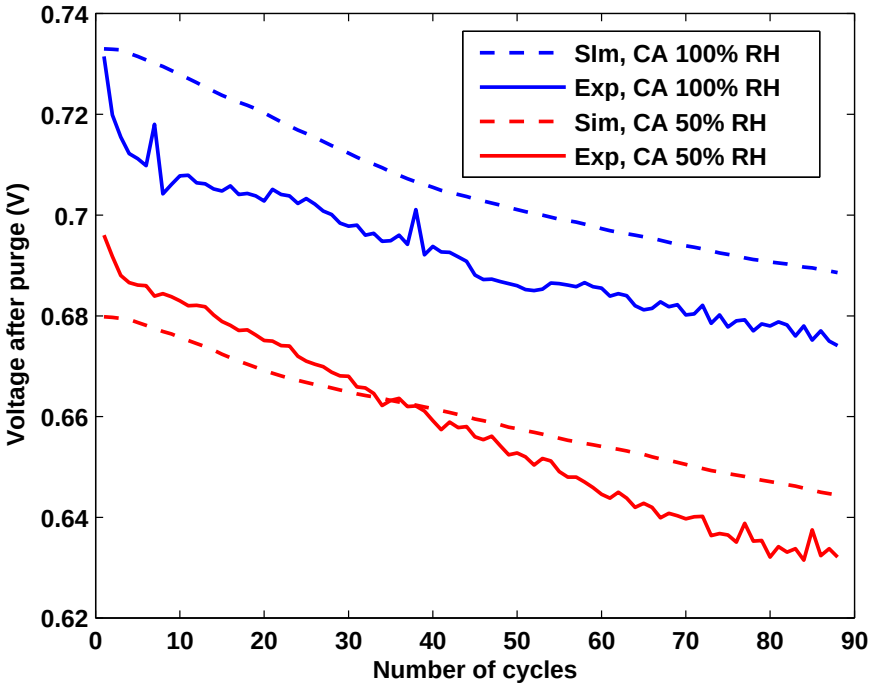

Figure 3.7 The comparison of after-purge voltage degradation from both experiment and simulation. The operating conditions are: cell temperature 60 °C, cathode SR 2.5, both anode and cathode pressures 3.8 psig, current density 0.4 A/cm^2, and cathode supply RH 50% and 100% for each case.

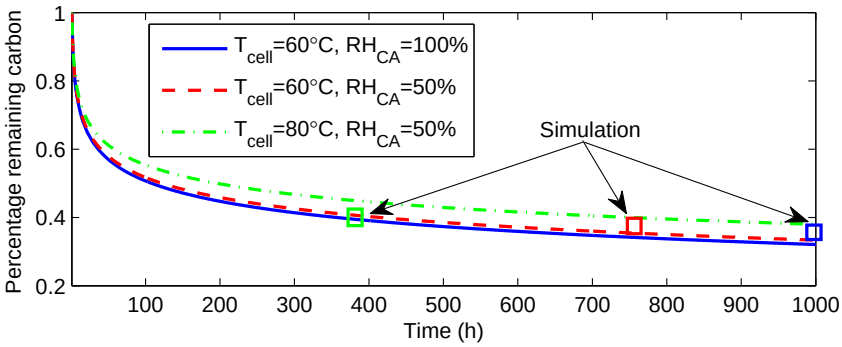

Figure 3.8 The percentage remaining carbon mass in the channel-end region. The operating conditions are: cathode SR 2.5, both anode and cathode pressures 3.8 psig, and current density 0.4 A/cm^2. The cathode supply RH is 100% for Case 1 (blue solid line) and 50% for Cases 2 (red dashed line) and 3 (green dash-dot line). The cell temperature is 60 °C for Cases 1 and 2 and 80°C for Case 3. The simulation results from postmortem thickness of cathode catalyst layer are illustrated by the colored markers corresponding to each case.

Dupont) and 0.3 mg cm^{-2} Pt loading at both anode and cathode. The Platinum/Carbon weight percentage (wt%) ratio was not released by the company.

When the cathode RH is 100% the voltage decreases primarily due to the well-predicted

carbon corrosion. When the cathode RH is 50% the model under-estimates the decay. It is likely that the membrane degradation, which is not considered in the model, also contributes to the voltage degradation in a form of polymer chemical decomposition and associated increased resistance; because the chemical degradation proceeds more rapidly when the cathode is drier (RH 50%) [41]. Since shorting and hydrogen crossover measurements were not performed at the periodic evaluations, the exact cause for such discrepancy is unclear. Fortunately, catastrophic membrane failure such pin-hole was not observed in the DEA operation with small or medium current load [39] which normally leads to rapid voltage drop and shutdown of the cell under galvanostatic operation [103].

The percentage remaining carbon mass at the channel end (0.9 fractional channel) throughout the degradation test is calculated from both simulation and experiments as shown in Fig. 3.8. The postmortem MEA samples were analyzed to determine the thickness of cathode catalyst layer [25]. Assuming constant density of the cathode catalyst layer throughout the test, the decreasing thickness can be attributed to the loss of carbon mass. The simulation results show general consistency with the experimental data for all three cases.

3.5 Optimization of Purge Schedule

The target range for the purge interval depends on the gas and liquid water distribution in the anode channel at the end of the cycle. Figure 3.9 shows a simulation used to determine the target range for the purge interval. At the end of a DEA cycle or the start of a purge ($t=t_{bp}$), liquid water accumulates in the channel end, where complete hydrogen starvation with zero molar fraction is also observed.

3.5.1 Determining the Target Range for Purge Interval

The minimum purge time, δt_1, is designed to release the accumulated water/nitrogen and to place the hydrogen starvation front at the channel end. Due to the high purge flow rate (diffusion can be ignored), the profile at $t=t_{bp}+\delta t_1$ consists of a shift of the hydrogen profile at $t=t_{bp}$ towards the channel end plus a hydrogen restored region ($n_{H_2}=1$) in the channel inlet. In other words, the purge flow behaves as plug flow. With the minimum purge interval δt_1, there is no hydrogen loss during the purge, however the hydrogen concentration is low in the channel, which would adversely affect the energy output in the subsequent cycle. If the purge is extended to $t=t_{bp}+\delta t_2$ when the hydrogen molar fraction reaches unity in

the whole channel, then the energy output in the subsequent cycle would be the highest, although there is some hydrogen loss during the purge.

Mathematically, δt_1 and δt_2 satisfy:

$$L - \int_{t_{bp}}^{t_{bp}+\delta t_1} \frac{W_{total}}{k w_{ch} d_{ch}} dt = y|_{n_{H_2}=0, t=t_0} \tag{3.24}$$

$$L - \int_{t_{bp}}^{t_{bp}+\delta t_2} \frac{W_{total}}{k w_{ch} d_{ch}} dt = 0 \tag{3.25}$$

in which W_{total} is the volumetric purge flow rate defined in Eq. 3.21.

In Fig. 3.9 the hydrogen starvation occurs before the purge. There exists a special scenario: when the cycle duration is very short, then it is possible that hydrogen starvation does not occur even at the channel end. Under that circumstance, there would inevitably be a certain amount of hydrogen loss during any purge. Therefore the lower limit of the target

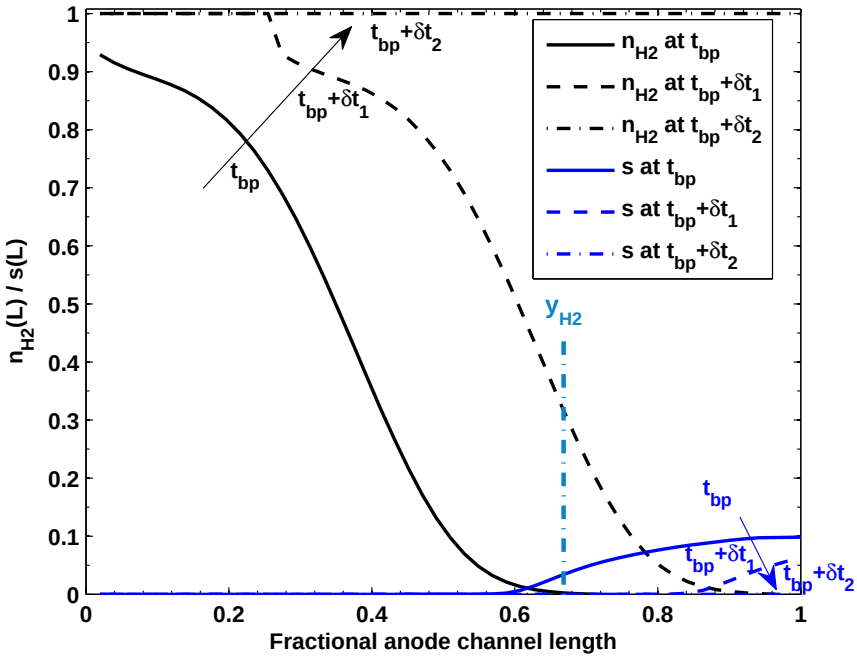

Figure 3.9 Distribution of hydrogen concentration and liquid volume fraction before and after purge at operating conditions of cycle duration 1100 s, current density 0.6 A cm^{-2}, cell temperature 50 °C, cathode RH 0.9, stoichiometry ratio 3 and pressure 1.18 bar. The black curves show the hydrogen molar fraction and the blue ones show the liquid volume fraction in the anode channel. The hydrogen starvation front y_{H_2} before the purge is also shown. Minimum purge interval should be chosen to place the hydrogen starvation front at the channel end, and maximum one exactly and fully restore the hydrogen in the channel without further loss.

range for small cycle duration is always t_{SV}. The target range for purge interval in general is dependent on the cycle duration.

3.5.2 Influences of Cycle Duration

In this subsection we investigate the influence of cycle duration on carbon corrosion and cell efficiency. The purge interval is set to a constant, δt=20 ms. The cycle duration affects both the cathode carbon corrosion rate within a cycle and the hydrogen loss during the purge.

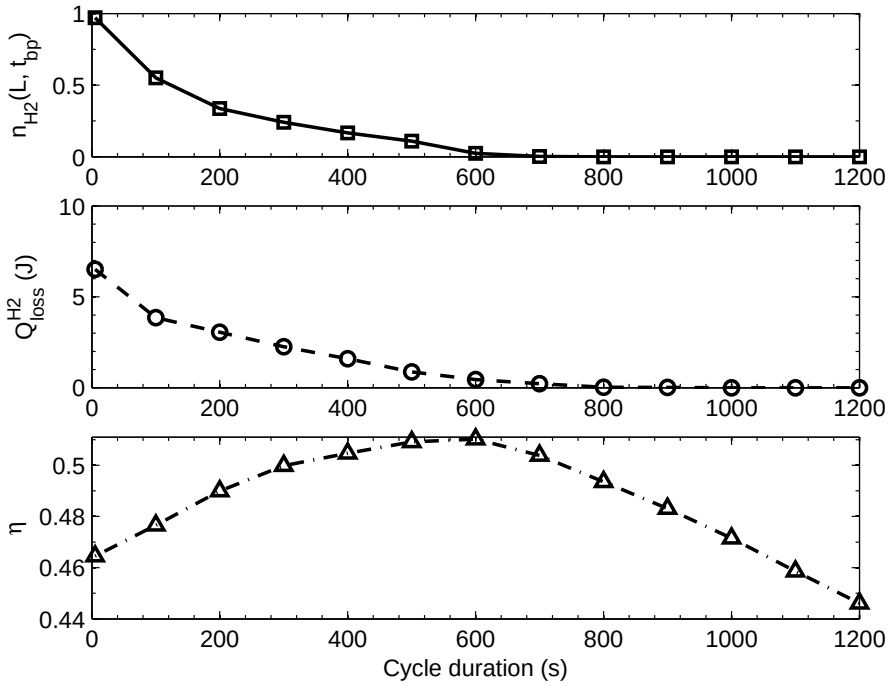

Figure 3.10 Influences of cycle duration. The operating conditions are consistent with the validated case in Fig. 3.4. The first subplot indicate the influence of increasing cycle duration on the hydrogen molar fraction at the channel end right before the purge. The second subplot shows the hydrogen loss in Joule. The third subplot indicates the efficiencies evaluated over one DEA cycle together with the subsequent purge. The purge interval is fixed at 20 ms.

The DEA cell efficiency as the objective should also be considered when determining the optimum cycle duration. Fig. 3.10 shows the channel end hydrogen concentration at the cycle end and the hydrogen loss during the purge as a function of cycle duration with a fixed purge interval. When the cycle duration becomes shorter, there is still hydrogen at the channel end right before the purge, and thus unavoidable hydrogen loss. Wasted hydrogen during the purge reduces the DEA cell efficiency through $Q_{loss}^{H_2}$ term in Eq. 3.1. The hydrogen loss is substantially reduced as the cycle duration extends beyond 600 s, be-

cause hydrogen starvation occurs at the channel-end region with extended cycle duration and therefore the purge removes less hydrogen and more nitrogen and liquid water. The thermodynamic efficiency increases with shorter cycle duration as indicated by the terminal voltage as shown in Fig. 3.11. However $Q_{loss}^{H_2}$ also increases with shorter cycle duration. The efficiency in the third subplot of Fig. 3.10 shows a non-monotonic evolution against cycle duration. The hydrogen loss is dominant due to the increasing efficiency when the cycle duration is smaller than 600 s.

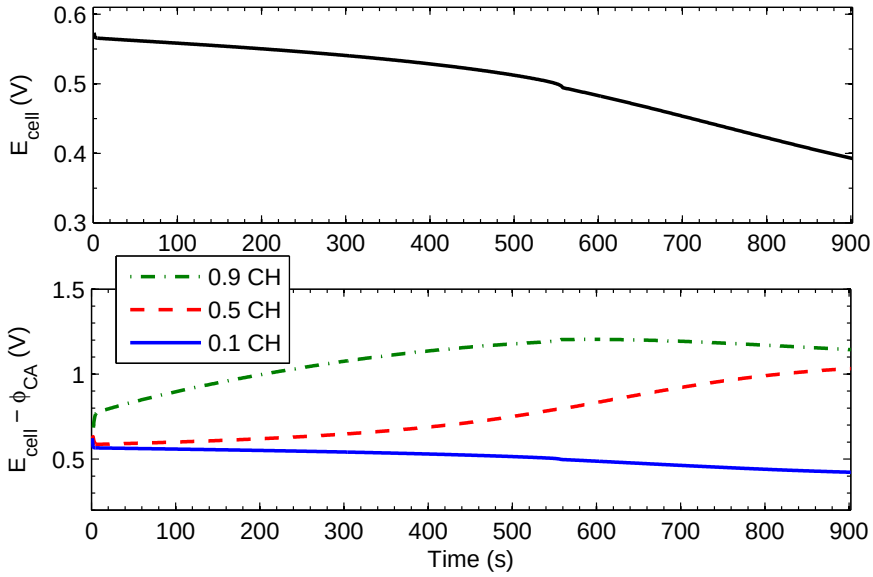

Figure 3.11 Evolution of cathode interfacial potential within a DEA cycle. The operating conditions are consistent with the validated case in Fig. 3.4. The upper subplot shows the model predicted cell voltage within a 900 s cycle. The lower subplot illustrates the cathode interfacial potential at the inlet (0.1), middle (0.5) and end (0.9) regions of the channel. At the end region a non-monotonic evolution trend with time has been observed.

Figure 3.11 illustrates the evolution of cell voltage and cathode interfacial potential within a DEA cycle. The cycle duration is 900 s and the operating conditions are the same with the validated case in Fig. 3.4. The cathode interfacial potential, $E_{cell} - \phi_{CA}$, determines the kinetics of cathode carbon corrosion as shown in Eq. 3.17. It is much higher at the channel end compared with other regions due to the fuel starvation. The cathode interfacial potential at the channel end is therefore the main concern. As shown in the upper subplot, the cell voltage decreases with time due to the hydrogen depletion which effectively reduces the corrosion rate. Meanwhile the membrane phase potential at the channel end becomes more negative, which increases the corrosion rate. If the cycle duration is extended, the carbon corrosion rate at the channel end would decrease after reaching a peak value at ~650 s. That is to say, further postponing a purge after reaching the peak cathode

interfacial potential would be beneficial for protecting carbon, although the cell voltage decreases significantly. If there are no other constraints on cycle duration, a shorter cycle is preferred because of the increased energy output and reduced carbon corrosion during DEA cycling.

3.5.3 Influences of Purge Interval

In this subsection, the influences of purge interval are examined with fixed cycle duration. The model can be used to evaluate the trade-off between hydrogen loss and increased energy output for a single cycle. The objective function thus becomes $\eta = \frac{\int_{t_{ap}^{j}}^{t_{ap}^{j+1}} E_{cell} i A dt}{\Delta h_f (Q_{rxt}^{H_2} + Q_{loss}^{H_2})}$. The effect of carbon corrosion is not shown because it affects the integral in the numerator only after multiple cycles. Fig. 3.12 summarizes the simulation results. Three cases with different cycle durations are examined. The target range of purge interval depends on the cycle duration. In Fig. 3.12, the range of purge interval presented corresponds to the target range of that particular cycle duration (500 s, 800 s and 1100 s).

The hydrogen molar fraction at the channel end increases with purge interval and reaches unity at δt_2 as shown in the first subplot of Fig. 3.12. The second subplot indicates that an extended purge indeed leads to a larger power output since the hydrogen concentration is higher during the subsequent DEA cycle. On the other hand, it would produce a larger amount of hydrogen loss, as shown in the third subplot. The competing influence of hydrogen loss and increased terminal voltage on the overall efficiency as a function of purge interval is shown in the last subplot of Fig. 3.12. For the cases with Δt=500 and 800s, increasing purge interval leads to lower cell efficiency. However for longer cycle durations, when hydrogen starvation occurs in the channel end, the slope of the efficiency vs purge interval is non-monotonic. Therefore, the shortest duration does not yield the highest efficiency. In this case a maximum efficiency of 52.9% is reached, after which the efficiency slightly decreases. These findings indicate that if complete hydrogen starvation has not been observed in the channel end, reducing the hydrogen loss is more significant than restoring the hydrogen concentration in the anode. Even with complete hydrogen starvation (Δt=1100), δt=36 ms, rather than δt_2=42.1 ms, gives the largest efficiency.

The calculated efficiencies do not show substantial differences ($< 2\%$), because the purge interval is already constrained in the target range. This suggests that as long as the purge interval lies within the target range, then its influences on the efficiency may be negligible.

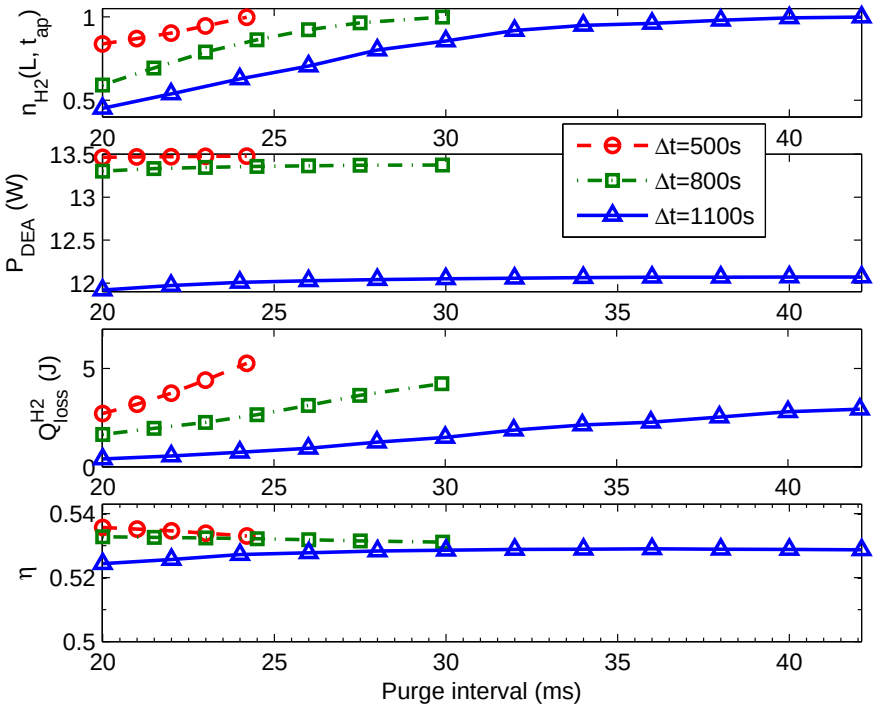

Figure 3.12 The influences of purge interval and cycle duration, with operating conditions being: current density 0.4 A cm^{-2}, cell temperature 50 °C, cathode RH 0.9, stoichiometry ratio 3 and pressure 1.18 bar. The simulation results are collected after the system reaches periodic steady state. The three colored curves with markers represent the simulation results obtained from three different cycle durations. The x-limits of each curve indicate δt_{min} and δt_{max} for that cycle duration. The first subplot shows the hydrogen molar fraction at the channel end after the purge. The second subplot presents the power outputs in the subsequent cycle after the purge. The third subplot indicates the hydrogen loss during the purge with different purge intervals. Finally, the fourth subplot shows the efficiencies evaluated over one DEA cycle together with different purge intervals.

3.5.4 Optimization of Cycle Duration and Purge Interval over Cell Lifetime

In prior subsections we examined the influences of cycle duration on carbon corrosion and purge interval on DEA cell efficiency. In general, shorter cycle duration and longer purge interval are beneficial for achieving higher thermodynamic efficiency and protecting support carbon in the cathode; however, the hydrogen loss would be higher in this case. The subject of this optimization study is to investigate the trade-off between wasted hydrogen and reducing the corrosion rate over a longer time horizon. The efficiency of a DEA cell, calculated using Eq. 3.1, is evaluated over the whole lifetime. In this work the cell lifetime is defined by the occurrence of 10 mV irreversible voltage drop. Since the cycle duration and purge interval both affect the lifetime, we use the shortest lifetime among all cases as the simulation time interval for comparing the efficiencies. In this subsection we con-

sider cycle duration and purge interval simultaneously as the variables and search for the maximum (optimum) lifetime efficiency, Eq. 3.1, within a 2-D space by simulating the efficiency over the cell lifetime. The operating conditions are the same with the validated case: current density 0.6 A cm^{-2}, cell temperature 50 °C, cathode RH 100% and stoichiometry ratio 3, and anode/cathode pressure 4.0/3.6 psig. The lifetime simulation was performed in Matlab environment at the University of Michigan Computer Aided Engineering Network (CAEN) PCs with 3.07 GHz Intel® Xeon® processor and 5.11 GB RAM. Matlab solver ODE15s was used for the non-linear system consisting of 12 dynamic states, and a grid number of 51 was used for along-channel spatial discretization. For a given operating scheme, the lifetime simulation consisting of multiple DEA cycles took more than 8 hours to finish. Those schemes with shorter cycle duration require larger number of cycles to reach the lifetime, and therefore consumed longer simulation time; because the transition between the DEA operation and purging is most time-consuming.

Fig. 3.13 illustrates the 2-D target domain in which the optima lies, as well as the calculated efficiencies within the domain. The target range for purge interval is calculated after the system reaches periodic steady state. The calculated target range for each purge interval, [max(t_{SV}, δt_{min}), max(t_{SV}, δt_{max})], is reflected by the vertical limits of the domain. The target range for cycle duration is defined as follows: its lower limit can go as small as zero, in which case it becomes a flow-through operation. Its upper limit is defined as the amount of time to reduce the cell voltage to 0.4 V. In Fig. 3.13, these two limits are 0 and 900 s, respectively. When cycle duration is extremely short (Δt=50 s and zero), the target range for purge interval shrinks to a single point, t_{SV}, because the very high hydrogen concentration in the channel leads to a large purge flow rate. When the cycle duration is less than 600 s, t_{SV} is always the lower limit of the target range.

Since the efficiency (Eq. 3.1) depends on the two design variables, Δt and δt, the search of optima is performed by scanning the target domain with coarse grids first. A further scan with finer grids would be performed as necessary until the optima can be located with satisfactory accuracy. The two-step scheme in scanning the domain can reduce the computational expense as the lifetime simulation is highly time-consuming. In Fig. 3.13, the grid distance for purge interval is 2 ms and for cycle duration 100 s.

At each grid represented by a combination of Δt and δt, the efficiency is collected to generate the contour plot. Because the cell durability is concerned, the total DEA operating time should be identical when evaluating the efficiency at each grid. The operating time is determined from the cell lifetime using the operating schedule that gives the worst durability, namely, longest cycle duration with shortest purge interval. In Fig. 3.13, they are 900 s and 34.1 ms, respectively. For this operating schedule, after 132 DEA cycles the

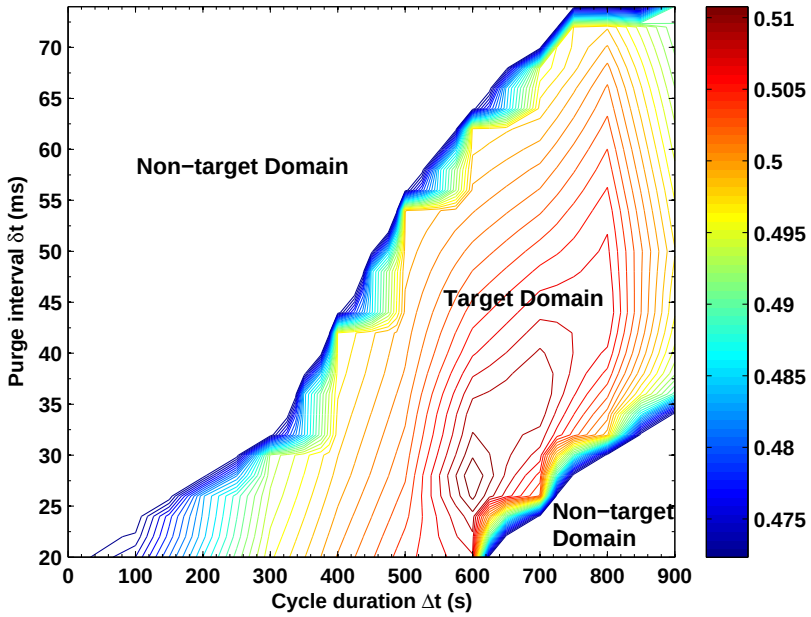

Figure 3.13 The contour plot showing the target domain and the lifetime efficiencies therein given fixed amount of operating time. The last subplots in Figs. 3.10 and 3.12 can be considered as the vertical and horizontal slices from the contour map, although only one cycle is evaluated as opposed to lifetime. The contour map shows that the maximum efficiency is achieved with cycle duration of 600 s and purge interval of 28 ms.

cell voltage observes 10 mV irreversible drop, and the cell lifetime is reached according to the prior definition. The total operating time is thus 132×900s=33h. The necessary DEA cycle numbers for other operating schedules are then calculated to satisfy an identical operating time. For shorter cycle durations or longer purge intervals, the actual voltage degradations at the end are smaller than 10 mV as shown in Fig. 3.14, which also plots the energy outputs throughout the total operating time for different cycle durations. Shorter cycle duration leads to higher energy or power output, and smaller voltage degradation, although the efficiency may be low with a short cycle duration. The difference in energy output is enlarged by the more severe cell degradation at longer cycle duration.

The optimum efficiency is ~50.9%, as shown in the contour plot in Fig. 3.13. The variation of efficiency within the target domain is less than 4%. Motivated by this finding, we conducted a parametric study of current setpoint on the target domain as shown in Fig. 3.15. At reduced current setpoint (power level), it takes a longer time to reduce the voltage to 0.4 V and there is a smaller amount of liquid water at the end of a cycle. As a result, with decreasing current density the target range for cycle duration becomes larger, whereas that for purge interval becomes smaller. One can simply calculate the target domain for the

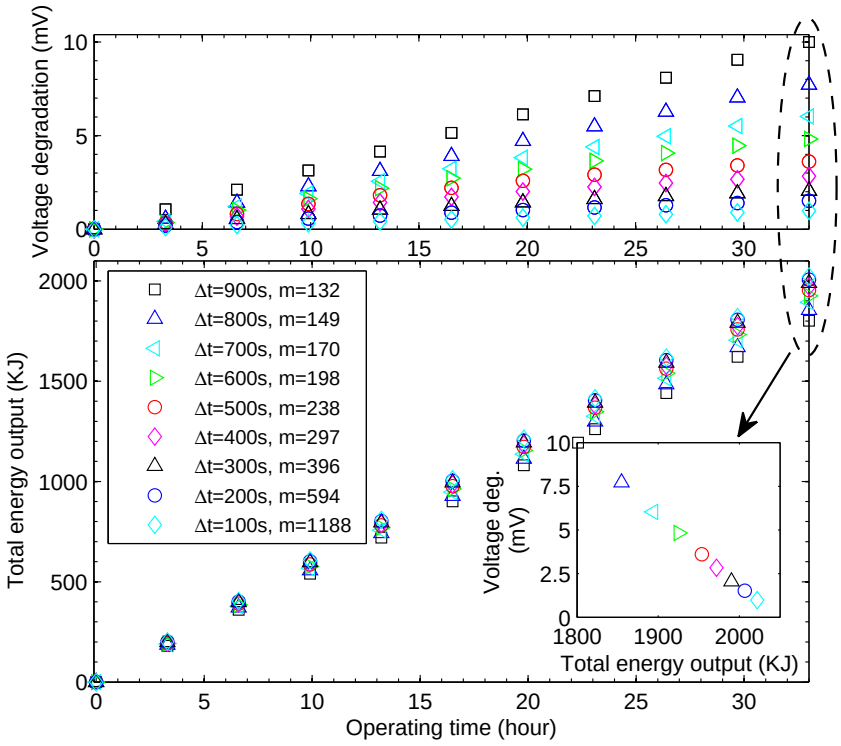

Figure 3.14 Voltage degradation and total energy output in 33 h DEA operation for different cycle durations with minimum purge intervals in the target domain. The cycle duration (Δt) and the corresponding number of cycles (m) are noted in the legend. With the same simulation time, the enlarged view shows the voltage degradation versus total energy output at the end for nine different cycle durations.

selected power as illustrated in Fig. 3.15, then use $0.5\times(\delta t_1+\delta t_2)$ as the optimized purge interval. The maximum achievable efficiency shown in Fig. 3.15, which increases with decreasing current loads, can be used as a criterion for choosing an operating condition, since the efficiency variation within the target domain is small.

In Fig. 3.13, increasing cycle duration beyond 800 s or decreasing cycle duration within 500 s decreases the efficiency. With a medium cycle duration (Δt=600 s) the achievable efficiency is highest. For purge interval, if the cycle duration is longer than 800 s, the efficiency reaches maximum at medium δt, whereas it decreases as it approaches δt_1 and δt_2. Complete hydrogen starvation due to water accumulation and nitrogen blanketing, which is associated with longer cycle durations, greatly accelerates the carbon corrosion in the channel-end region. When the cycle duration is very long (Δt>800 s), a medium purge interval, rather than complete purge, leads to the maximum efficiency. The efficiency still decreases beyond the maximum value with increasing purge intervals, which suggests that hydrogen loss is more influential than carbon corrosion under such conditions. When

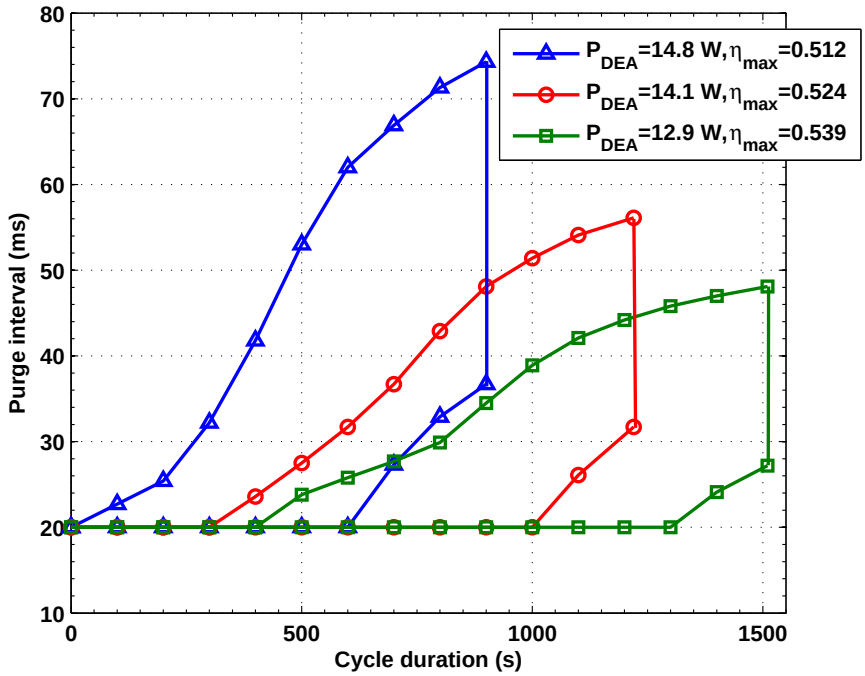

Figure 3.15 The target domains with different current setpoints (0.6, 0.5 and 0.4 A/cm^2) or power levels (14.8, 14.1 and 12.9 W). Other operating conditions (cell temperature 50 °C, cathode RH 100% and stoichiometry ratio 3, and anode/cathode pressure 4.0/3.6 psig) are the same for three cases. The power in the legend is the average one calculated from P_{DEA} for all cycle durations and purge intervals within the target domain.

$\Delta t < 500$ s, the efficiency decreases monotonically with increasing purge intervals and the minimum purge interval is preferred, because hydrogen loss becomes the sole concern.

The optimum appears at medium cycle duration. Because large Δt results in severe hydrogen starvation and associated carbon corrosion, whereas small Δt leads to substantial hydrogen in the channel-end region before the purge and associated hydrogen loss during the purge. It is essential not to purge the cell too early with sufficient hydrogen in the channel end. The DEA operation with small Δt generally exhibits a lower efficiency but produces higher energy output as shown in the lower subplot of Fig. 3.14.

3.6 Conclusions

In this chapter, we focus on the optimization of the DEA operating schedule determined by purge interval and cycle duration. We extended the along-channel, single-phase and transient DEA model in Chapter 2 to capture the liquid water transport and accumulation in

the anode channel end, as well as the purge flow behavior. These improvements were necessary to accurately predict water and nitrogen accumulation in the anode channel and the resulting hydrogen loss during the purge. The target ranges for purge interval are defined based on the channel gas composition at the end of the cycle duration.

We then investigated the influence of cycle duration and purge interval on carbon corrosion and DEA cell efficiency. There exists a trade-off between maximizing the thermodynamic efficiency during the DEA cycle and minimizing hydrogen loss during the purge. Shorter cycle durations and longer purge intervals tend to increase the thermodynamic efficiency; however, longer cycle durations and shorter purge intervals can reduce the amount of hydrogen loss. The optimization is performed by collecting the lifetime simulation data at each grid within the 2D target domain for cycle duration and purge interval. It is found that a medium cycle duration without severe hydrogen starvation at the channel end together with a short purge interval leads to the best DEA cell efficiency at current density of 0.6 A/cm^2. For long cycle durations, severe hydrogen starvation due to water accumulation and nitrogen blanketing accelerates the carbon corrosion particularly in the channel-end region, which requires an increased purge interval, but not a complete purge, to achieve highest efficiency. For short cycle durations, however, the minimum purge interval is preferred, suggesting that reducing hydrogen loss is more important than removing nitrogen and water. The small variation of efficiency (~4%) within the target domain suggests that as long as the purge interval can be selected from the target range, further optimization may not be necessary. Decreasing the current setpoint from 0.6 to 0.4 A/cm^2 changes the target domain, and increases the maximum obtainable efficiency.

The analysis and methodology presented in this chapter can be used for the design of a DEA fuel cell system. The optimum purge interval and cycle duration vary with the operating conditions and the physical specifications of solenoid valve. In the future, the optimized purge behavior and associated voltage degradation will be compared to experimental data.

Chapter 4

Equilibrium behavior in dead-ended anode operation of a fuel cell

The prior chapter showed that the DEA fuel cell system can be optimized for best lifetime efficiency. It is of further interest to investigate the possibility of operating the DEA fuel cell in a simpler way with the purge disabled, so that the purge optimization becomes unnecessary. To this end, this chapter investigates the nitrogen blanketing front during the DEA operation of a PEM fuel cell. It is found that the dynamic evolution of nitrogen accumulation in the DEA of a PEM fuel cell eventually achieves a steady state, which suggests the existence of equilibrium. We use a multi-component model of the two-phase, one-dimensional (along-channel) system to analyze this phenomenon. Specifically, the model is first verified with experimental observations, then utilized to show the evolution toward equilibrium. The full-order model is reduced to a second-order partial differential equation (PDE) with one state, which can be used to predict and analyze the observed steady-state DEA behavior. The parametric study is performed focusing on the influence of the cathode pressure on the existence of equilibrium in the DEA condition. In applications with low power requirement, operating a DEA cell without purging yields a simple system that does not require purge optimization but suffers serious degradation in the regions of hydrogen starvation. Novel cell design is necessary to alleviate the degradation.

4.1 Introduction

Dead-end anode (DEA) operation of a PEM fuel cell has been implemented by several groups [125, 126, 67] and applied in a commercial fuel cell module, the Nexa (1.2 KW stack of 42 cells) from Ballard Power Systems [127]. In DEA operation, hydrogen is fed into the anode with regulated pressure at the inlet, whereas the cathode is operated with conventional flow-through conditions associated with a stoichiometry ratio (SR) greater than one. Since the Nafion membrane is not an ideal separator, nitrogen and water can

diffuse through the membrane from the cathode and accumulate in the anode. In a vertically oriented channel as shown in Fig. 4.1, the reaction drives the convective transport of gas mixture toward the channel end. The accumulation of inert nitrogen at the channel end displaces hydrogen and eventually leads to a starvation at the channel end. The spatial variation of the species in the anode results in uneven local current distribution. The depletion of hydrogen over time leads to the decreasing cell voltage under galvanostatic operation. For example, in our 50 cm^2 DEA cell experiment, the voltage dropped from 0.7 to 0.6 V in about 15 minutes at a constant current load of 0.4 A/cm^2, as shown in Fig. 3.1.

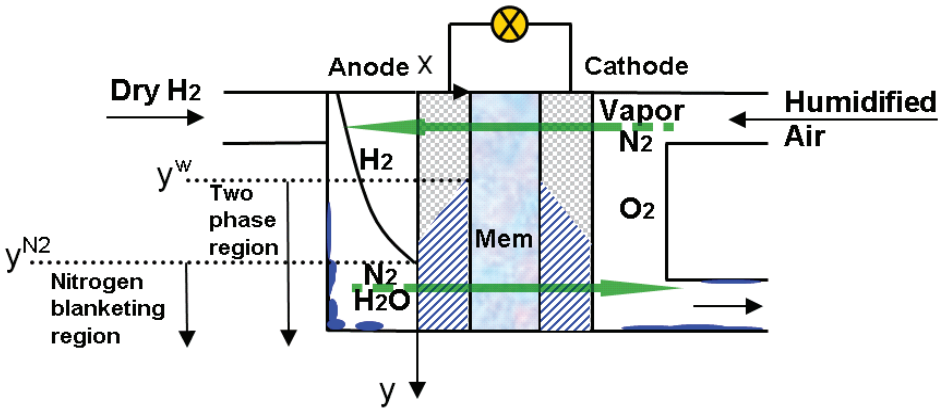

Figure 4.1 Equilibrium scenario in DEA operation (not to scale). The flux of nitrogen is from anode to cathode in the channel-end region, as opposed to in the other regions. Globally, zero net fluxes of nitrogen and water through the membrane are achieved at equilibrium.

Purging of the anode is typically needed to release accumulated nitrogen and water and maintain a manageable voltage range. A purge, normally taking 20-900 ms, is implemented via a solenoid valve at the downstream of the anode. Since the anode pressure is regulated at the upstream of anode, the opening of the solenoid valve leads to turbulent orifice flow, which clears the nitrogen and water from the anode channels. The downstream purge valve and the upstream pressure regulator are the only hardware at the anode side for a DEA system. As a comparison, the conventional flow-through anode (FTA) fuel cell system depends on a recirculation loop to maintain a high hydrogen utilization, which requires hydrogen grade plumbing and hardware such as ejector/blower and water separator. These components add weight, volume, and expense to the system.

Motivated by the experimental findings of [115], the possibility of operating the DEA cell without purging is analyzed in this paper. We address the conditions under which system equilibrium could be achieved with relatively stable voltage output under galvanostatic operation, and how to obtain a reasonable power under such equilibrium conditions. Voltage equilibrium was indeed observed in prior experimental studies [122, 128]. These findings motivate our further investigation by mechanism analysis and simulation using the

validated model.

As shown in Fig. 4.1, a stratified channel distribution with water and nitrogen in the end can be observed for the DEA cell [67]. In this case the local nitrogen partial pressure may easily exceed the cathode, particularly in the channel-end region. The nitrogen diffuses from the anode to the cathode due to the partial pressure gradient, as illustrated by the bottom arrow (positive x-direction). In the upper portion of the cell, the nitrogen crossover is from cathode to anode (negative x-direction). The nitrogen continues to accumulate in the anode until a global balance of nitrogen crossover has been achieved, meaning a zero net flux of nitrogen. The nitrogen partial pressure in the anode depends on the rate of crossover and the convective velocity, which are coupled with the current density distribution. An equilibrium for the nitrogen blanketing front is necessary for the equilibrium of the whole DEA fuel cell system. There is a non-linear coupling of anode nitrogen partial pressure and membrane hydration that introduces further complexity while analyzing such equilibrium. The local electrochemical reaction rate depends on the hydrogen concentration, or nitrogen concentration due to the regulated anode pressure, and determines the local water generation rate, which affects the membrane water content. The membrane permeation coefficient for nitrogen, as a function of membrane water content and temperature, in turn influences the local nitrogen crossover rate and the establishment of nitrogen equilibrium.

In previous work [23], the effect of nitrogen accumulation in the anode on the voltage decay has been demonstrated by modeling nitrogen crossover and convective transport. However, the model neglected the impact of diffusion in the anode channel, which can be significant for the deeper channel geometry studied here. A one-dimensional, single-phase, and transient model considering both convection and diffusion has been developed [66] to capture the spatiotemporal evolution of species and electrochemical reaction in a DEA cell. The model was further extended to include the cathode carbon corrosion caused by the anode fuel starvation and associated irreversible voltage degradation over time [68]. Recently, the model was improved to be 1+1D (along channel + through membrane) and two-phase so that the purge behavior can be predicted more accurately for an optimization study of purge scheduling [69]. After careful tuning, the present full-order model can capture comprehensive mass transport and electrochemical processes in DEA operation with satisfactory accuracy. The model can be used for predicting the equilibrium behavior [122]. However, the full-order model requires numerical tools with substantial computational expense to investigate the equilibrium.

Therefore, we focus on reducing the number of model states. It is anticipated that the reduced-order model can still predict the equilibrium behavior and characteristics. Similar publications (simulation and analysis) focus on the fuel cell equilibrium from Benziger's

group [129, 72, 71, 130]. However, those studies are based on a stirred-tank-reactor (STR) fuel cell. In such a case both anode and cathode supplies are dry or slightly humidified to comply with the auto-catalytic concept of the STR fuel cell, and the equilibrium arises from a water balance. The effect of convective transport is eliminated by the open channel architecture. Although both the STR and DEA cells feature self-humidification and spatial inhomogeneity, the equilibrium behavior in the DEA cell represents a more complicated scenario where both diffusion and convection must be considered. The convection leads to the stratified channel distribution of gas species in the vertically oriented cell. The diffusive transport in the channel is equally important by moderating the effect of nitrogen blanketing in the anode channel.

This chapter is organized as follows. Since the model has been detailed in prior chapters, only a brief overview is provided in this chapter. The model validation against the flow-through polarization will be presented. The tuned model predicts the voltage evolution toward equilibrium in DEA operation, achieving satisfactory agreement with the experimental data. A single-state PDE system based on the nitrogen distribution in the anode is derived. This reduced order model is shown to predict the evolution toward equilibrium and capture the influence of cathode pressure. Finally, the voltage degradation under equilibrium operation is identified.

4.2 Model Summary and Validation

The baseline (full-order) model is 1+1D, two-phase, and transient, which generally captures all transport phenomena and reaction kinetics in the vertically oriented DEA cell.

The model parameters relevant to the species distribution in the anode have been tuned in prior works [66, 68]. These parameters include the nitrogen permeation scale factor, the oxygen crossover scale factor, and the hydrogen concentration parameter [66, 68]. They are kept unchanged in this paper. Another group of parameters that relate to the cell polarization are further tuned: the exchange current density of oxygen reaction (i_{0,O_2}) and the contact resistance (R_{GDL}). These two parameters influence the reaction kinetics and cell voltage by the Butler-Volmer equation, as shown in Eqs. 4.1 and 4.2 with detailed discussions in Ref. [68]. The average current density is related to the local current density by Eq. 4.3.

$$i(y,t) = i_{0,O_2}\left\{\frac{P_{V,CA}}{P^*_{V,CA}}\exp\left[\frac{\alpha_{a,O_2}F}{RT}(\eta^{CA})\right] - \left(\frac{P^{CL}_{O_2,CA}}{P^*_{O_2,CA}}\right)^{\beta_{O_2}}\left(\frac{P_{H_2}}{P^*_{H_2}}\right)^{\beta_{H_2}}\exp\left[\frac{-\alpha_{c,O_2}F}{RT}(\eta^{CA})\right]\right\} \tag{4.1}$$

$$\eta^{CA} = V^{CA}_m - \phi_{CA} - V^{eq}_{O_2} = V^{AN}_m + E_{cell} + R_{GDL}i_{AN} - \phi_{CA} - V^{eq}_{O_2} \tag{4.2}$$

$$i_{fc} = \frac{1}{L_{ch}}\int_0^{L_{ch}} i(y,t)dy \tag{4.3}$$

Table 4.1 Tuned parameters in the model

Quantity	Value	Range
i_{0,O_2}	0.8×10^{-9} A/cm^2	10^{-10}–10^{-8} A/cm^2
R_{GDL}	0.34 Ω cm^2	0.1–0.8 Ω cm^2

Figure 4.2 shows the polarization performance obtained from the flow-through operation, and Figure 3.7 illustrates the voltage evolution in three continuous DEA cycles for two cases with different cathode supply RH. The DEA model is used to predict flow-through operation by assigning a constant to the flux at the anode outlet N_{out} [69] so that the desired anode SR is achieved. The polarization data in the flow-through condition 1 are used for tuning the model parameters, whereas the polarization performances in the other three conditions and the voltage cycling data under DEA operation in Fig. 3.7 are used for validation of the tuned model. Similar to Eq. 2.50, the tuning is to minimize $f(i_{0,O_2}, R_{GDL}) = \sqrt{\frac{\Sigma_1^N (E^{sim}_{cell} - E^{exp}_{cell})^2}{N}}$, where the cell voltage data come from the flow-through polarizations. The tuned parameter values are shown in Table 4.1.

The model prediction shows satisfactory agreement with the experimental data for flow-through operation. The model can capture the performance improvement due to the increased cathode pressure and RH, although the difference is limited as the cathode pressure increases from 2 to 10 psig. Under 100% cathode RH and elevated current density conditions, the model overestimates the voltage probably because the influence of liquid water on the oxygen transport in the cathode channel is not modeled. When the cathode RH has been reduced to 50%, the model prediction is closer to the experimental data at the elevated current densities. The satisfactory agreement at small current densities is important since the model is used for studying DEA operation at low current densities.

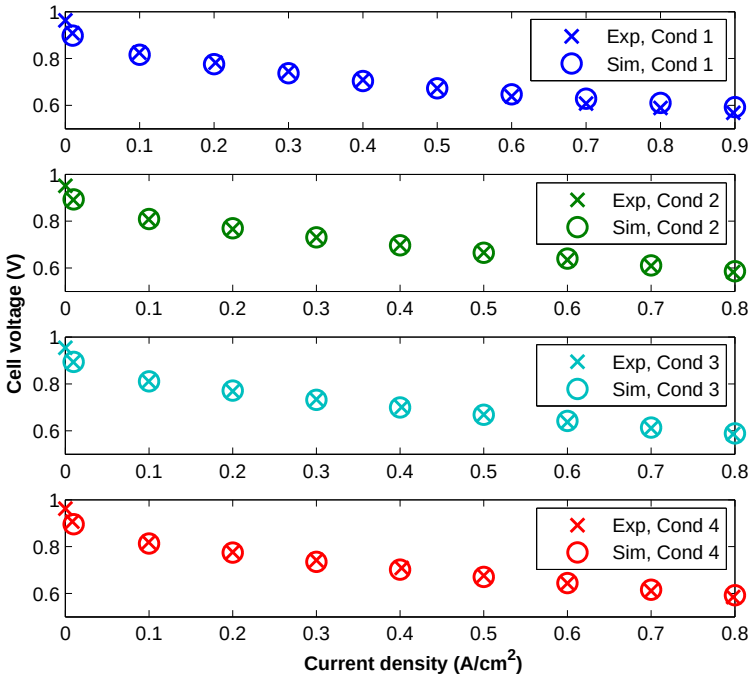

Figure 4.2 The comparison of polarization performance between modeling and experimental data for four sets of operating conditions. Condition 1: pressure 2.5/2.5 psig and RH 100%/100% for anode/cathode; condition 2: pressure 2/2 psig and RH 100%/50% for anode/cathode; condition 3: pressure 2/4 psig and RH 100%/50% for anode/cathode; condition 4: pressure 2/10 psig and RH 100%/50% for anode/cathode. For all conditions, the cell temperature is 60°C and the stoichiometry ratio is 1.2/2.5 for anode/cathode. The model can predict the polarization performance with satisfactory accuracy.

The tuned model can predict the voltage evolution toward an equilibrium in DEA operation when the purge is disabled, with satisfactory agreement compared to the experimental data. Figure 4.3 shows two cases that achieved equilibrium in the experiment after approximately 100 minutes of DEA operation and the simulation results with the same operating conditions. The experimental findings shown in Fig. 4.4 indicate that the cathode pressure needs to be reduced to achieve the equilibrium (2.4 versus 4.0 psig), since large partial pressure of nitrogen could blanket too much area in the anode and shut down the cell. On the other hand, high cathode RH should be avoided in order to obtain an equilibrium because the liquid accumulation could cause a localized shutdown. In Fig. 4.4, the equilibrium was achieved with cathode supply RH of 60%. Generally, the humidified cathode supply introduces additional complexity and randomness in DEA equilibrium. For example, the erratic voltage behavior after reaching equilibrium can be attributed to liquid water condensation in the anode channel, which forms droplets that randomly block the channel before falling

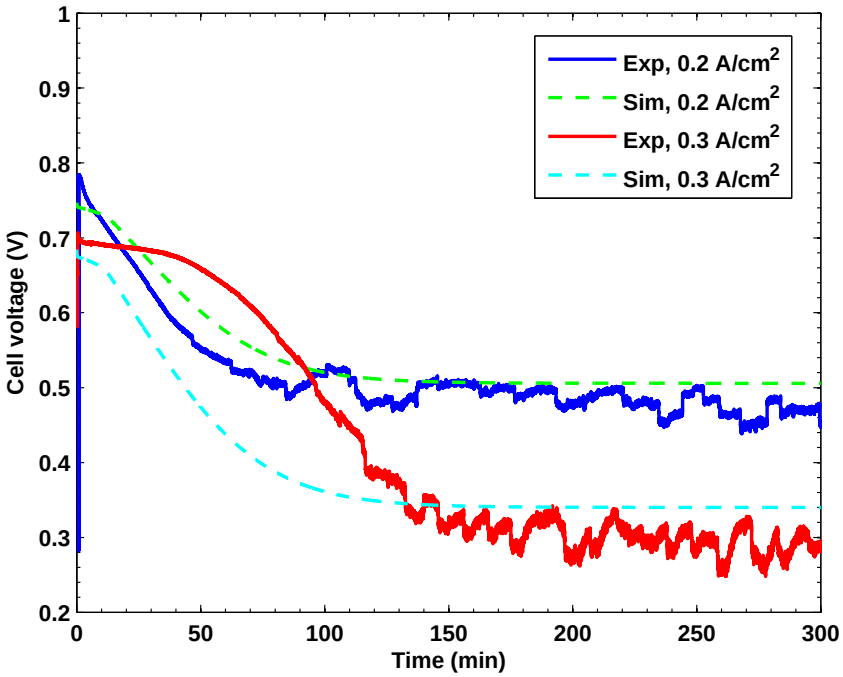

Figure 4.3 The model predicted and experimentally observed voltage evolution towards equilibrium in DEA operation. The operating conditions are 65°C cell temperature, 60% cathode supply RH, 4.0/2.4 psig anode/cathode pressure, and 2.5 cathode SR. The equilibria have been reached with current density of 0.2 and 0.3 A/cm^2

to the bottom of the channel. In addition, the increased local current in the nitrogen non-blanketing region under equilibrium leads to higher water generation rate in the catalyst layer, which also contributes to the erratic voltage. In Fig. 4.3, the case with 0.3 A cm^{-2} shows higher magnitude of voltage oscillation compared with 0.2 A cm^{-2}.

4.3 Reduced Order Modeling

In this section, we analyze the equilibrium behavior using the reduced-order model (ROM) instead of the full-order model (FOM) shown in [68, 69]. The validity of reduced-order modeling will be examined by a comparison with the FOM simulation. It is expected that the existence of DEA equilibrium under a certain set of operating conditions and the influences of operating conditions on the equilibrium can be predicted by the ROM.

The fundamental assumption in developing the ROM is the following: the evolution of N_2 blanketing front is crucial to determine the power output characteristics under a DEA equilibrium. In other words, we anticipate that a ROM that tracks the N_2 blanketing, or H_2

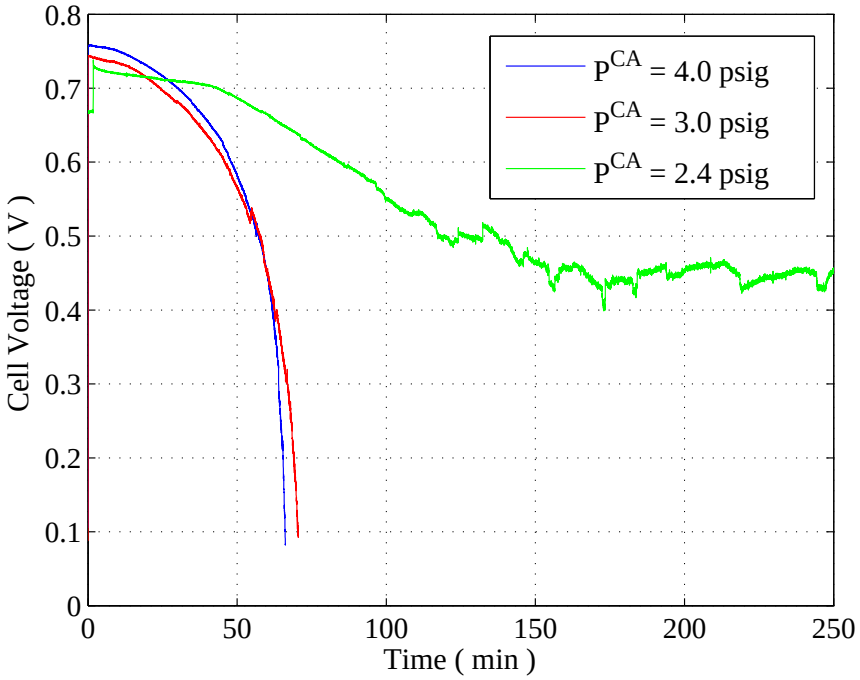

Figure 4.4 The voltage evolutions toward equilibrium with three different cathode pressures. The other operating conditions are 65°C cell temperature, 60% cathode supply RH, 4.0 psig anode pressure, and 0.2 A/cm^2 current density.

Table 4.2 Parameter values in the ROM

Quantity	Value	Unit
D_{H_2/N_2}	1.31	cm^2 s^{-1}
K_{N_2}	0.96×10^{-15}	mol Pa^{-1}m^{-1}s^{-1}
w_{ch}	2.08	mm
w_{lnd}	0.838	mm
h_{an}	1.78	mm
L_{ch}	68.5	mm
δ_{mb}	25	μm
I	10	A
A	50	cm^2
T	338	K
β_{H_2}	0.5	

starvation, front can predict the power under equilibrium and influences from several key operating parameters with sufficient accuracy. The governing equation of N_2 transport is the basis of the ROM in order to track the blanketing front. The following equation of $P_{N_2}^{AN}$ comes from the FOM and holds from the inlet to the end (L_{ch}):

$$\frac{\partial P_{N_2}^{AN}}{\partial t} = \frac{\partial}{\partial y}(D_{N_2}\frac{\partial P_{N_2}^{AN}}{\partial y} - P_{N_2}^{AN}v) + \frac{K_{N_2}RT(w_{ch}+w_{lnd})(P_{N_2}^{CA}-P_{N_2}^{AN})}{\delta_{mb}h_{an}w_{ch}} \tag{4.4}$$

in which $P_{N_2}^{CA}$ is the N_2 partial pressure in the cathode in Pa, D_{N_2} is the Fickian diffusivity of N_2 in $m^2\ s^{-1}$, v is the gas mixture velocity in m s^{-1}, K_{N_2} is the N_2 permeation coefficient in mol $Pa^{-1}\ m^{-1}\ s^{-1}$, δ_{mb} is the membrane thickness, h_{an} is the anode channel height, and w_{ch}/w_{lnd} is the anode channel/land width. The first term in the RHS of Eq. 4.4 represents the diffusive transport, and the second one represents the convective transport. The third term is the source term capturing the N_2 crossover through the membrane depending on the local differential pressure of N_2 between anode and cathode.

The boundary conditions for Eq. 4.4 are zero flux at both ends, i.e., $\frac{\partial P_{N_2}^{AN}}{\partial y}$=0 at y=0 and y=$L_{ch}$, since there is no N_2 flux entering the inlet and leaving the outlet of the anode.

The state equation of H_2 is also needed for deriving a functional dependence of the convective velocity of gas mixture, v(y,t), on $P_{N_2}^{AN}$:

$$\frac{\partial P_{H_2}^{AN}}{\partial t} = \frac{\partial}{\partial y}(D_{H_2}\frac{\partial P_{H_2}^{AN}}{\partial y} - P_{H_2}^{AN}v) - \frac{iRT(w_{ch}+w_{lnd})}{2Fh_{an}w_{ch}} \tag{4.5}$$

in which i(y,t) denotes the local current density in A/cm^2. For simplicity, a saturated anode channel condition is assumed. Therefore,

$$P_{H_2}^{AN} + P_{N_2}^{AN} = P^{AN} - P_{sat} = P_{tot}. \tag{4.6}$$

The total anode pressure is fixed, therefore the time derivative of Eq. 4.6 is zero, and the summation of Eqs. 4.4 and 4.5 yields:

$$P_{tot}\frac{\partial v}{\partial y} = \frac{RT(w_{ch}+w_{lnd})}{h_{an}w_{ch}}\left(\frac{K_{N_2}(P_{N_2}^{CA}-P_{N_2}^{AN})}{\delta_{mb}} - \frac{i}{2F}\right). \tag{4.7}$$

During the DEA operation, the outlet velocity is zero. Therefore $v(t,L)=0$.

The local current density at the anode (H_2 dissociation) can be also described by the Butler-Volmer equation:

$$i(y,t) = i_0\left(P_{H_2}^{AN}\right)^{\beta_{H_2}}\left[\exp\left(\frac{\alpha\eta}{RT}\right) - \exp\left(-\frac{\alpha\eta}{RT}\right)\right] \tag{4.8}$$

in which i_0 is a lumped parameter showing the effects from all pre-multiplier constants in

the Butler-Volmer equation. It is assumed that the local over-potential η is independent of the local H_2 concentration, i.e., η is a constant along the channel. Using Eq. 4.3 to eliminate the exponential term in the Butler-Volmer equation yields the following expression for i(y,t):

$$i(y,t) = \frac{L_{ch} I \left(P_{tot} - P_{N_2}^{AN} \right)^{\beta_{H_2}}}{A \int_0^{L_{ch}} \left(P_{tot} - P_{N_2}^{AN} \right)^{\beta_{H_2}} dy} \tag{4.9}$$

in which I/A (current/area) gives the average current density in A/cm^2. The functional dependence of i(y,t) on the local N_2 concentration is important because the cell voltage can be further estimated with sufficient accuracy in the ROM. Equations 4.4, 4.7 and 4.9 constitute the ROM. The parameter values in the ROM are summarized in Table 4.2. The ROM is solved by Comsol Multiphysics with a mesh size of 0.7 mm and relative tolerance of 1e^{-4}.

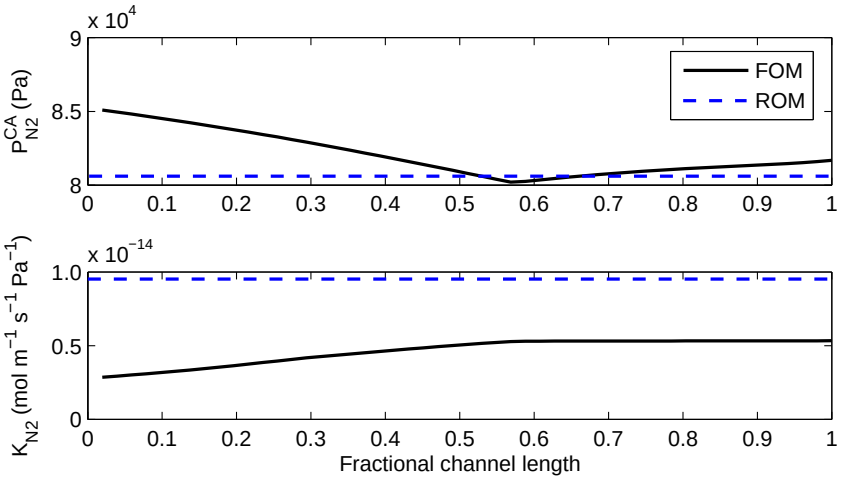

Figure 4.5 The full-order model predicted $P_{N_2}^{CA}$ and K_{N_2} under equilibrium and their values in the reduced-order model under assumption. The operating conditions are 65°C cell temperature, 60% cathode supply RH, 4.0/2.4 psig anode/cathode pressure, 2.5 cathode SR, and 0.2 A/cm^2 current density.

Several assumptions are made in the ROM. First, $P_{N_2}^{CA}$ is assumed to be constant along the cathode channel given the high stoichiometry ratio in the cathode; namely, the small drop of N_2 partial pressure along the channel (about 5%) is neglected. Second, the membrane permeation coefficient K_{N_2} is assumed to be constant since the state of membrane water content is not included in the ROM. Finally, D_{N_2} is assumed to be constant along the channel. The effect of liquid water on diffusivity is neglected. The assumptions in the

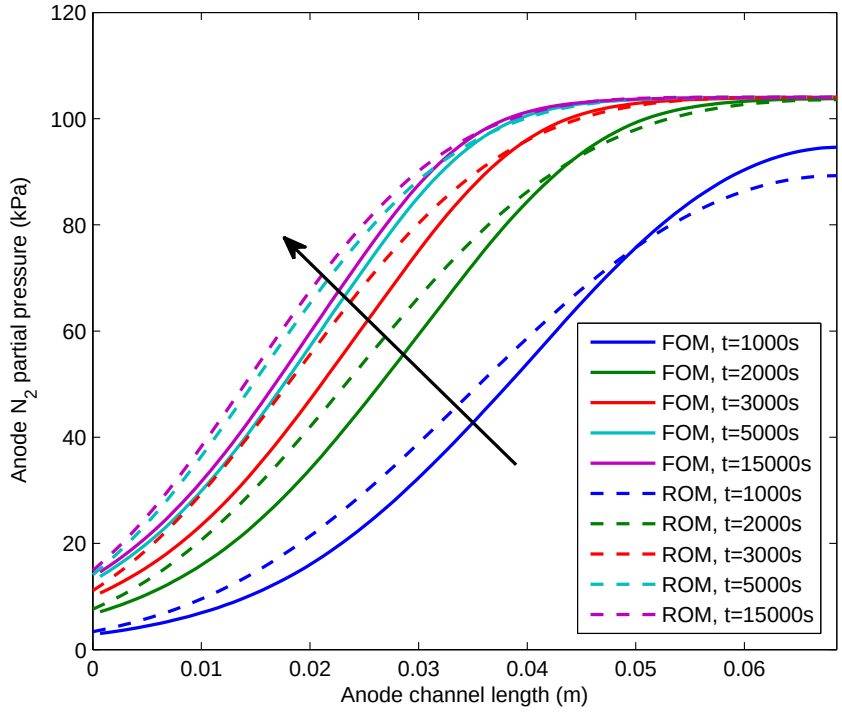

Figure 4.6 The full-order model and reduced-order model predicted evolution of anode N_2 partial pressure toward equilibrium with the same operating conditions as in Fig. 4.5.

ROM are compared with the FOM simulations in Fig. 4.5. In the upper subplot of Fig. 4.5, the non-monotonic distribution of $P_{N_2}^{CA}$ comes from a combined effect of local oxygen/vapor partial pressure determined by local current. Since the cathode pressure is maintained at a constant, the decreasing oxygen partial pressure along the channel tends to produce a monotonically increasing partial pressure of nitrogen, whereas the increasing vapor partial pressure leads to an opposite trend. The turning point in the subplot for $P_{N_2}^{CA}$ indicates the location where the effect of vapor pressure becomes less dominant as it approaches the saturation pressure. In the lower subplot of Fig. 4.5, the K_{N_2} of ROM is larger than that of FOM in order to match the rate of N_2 accumulation in the FOM, which is consistent with the prior assumption of a saturated anode channel.

A comparison of the ROM predictions based on these assumptions against the actual parameter values by the FOM simulation is presented in Figs. 4.6 and 4.7. The evolutions of $P_{N_2}^{AN}$ from both FOM and ROM are shown in Fig. 4.6. An equilibrium has been achieved since the changes after t=5000 s are slight in both FOM and ROM, with a nitrogen blanketing front at approximately 0.6 fractional channel location. The ROM can not only predict the N_2 distribution under equilibrium, but also capture the evolution toward equilibrium

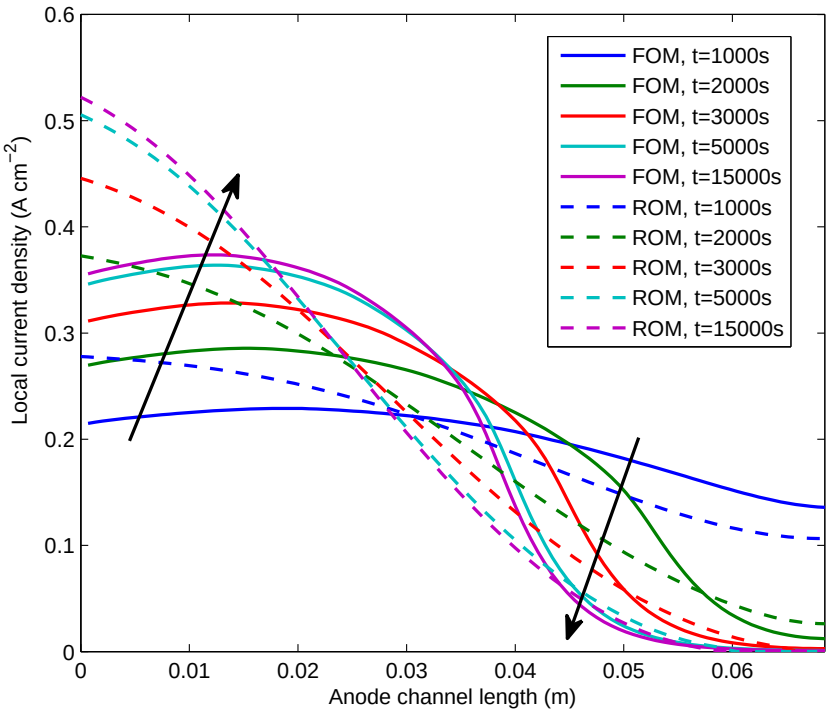

Figure 4.7 The full-order model and reduced-order model predicted evolution of local current density toward equilibrium with the same operating conditions as in Fig. 4.5.

accurately since the N_2 distributions at selected times are very close from both models.

Fig. 4.7 presents the evolutions of local current from both models. The ROM predicts a monotonically decreasing local current along the channel, whereas the FOM demonstrates the non-monotonic spatial variation of local current. Since the ROM assumes a constant membrane state along the channel and the local current depends only the local H_2 concentration, it cannot capture the non-monotonic local current distribution due to a combined effect from membrane self-humidification by the reaction generated water and hydrogen depletion along the channel. The FOM can predict the non-homogeneity with additional membrane states.

4.4 Parametric Sensitivity

We have shown that the ROM can predict the nitrogen evolution toward an equilibrium (Fig. 4.6) with satisfactory accuracy against the FOM. However, this finding only shows the validity of the ROM under one set of operating conditions. It is also of interest to examine whether the parametric sensitivity of the ROM is consistent with that of experimental

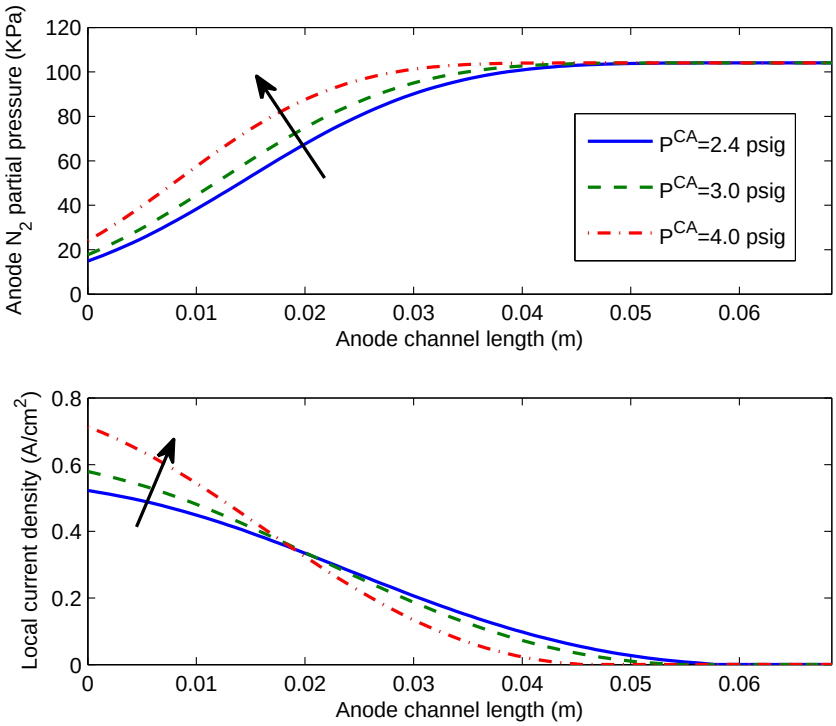

Figure 4.8 The reduced-order model predicted anode N_2 partial pressure and local current density distribution at equilibrium with increasing cathode pressures from 2.4, 3.0 to 4.0 psig. The other operating conditions are the same as those in Fig. 4.5.

data. Cathode pressure is chosen to perform this parametric study.

Fig. 4.8 presents the distributions of nitrogen partial pressure and local current density under equilibrium from the ROM simulations with increasing cathode pressures. The upper subplot shows that more channel region becomes blanketed as the cathode pressure increases. Correspondingly, the local current density in the non-blanketing region increases dramatically, as shown in the lower subplot. When P^{CA} increases to 4.0 psig, the local current density can exceed three times the average current density, which leads to a high local water generation rate and tends to shut down the cell. These findings are consistent with the experimental observations shown in Fig. 4.4 in which an equilibrium with reasonable power output (anode channel partially blanketed by N_2) was not found for higher cathode pressures.

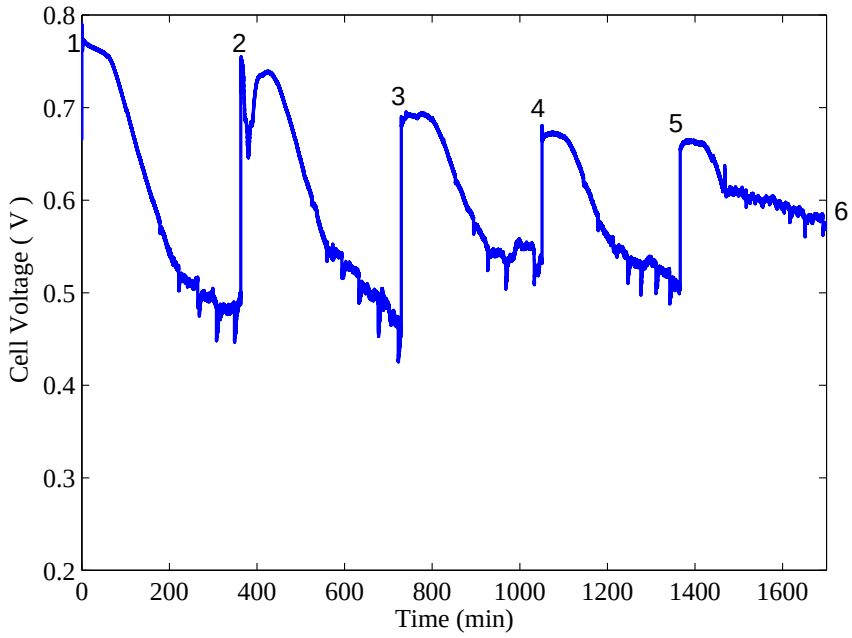

Figure 4.9 The voltage evolution with purging disabled. The experimental conditions are 0.2 A/cm^2 current density, 65°C cell temperature, 60% cathode supply RH, 4.0/2.4 psig anode/cathode pressure, and 2.5 cathode SR. The flow-through polarization evaluations were performed periodically after the purge. The numbers from one to six correspond to the six polarization curves in Fig. 4.10

4.5 Degradation under Equilibrium

Under the equilibrium operation, the fuel starvation condition at the channel end remains until a purge is performed. Thus, the carbon corrosion and associated voltage degradation become non-negligible. Figure 4.9 presents the voltage evolution during the extended DEA operation, and Fig. 4.10 shows the flow-through polarizations after performing each purging labeled in Fig. 4.9. The experimental data indicate the gradual and irreversible decay of after-purge voltage, as shown in Fig. 4.9. It is not clear as to whether an equilibrium had been achieved between certain purges, e.g., the No. 2 and No. 3 purges. Also, an explanation lacks for the recovery of pre-purging voltage observed after the No. 3 purge.

Nevertheless, an evaluation of the influences from carbon corrosion on polarization can be performed, as shown in Fig. 4.10. The initial carbon loading is assumed to be 0.21 mg/cm^2 (constant along the channel) together with a Pt/C ratio of one in order to match the first polarization curve from experimental data. The subsequent two polarizations after the No. 2 and No. 3 purges show satisfactory agreement with the simulation results after identical time of DEA operation. After the No. 3 purge, the simulation predicts higher polarizations than the experiment creates probably due to the membrane degradation that

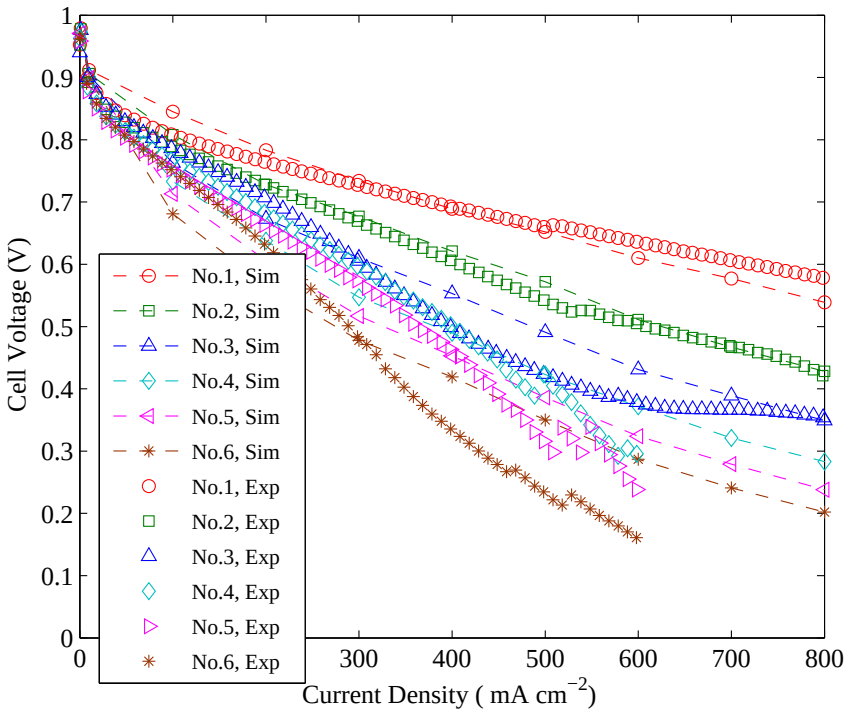

Figure 4.10 The polarization drop due to the equilibrium operation corresponding to the six evaluations in Fig. 4.9. The dashed lines indicate the simulation results whereas all markers are from experiments. The operating conditions for flow-through polarizations are 65°C cell temperature, 100% anode/cathode supply RH, 4.0/4.0 psig anode/cathode pressure, and 1.2/2.5 anode/cathode SR.

is not captured by modeling.

The durability becomes a concern if the DEA cell is operated under the equilibrium mode (purging disabled). The degradation can be alleviated by removing or reducing the catalyst loading in the fuel starvation region, since it has been shown in Chapter 2 that the corrosion rate depends highly on the Pt loading. In the channel-end regions that suffer complete fuel starvation, Pt loading is unnecessary. Essentially, the novel design appears to be a normally working cell in parallel to a nitrogen and water reservoir, the size ratio between which can be determined by our validated model. Such a novel DEA cell with variable catalyst loading is suitable for operations without purging due to the improved resistance to carbon corrosion.

4.6 Conclusions

The evolution of the nitrogen blanketing front and subsequent equilibrium in dead-ended anode operation of a fuel cell is shown to depend on the nitrogen distribution in the anode channel. The equilibrium mechanism can be summarized as zero net flux of nitrogen crossover through the membrane. For a wide range of cathode pressure, the simulation results from the tuned full-order model (FOM) match the experimental data with satisfactory accuracy. Both the FOM simulation and experimental data indicate the existence of such equilibrium, represented by voltage evolution toward a steady state, under certain operating conditions. The voltage degradation under equilibrium and the corresponding polarization drop are identified.

An assumption for the functional dependence of local current density on the N_2 partial pressure in the anode is used to calculate the convective velocity. This enables the formulation of a simplified single-state second-order PDE system to study the equilibrium behavior under DEA operation. The reduced-order model (ROM) can predict the evolution of N_2 partial pressure toward equilibrium with satisfactory accuracy as compared with the FOM. It also can capture the influences of cathode pressure on the distributions of nitrogen and local current density under equilibrium, indicating a consistent trend with the experimental data. In the future, the assumption of uniform cathode over-potential will be relaxed and a distributed voltage model will be incorporated into the ROM framework, thus enabling comparison with the equilibrium voltage data from the experiments. It is also of interest to examine the influences of geometrical parameters such as channel depth on the equilibrium by both experiments and full-order modeling, in addition to the operating parameters such as cathode pressure shown in Fig. 4.4. Furthermore, design and testing of a novel cell with variable catalyst loading and therefore improved resistance to carbon corrosion are necessary to operate a DEA cell without purging in low-power applications.

Chapter 5
Conclusions and Future Work

5.1 Research Motivation Revisited

The dead-ended anode operation of fuel cells, as opposed to the flow-through modes, has several attractive advantages, such as reduced system weight, cost, and complexity which make it a potential candidate for portable power applications. Our prior work has shown the nitrogen front evolution and voltage drop in DEA operation from both modeling and experiment. The nitrogen blanketing and water flooding in the anode generally lead to the local fuel starvation, which raises a concern of durability.

Advancing the prior study on nitrogen front evolution in DEA cell by dynamic model development [82], this dissertation research has focused on the practical aspects of the DEA operation, i.e., durability and efficiency, that are essential for developing a commercial system based on a DEA architecture. It is unclear that whether the simplified system architecture and reduced cost are offset by the shorter lifetime due to the degradation issue. By the optimization of the purging schedule, it is anticipated to improve the lifetime efficiency while maintaining the simplified system architecture. It is also of interest to explore the simplest way to operate a fuel cell, a DEA cell with purging disabled being one possibility. Such a system will feature fewest BOP components and efforts in purging optimization, yet suffer from small power density and short lifetime.

5.2 Summary of Findings

In this thesis, the cathode carbon corrosion due to the anode fuel starvation is studied via simulation. To better predict the voltage degradation, the model also captures the loss of active catalytic sites due to carbon corrosion by correlating it with the amount of carbon mass remained in the catalyst layer via a power law. The cathode carbon corrosion rate exhibits

spatiotemporal evolution along the channel, with the highest rate found at the channel-end region before the purge when the hydrogen starvation is most severe (Section 2.7). If the purge can be scheduled before severe hydrogen starvation, the carbon corrosion at the channel end and therefore the voltage degradation will be greatly mitigated. In the inlet and middle channel regions, the corrosion rate is normally mild due to the availability of hydrogen fuel with reasonable cycle duration and current load. The decreasing voltage in galvanostatic DEA operation in fact mitigates the cathode carbon corrosion rate by reducing the interfacial potential between membrane and electrode in the cathode.

Motivated by the influences of purge scheduling on the durability, the cycle duration and purge interval were optimized in order to achieve highest lifetime efficiency of a DEA cell. The lifetime efficiency is defined upon three interrelated objectives: the hydrogen loss during the purge, the average voltage output between the purges, and the voltage decrease due to the carbon corrosion caused by hydrogen starvation over the lifetime of the DEA operation. The study therefore elucidates the following concerns on DEA operation. First, how does one achieve high hydrogen utilization? Although the DEA operation reaches anode stoichiometry ratio of unity within a cycle, there could be hydrogen loss due to the purge between two consecutive cycles. This part of hydrogen loss should be considered while evaluating the overall hydrogen economy. Second, although it is usually stated as one major benefit of DEA operation, is it worthwhile to achieve highest hydrogen utilization?

We have shown that, for some operating conditions, controling the purge interval can achieve highest hydrogen utilization, or zero hydrogen loss during the purge (Subsection 3.5.1). However, with such an operating schedule, the lifetime efficiency is not highest because of the more severe carbon corrosion and additional amount of voltage degradation, as well as the smaller average voltage in a cycle due to the incomplete removal of the accumulated nitrogen in the channel end. Considering cycle duration and purge interval together, it is found that a medium cycle duration without severe hydrogen starvation at the channel end together with a short purge interval leads to the best DEA cell efficiency at a current density of 0.6 A/cm^2 (Subsection 3.5.4). Also, the simulation shows small variation of efficiency within the target domain, which suggests that, as long as the purge interval can be selected from the target range, further optimization may not be necessary.

After the optimization study on the purge scheduling, the focus was finally on the DEA operation without purging, which is the simplest way to operate a fuel cell. Both simulation and experimental results indicate that an equilibrium in galvanostatic DEA operation, which achieves relatively small power, can be established with low cathode RH and pressure as well as reduced current load (Section 4.2). It is possible to operate the DEA cell under this equilibrium condition as long as the carbon corrosion due to the extended dura-

tion of fuel starvation can be alleviated by novel cell design.

The present modeling of the spatiotemporal evolution of species and local potential provides a comprehensive foundation for modeling other power systems. The model-based lifetime efficiency evaluation and analysis including the degradation effects can be also used to examine other peer systems. Therefore, this dissertation work not only addresses the concerns in developing a commercial DEA fuel cell system, but also provides useful tools for general power system analysis and development. For example, in a mainstream fuel cell system that applies anode recirculation, there is also nitrogen and water crossover and accumulation in the anode [101]. The periodic anode purging is necessary to remove the impurities and to maintain sufficient hydrogen concentration. The present modeling framework of species distribution in the anode and purge flow can be readily utilized in the RCA system due to the similarity, although modification to fit the open-ended anode and consideration of hydrogen pulsation [118] are necessary. The carbon corrosion submodel and purge optimization technique also remain valid and can be used directly in an RCA scenario.

5.2.1 Highlights of Key Findings

Given the specific operating conditions reported in Section 3.5, the significant findings from model-based purge optimization are summarized below:

– With a short purge interval (54 ms), there is 10 mV irreversible decay of after-purge voltage throughout 38 h DEA operation, corresponding to a 25% loss of carbon mass at 0.9 fractional channel location (Fig. 3.6).

– The lifetime efficiency of a DEA cell can be improved from $<$20% to around 50% by simply reducing the purge interval from 900 ms to the minimum operating time of the solenoid valve (Fig. 3.3).

– With a medium cycle duration of 600 s, the lifetime efficiency is highest. A 4% efficiency increase (approximately from 47% to 51%) has been achieved by optimization within the target domain (Fig. 3.13).

– The most efficient cycle duration of 600 s leads to an irreversible decay of about 5 mV in after-purge voltage after 33 h DEA operation (Fig. 3.14).

– As shown in Figs. 3.14 and 3.13, the shortest cycle duration (100 s) yields the maximum energy output (2020 KJ) within the 33 h DEA operation and the minimum voltage decay (1 mV), with the associated lifetime efficiency being lowest in the target domain (around 47%). These data are helpful when one needs to trade between efficiency and power/durability.

5.3 Future Work

The dissertation research can be further extended in the following aspects. First, the isothermal assumption in the present model may introduce non-negligible error due to the uneven local current distribution, and therefore heat generation, observed with many operating conditions in DEA operation. The isothermal assumption shall be relaxed in the future. Second, the RH cycling and chemical degradation on the membrane applies additional influences on the DEA cell. Severe membrane degradation has been observed in an aged cell with DEA [39, 25]. The voltage discrepancy between present model and experiment shown in Fig. 3.7 suggests the influence of ongoing membrane degradation that has not been modeled. A thorough investigation of the membrane degradation during DEA operation thus becomes essential.

The oxidization of carbon, dissolution and mitigation (or particle size change) of Pt and membrane polymer decomposition lead to a combined degradation and the individual contribution is difficult to be separated. To examine the degradation solely from membrane, very small current load is desired (less than 0.1 A/cm^2) to minimize the carbon corrosion. However, such degradation test may be extremely time consuming and special accelerated stress testing (AST) needs to be designed for the DEA cell. Alternatively, a modeling approach can be conducted to capture the species concentration relating to the membrane chemical degradation and the corresponding voltage decay, some prior works being Refs. [131, 132, 133]. Nevertheless, the physical deformation/delamination of the membrane [25] due to the cycling and dry conditions can hardly be captured by modeling and still requires AST to investigate.

It is necessary to extend the present study of carbon corrosion modeling. Due to the unavailability of a CO_2 analyzer, the carbon corrosion rate ($i_{C,0}$) has not been tuned directly. Instead, the value of $i_{C,0}$ is taken from the literature and validated with the voltage degradation data. It is of interest to determine the parameter values of $i_{C,0}$ and q from systematic experiment with direct measurement of CO_2 ppm at the cathode outlet. For different types of carbon, these two parameters vary, indicating different resistances against corrosion.

From the system prospective, the present model can be incorporated into a fuel cell system-level model to evaluate the trade-off between cost and power density. Specifically, the statement of cost reduction due to the system simplification does not take into account the relatively low power density of a DEA fuel cell when comparing with the RCA system. A further evaluation of $/Kw from both systems is very necessary. To this end, the BOP components should be modeled in addition to the DEA cell itself.

Bibliography

[1] J. Larminie and A. Dicks, *Fuel Cell System Explained, John Wiley and Sons*. John Wiley & Sons, 2003.

[2] J. Wu, X. Z. Yuan, J. J. Martina, H. Wang, J. Zhang, J. Shen, S. Wu, and W. Merida, "A review of PEM fuel cell durability: Degradation mechanisms and mitigation strategies," *Journal of Power Sources*, vol. 184, pp. 104–119, 2008.

[3] A. Shah, G.-S. Kim, W. Gervais, A. Young, K. Promislow, J. Li, and S. Ye, "The effects of water and microstructure on the performance of polymer electrolyte fuel cells," *Journal of Power Sources*, vol. 160, pp. 1251–1268, 2006.

[4] B. A. McCain, A. G. Stefanopoulou, and I. V. Kolmanovsky, "On the dynamics and control of through-plane water distributions in PEM fuel cells," *Chemical Engineering Science*, vol. 63, pp. 4418–4432, 2008.

[5] [Online]. Available: www1.eere.energy.gov/hydrogenandfuelcells/accomplishments.html

[6] Y. Wang, K. S. Chen, J. Mishler, S. C. Cho, and X. C. Adroher, "A review of polymer electrolyte membrane fuel cells: Technology, applications, and needs on fundamental research," *Applied Energy*, vol. 88, pp. 981–1007, 2011.

[7] [Online]. Available: www1.eere.energy.gov/hydrogenandfuelcells/fuelcells/fc_challenges.html

[8] (2011, August) DOE hydrogen and fuel cells program record – fuel cell system cost 2011. [Online]. Available: www.hydrogen.energy.gov/pdfs/11012_fuel_cell_system_cost.pdf

[9] M. Skyllas-Kazacos, M. H. Chakrabarti, S. A. Hajimolana, F. S. Mjalli, and M. Saleem, "Progress in flow battery research and development," *Journal of the Electrochemical Society*, vol. 158, pp. R55–R79, 2011.

[10] C. P. de Leon, A. Fras-Ferrer, J. Gonzalez-Garca, D. A. Szanto, and F. C. Walsh, "Redox flow cells for energy conversion," *Journal of Power Sources*, vol. 160, pp. 716–732, 2006.

[11] A. Z. Weber, M. M. Mench, J. P. Meyers, P. N. Ross, J. T. Gostick, and Q. Liu, "Redox flow batteries: A review," *Journal of Applied Electrochemistry*, vol. 41, pp. 1137–1164, 2011.

[12] K. Huang, X. Li, S. Liu, N. Tan, and L. Chen, "Research progress of vanadium redox flow battery for energy storage in China," *Renewable Energy*, vol. 33, pp. 186–192, 2008.

[13] P. Zhao, H. Zhang, H. Zhou, J. Chen, S. Gao, and B. Yi, "Characteristics and performance of 10kw class all-vanadium redox-flow battery stack," *Journal of Power Sources*, vol. 162, pp. 1416–1420, 2006.

[14] K. T. Cho, P. Ridgway, A. Z. Weber, S. Haussener, V. Battaglia, and V. Srinivasan, "High performance hydrogen/bromine redox flow battery for grid-scale energy storage," *Journal of the Electrochemical Society*, vol. 159, pp. A1806–A1815, 2012.

[15] V. Viswanathan, A. Crawford, L. Thaller, D. Stephenson, S. Kim, W. Wang, G. Coffey, P. Balducci, Z. G. Yang, L. Li, M. Kintner-Meyer, and V. Sprenkle, "Estimation of capital and levelized cost for redox flow batteries," in *USDOE-OE ESS Peer Review at Washington, DC*, 2012.

[16] J. A. Kosek and A. B. Laconti, "Advanced hydrogen electrode for a hydrogen-bromine battery," *Journal of Power Sources*, vol. 22, pp. 293–300, 1988.

[17] V. Srinivasan, A. Z. Weber, and V. Battaglia, "Hydrogen/bromine redox flow battery for grid-scale energy storage," in *USDOE-OE ESS Peer Review at Washington, DC*, 2012.

[18] A. Creeth, "Pt-free PEM cathode technology with fundamental durability benefits: Flowcath," *Fuel Cells Bulletin*, vol. April, pp. 12–15, 2011.

[19] A. LaConti, In ACS polymer division topical workshop on perfluorinated ionomer membranes, 1982, lake Buena Vista, FL.

[20] A. B. LaConti, M. Hamdan, and R. C. McDonald, "Mechanisms of membrane degradation," *Handbook of Fuel Cells-Fundamentals, Technology and Application*, vol. 3, John, Wiley and Sons, 2003.

[21] R. Ahluwalia and X. Wang, "Fuel cell systems for transportation: Status and trends," *Journal of Power Sources*, vol. 177, pp. 167–176, 2008.

[22] S. Kocha, J. Yang, and J. Yi, "Characterization of gas crossover and its implications in PEM fuel cells," *AIChE Journal*, vol. 52, pp. 1916–1925, 2006.

[23] E. Muller, F. Kolb, L. Guzzella, A. Stefanopoulou, and D. McKay, "Correlating nitrogen accumulation with temporal fuel cell performance," *Journal of Fuel Cell Science and Technology*, vol. 7, pp. 021 013–1–021 013–11, 2010.

[24] C.-Y. Wang, "Fundamental models for fuel cell engineering," *Chemical Reviews*, vol. 104, pp. 4727–4766, 2004.

[25] T. Matsuura, J. Chen, J. B. Siegel, and A. G. Stefanopoulou, "Degradation phenomena in PEMFC with dead-ended anode," *International Journal of Hydrogen Energy*, In press, 10.1016/j.ijhydene.2013.06.096, 2013.

[26] R. Borup, J. Meyers, B. Pivovar, Y.-S. Kim, R. Mukundan, N. Garland, D. Myers, M. Wilson, F. Garzon, D. Wood, P. Zelenay, K. More, K. Stroh, T. Zawodzinski, J. Boncella, J. McGrath, M. Inaba, K. Miyatake, M. Hori, K. Ota, Z. Ogumi, S. Miyata, A. Nishikata, Z. Siroma, Y. Uchimoto, K. Yasuda, K. Kimijima, and N. Iwashita, "Scientific aspect of polymer electrolyte fuel cell durability and degradation," *Chemical Reviews*, vol. 107, pp. 3904–3951, 2007.

[27] J. St-Pierre and N. Jia, "Successful demonstration of ballard PEMFCs for space shuttle applications," *J. New Mater. Electrochem. Syst.*, vol. 5, pp. 263–271, 2002.

[28] J. Xie, D. Wood, K. More, P. Atanassov, and R. Borup, "Microstructural changes of membrane electrode assemblies during pefc durability testing at high humidity conditions," *Journal of the Electrochemical Society*, vol. 152, pp. A1011–A1020, 2005.

[29] V. Mehta and J. Cooper, "Review and analysis of pem fuel cell design and manufacturing," *Journal of Power Sources*, vol. 114, pp. 32–53, 2003.

[30] M. Watanabe, K. Tsurumi, T. Mizukami, T. Nakamura, and P. Stonehart, "Activity and stability of ordered and disordered Co-Pt alloys for phosphoric acid fuel cells," *Journal of the Electrochemical Society*, vol. 141, pp. 2659–2668, 1994.

[31] T. Akita, A. Taniguchi, J. Maekawa, Z. Siroma, K. Tanaka, M. Kohyama, and K. Yasuda, "Analytical TEM study of pt particle deposition in the proton-exchange membrane of a membrane-electrode-assembly," *Journal of Power Sources*, vol. 159, pp. 461–467, 2006.

[32] Y. Zhai, H. Zhang, D. Xing, and Z. Shao, "The stability of Pt/C catalyst in H_3PO_4/PBI PEMFC during high temperature life test," *Journal of Power Sources*, vol. 164, pp. 126–133, 2007.

[33] R. Darling and J. Meyers, "Kinetic model of platinum dissolution in PEMFCs," *Journal of the Electrochemical Society*, vol. 150, pp. A1523–A1527, 2003.

[34] ——, "Mathematical model of platinum movement in PEM fuel cells," *Journal of the Electrochemical Society*, vol. 152, pp. A242–A247, 2005.

[35] C. Reiser, L. Bregoli, T. Patterson, J. Yi, J. Yang, M. Perry, and T. Jarvi, "A reverse-current decay mechanism for fuel cells," *Electrochemical Solid-State Letters*, vol. 8, pp. A273–A276, 2005.

[36] J. Meyers and R. Darling, "Model of carbon corrosion in PEM fuel cells," *Journal of the Electrochemical Society*, vol. 153, pp. A1432–A1442, 2006.

[37] H. Tang, Z. Qi, M. Ramani, and J. Elter, "Pem fuel cell cathode carbon corrosion due to the formation of air/fuel boundary at the anode," *Journal of Power Sources*, vol. 158, pp. 1306–1312, 2006.

[38] L. Roen, C. Paik, and T. Jarvi, "Electrocatalytic corrosion of carbon support in PEMFC cathodes," *Electrochemical Solid-State letters*, vol. 7, pp. A19–A22, 2004.

[39] T. Matsuura, J. Siegel, J. Chen, and A. Stefanopoulou, "Multiple degradation phenomena in polymer electrolyte fuel cell operation with dead-ended anode," *Proceeding of ASME 2011 5th International Conference on Energy Sustainability & 9th Fuel Cell Science, Engineering and Technology Conference*, Washington D.C., 2011.

[40] V. Mittal, H. Kunz, and J. Fenton, "Membrane degradation mechanisms in PEMFCs," *Journal of the Electrochemical Society*, vol. 154, pp. B652–B656, 2007.

[41] D. Curtin, R. Lousenberg, T. Henry, P. Tangeman, and M. Tisack, "Advanced materials for improved PEMFC performance and life," *Journal of Power Sources*, vol. 131, pp. 41–48, 2004.

[42] S. Scherer, S. Schlagowski, and E. Fischer, "PEM water electrolysers: evidence for membrane failure in 100kw demonstration plants," *Journal of Applied Electrochemistry*, vol. 28, pp. 1041–1049, 1998.

[43] M. Geske, M. Heuer, G. Heideck, and Z. A. Styczynski, "Current density distribution mapping in PEM fuel cells as an instrument for operational measurements," *Energies*, vol. 3, pp. 770–783, 2010.

[44] I. Alaefour, G. Karimi, K. Jiao, and X. Li, "Measurement of current distribution in a proton exchange membrane fuel cell with various flow arrangements," *Applied Energy*, vol. 93, pp. 80–89, 2012.

[45] K. Jiao, I. Alaefour, G. Karimi, and X. Li, "Simultaneous measurement of current and temperature distributions in a proton exchange membrane fuel cell during cold start processes," *Electrichimita Acta*, vol. 56, pp. 2967–2982, 2011.

[46] D. Spernjak, P. P. Mukherjee, R. Mukundan, J. Davey, D. S. Hussey, D. Jacobsonf, and R. L. Borup, "Measurement of water content in polymer electrolyte membranes using high resolution neutron imaging," *ECS Transaction*, vol. 33, pp. 1451–1456, 2010.

[47] Z. Zhang, J. Martin, J. Wu, H. Wang, K. Promislow, and B. J. Balcom, "Magnetic resonance imaging of water content across the nafion membrane in an operational PEM fuel cell." *Journal of Magnetic Resonance*, vol. 193, pp. 259–266, 2008.

[48] D. Bernardi and M. Vebrunge, "A mathematical model of the solid-polymer-electrolyte fuel cell," *Journal of the Electrochemical Society*, vol. 139, pp. 2477–2491, 1992.

[49] T. Springer, T. Zawodzinski, and S. Gottesfeld, "Polymer electrolyte fuel cell model," *Journal of the Electrochemical Society*, vol. 138, pp. 2334–2342, 1991.

[50] T. Fuller and J. Newman, "Water and thermal management in solid polymer electrolyte fuel cell," *Journal of the Electrochemical Society*, vol. 140, pp. 1218–1225, 1993.

[51] T. Nguyen and R. White, "A water and thermal management model for proton exchange membrane fuel cells," *Journal of the Electrochemical Society*, vol. 140, pp. 2178–2186, 1993.

[52] V. Gurau, H. Liu, and S. Kakac, "Two-dimensional model for proton exchange membrane fuel cells," *AIChE Journal*, vol. 44, pp. 2410–2422, 1998.

[53] S. Um, C.-Y. Wang, and K. Chen, "Computational fluid dynamics modeling of proton exchange membrane fuel cells," *Journal of the Electrochemical Society*, vol. 147, pp. 4485–4493, 2000.

[54] S. Um and C. Wang, "Three-dimensional analysis of transport and electrochemical reactions in polymer electrolyte fuel cells," *Journal of Power Sources*, vol. 125, pp. 40–51, 2004.

[55] H. Meng and C. Wang, "Large-scale simulation of polymer electrolyte fuel cells by parallel computing," *Chemical Engineering Science*, vol. 59, pp. 3331–3343, 2004.

[56] Y. Wang and C.-Y. Wang, "Modeling polymer electrolyte fuel cells with large density and velocity changes," *Journal of the Electrochemical Society*, vol. 152, pp. A445–A453, 2005.

[57] Z. Wang, C.-Y. Wang, and K. Chen, "Two-phase flow and transport in the air cathode of proton exchange membrane fuel cells," *Journal of Power Sources*, vol. 94, pp. 40–50, 2001.

[58] U. Pasaogullari and C. Wang, "Two-phase transport and the role of micro-porous layer in polymer electrolyte fuel cells," *Electrochimica Acta*, vol. 49, pp. 4359–4369, 2004.

[59] S. Mazumder and J. V. Cole, "Rigorous 3-d mathematical modeling of PEM fuel cells ii. model predictions with liquid water transport," *Journal of the Electrochemical Society*, vol. 150, pp. A1510–A1517, 2003.

[60] E. Birgersson, M. Noponen, and M. Vynnycky, "Analysis of a two-phase nonisothermal model for a PEFC," *Journal of the Electrochemical Society*, vol. 152, pp. A1021–A1034, 2005.

[61] Y. Wang, S. Basu, and C.-Y. Wang, "Modeling two-phase flow in PEM fuel cell channels," *Journal of Power Sources*, vol. 179, pp. 603–617, 2008.

[62] K. Jiao and X. Li, "Three-dimensional multiphase modeling of cold start processes in polymer electrolyte membrane fuel cells," *Electrochimica Acta*, vol. 54, pp. 6876–6891, 2009.

[63] ——, "Effects of various operating and initial conditions on cold start performance of polymer electrolyte membrane fuel cells," *International Journal of Hydrogen Energy*, vol. 34, pp. 8171–8184, 2009.

[64] K. Jiao, I. E. Alaefour, G. Karimi, and X. Li, "Cold start characteristics of proton exchange membrane fuelcells," *International Journal of Hydrogen Energy*, vol. 36, pp. 11 832–11 845, 2011.

[65] J. Siegel, A. Stefanopoulou, G. Ripaccioli, and S. Di Cairano, "Purge scheduling for dead-ended anode operation of PEM fuel cells" *The Control Handbook: Control System Applications, Second Edition* , W. S. Levine, Ed. CRC Press, 2010.

[66] J. Siegel, S. Bohac, A. Stefanopoulou, and S. Yesilyurt, "Nitrogen front evolution in purged polymer electrolyte membrane fuel cell with dead-ended anode," *Journal of the Electrochemical Society*, vol. 157, pp. B1081–B1093, 2010.

[67] J. Siegel, D. McKay, A. Stefanopoulou, D. Hussey, and D. Jacobson, "Measurement of liquid water accumulation in a PEMFC with dead-ended anode," *Journal of the Electrochemical Society*, vol. 155, pp. B1168–B1178, 2008.

[68] J. Chen, J. B. Siegel, T. Matsuura, and A. G. Stefanopoulou, "Carbon corrosion in PEM fuel cell dead-ended anode operations," *Journal of the Electrochemical Society*, vol. 158, pp. B1164–B1174, 2011.

[69] J. Chen, J. B. Siegel, A. G. Stefanopoulou, and J. R. Waldecker, "Optimization of purge cycle for dead-ended anode fuel cell operation," *International Journal of Hydrogen Energy*, vol. 38, pp. 5092–5105, 2013.

[70] J. Chen, J. B. Siegel, T. Matsuura, A. G. Stefanopoulou, and S. Yesilyurt, "Experimental validation of equilibria in fuel cells with dead-ended anodes," in *European Control Conference*, 2013.

[71] W. Hogarth and J. Benziger, "Operation of polymer electrolyte membrane fuel cells with dry feeds: Design and operating strategies," *Journal of Power Sources*, vol. 159, pp. 968–978, 2006.

[72] J. Benziger, E. Chia, E. Karnas, J. Moxley, C. Teuscher, and I. Kevrekidis, "The stirred tank reactor polymer electrolyte membrane fuel cell," *AIChE Journal*, vol. 50, pp. 1889–1990, 2004.

[73] J. Hu, P. Sui, S. Kumar, and N. Djilali, "Modelling and simulations of carbon corrosion during operation of a polymer electrolyte membrane fuel cell," *Electrochimica Acta*, vol. 54, pp. 5583–5592, 2009.

[74] J. H. Ohs, U. Sauter, S. Maass, and D. Stolten, "Modeling hydrogen starvation conditions in proton-exchange membrane fuel cells," *Journal of Power Sources*, vol. 196, pp. 255–263, 2011.

[75] A. Young, J. Stumper, and E. Gyenge, "Characterizing the structural degradation in a PEMFC cathode catalyst layer: Carbon corrosion," *Journal of Electrochemical Society*, vol. 156, pp. B913–B922, 2009.

[76] T. W. Patterson and R. M. Darling, "Damage to the cathode catalyst of a PEM fuel cell caused by localized fuel starvation," *Electrochemical and Solid-State Letters*, vol. 9, pp. A183–A185, 2006.

[77] Q. Shen, M. Hou, D. Liang, Z. Zhou, X. Li, Z. Shao, and B. Yi, "Study on the processes of start-up and shutdown in proton exchange membrane fuel cells," *Journal of Power Sources*, vol. 189, pp. 1114–1119, 2009.

[78] K. H. Lim, H.-S. Oh, S.-E. Jang, Y.-J. Ko, H.-J. Kim, and H. Kim, "Effect of operating conditions on carbon corrosion in polymer electrolyte membrane fuel cells," *Journal of Power Sources*, vol. 193, pp. 575–579, 2009.

[79] D. Condit and R. Breault, "Shut-down procedure for hydrogen-air fuel cell system," *U.S. Patent*, no. 6,635,370, 2003.

[80] T. Bekkedahl, L. Bregoli, R. Breault, E. Dykeman, J. Meyers, T. Patterson, T. Skiba, C. Vargas, D. Yang, and J. Yi, "Reducing fuel cell cathode potential during startup and shutdown," *U.S. Patent*, no. 6,913,845, 2005.

[81] Y. D. Decker, J. B. Benziger, E. Kimball, and I. G. Kevrekidis, "Multistability, nonlinear response and wave propagation in self-humidified PEM fuel cells," *Chemical Engineering Science*, vol. 65, pp. 2399–2409, 2010.

[82] J. B. Siegel, "Modeling and design of PEM fuel cells for dead-ended anode operation," *University of Michigan Ph.D. Dissertation*, 2010.

[83] F. Rong, H. C, Z.-S. Liu, D. Song, and Q. Wang, "Microstructure changes in the catalyst layers of PEM fuel cells induced by load cycling Part I. Mechanical model," *Journal of Power Sources*, vol. 175, pp. 699–711, 2008.

[84] K. Kinoshita, *Carbon–electrochemical and physicochemical properties*. John Wiley & Sons. Inc., 1988.

[85] Z. Liu, L. Yang, Z. Mao, W. Zhuge, Y. Zhang, and L. Wang, "Behavior of PEMFC in starvation," *Journal of Power Sources*, vol. 157, pp. 166–176, 2006.

[86] Z. Liu, B. Brady, R. Carter, B. Litteer, M. Budinski, J. Hyun, and J. D. Muller, "Characterization of carbon corrosion-induced structural damage of PEM fuel cell cathode electrodes caused by local fuel starvation," *Journal of the Electrochemical Society*, vol. 155, pp. B979–B984, 2008.

[87] D. Liang, Q. Shen, M. Hou, Z. Shao, and B. Yi, "Study of the cell reversal process of large area proton exchange membrane fuel cells under fuel starvation," *Journal of Power Sources*, vol. 194, pp. 874–853, 2009.

[88] W. Gu, P. T. Yu, R. N. Carter, R. Makharia, and H. A. Gasteiger, *Modeling and Diagnostics of Polymer electrolyte fuel cells, modern aspects of electrochemistry 49*, U. Pasaogullari and C.-Y. Wang, Eds. Springer Science+Business Media, LLC, 2010.

[89] A. A. Franco and M. Gerard, "Multiscale model of carbon corrosion in a PEFC: Coupling with electrocatalysis and impact on performance degradation," *Journal of the Electrochemical Society*, vol. 155, no. 4, pp. B367–B384, Apr. 2008.

[90] A. Maslyn, "Carbon loss in the cathode catalyst support of proton exchange membrane fuel cells," *http://www.optics.rochester.edu/workgroups/cml/opt307/spr11/andrew/ThickResults.html*, 2011.

[91] L. Gutaz, S. Escribano, and O. Sicardy, "Study by electron microscopy of proton exchange membrane fuel cell membrane-electrode assembly degradation mechanisms: Influence of local conditions," *Journal of Power Soucses*, vol. 212, pp. 169–178, 2012.

[92] J.-H. Park, S.-D. Yima, T. Kim, S.-H. Park, Y.-G. Yoon, G.-G. Park, T.-H. Yang, and E.-D. Park, "Understanding the mechanism of membrane electrode assembly degradation by carbon corrosion by analyzing the microstructural changes in the cathode catalyst layers and polarization losses in proton exchange membrane fuel cell," *Electrichimita Acta*, vol. 83, pp. 294–304, 2012.

[93] H.-S. Oh, K. H. Lim, B. Roh, I. Hwang, and H. Kim, "Corrosion resistance and sintering effect of carbon supports in polymer electrolyte membrane fuel cells," *Electrichimita Acta*, vol. 54, pp. 6515–6521, 2009.

[94] F. Xu, M. xian Wang, Q. Liu, H. fang Sun, S. Simonson, N. Ogbeifun, E. A. Stach, and J. Xie, "Investigation of the carbon corrosion process for polymer electrolyte fuel cells using a rotating disk electrode technique," *Journal of the Electrochemical Society*, vol. 157, pp. B1138–B1145, 2010.

[95] O. Cherstiouk, A. Simonov, N. Moseva, S. Cherepanova, P. Simonov, V. Zaikovskii, and E. Savinova, "Microstructure effects on the electrochemical corrosion of carbon materials and carbon-supported Pt catalysts," *Electrichimita Acta*, vol. 55, pp. 8453–8460, 2010.

[96] K. Artyushkov, S. Pylypenko, M. Dowlapalli, and P. Atanassov, "Structure-to-property relationships in fuel cell catalyst supports: Correlation of surface chemistry and morphology with oxidation resistance of carbon blacks," *Journal of Power Sources*, vol. 214, pp. 303–313, 2012.

[97] W. Sun, B. A. Peppley, and K. Karan, "An improved two-dimensional agglomerate cathode model to study the influence of catalyst layer structural parameters," *Electrichimita Acta*, vol. 50, pp. 3359–3374, 2005.

[98] M. Secanell, K. Karan, A. Suleman, and N. Djilali, "Multi-variable optimization of PEMFC cathodes using an agglomerate model," *Electrichimita Acta*, vol. 52, pp. 6318–6337, 2007.

[99] C. Marr and X. Li, "Composition and performance modelling of catalyst layer in a proton exchange membrane fuel cell," *Journal of Power Sources*, vol. 77, pp. 17–27, 1999.

[100] N. R. Amundson, T.-W. Pan, and V. I. Paulsen, "Diffusion with Stefan and Maxwell," *AIChE Journal*, vol. 49, pp. 813–830, 2003.

[101] R. Ahluwalia and X. Wang, "Buildup of nitrogen in direct hydrogen polymer-electrolyte fuel cell stacks," *Journal of Power Sources*, vol. 171, pp. 63–71, 2007.

[102] A. Weber and J. Newman, "Transport in polymer-electrolyte membranes," *Journal of the Electrochemical Society*, vol. 151, pp. A311–A325, 2004.

[103] A. Weber, "Gas-crossover and membrane-pinhole effects in polymer-electrolyte fuel cells," *Journal of the Electrochemical Society*, vol. 155, pp. B521–B531, 2008.

[104] P. T. Yu, W. Gu, R. Makharia, F. T. Wagner, and H. A. G. and, "The impact of carbon stability on PEM fuel cell startup and shutdown voltage degradation," *ECS transactions*, vol. 3, pp. 797–809, 2006.

[105] Y. Lee, B. Kim, and Y. Kim, "An experimental study on water transport through the membrane of a PEFC operating in the dead-end mode," *International Journal of Hydrogen Energy*, vol. 34, pp. 7768–7779, 2009.

[106] M. Secanell, J. Wishart, and P. Dobson, "Computational design and optimization of fuel cells and fuel cell systems: A review," *Journal of Power Sources*, vol. 196, pp. 3690–3704, 2011.

[107] M. Grujicic and K. Chittajallu, "Optimization of the cathode geometry in polymer electrolyte membrane (PEM) fuel cells," *Chemical Engineering Science*, vol. 59, pp. 5883–5895, 2004.

[108] H.-H. Lin, C.-H. Cheng, C.-Y. Soong, F. Chen, and W.-M. Yan, "Optimization of key parameters in the proton exchange membrane fuel cell," *Journal of Power Sources*, vol. 162, pp. 246–254, 2006.

[109] D. Song, Q. Wang, Z. Liu, T. Navessin, M. Eikerling, and S. Holdcroft, "Numerical optimization study of the catalyst layer of PEM fuel cell cathode," *Journal of Power Sources*, vol. 126, pp. 104–111, 2004.

[110] M. Secanell, B. Carnes, A. Suleman, and N. Djilali, "Numerical optimization of proton exchange membrane fuel cell cathode electrodes," *Electrochimica Acta*, vol. 52, pp. 2668–2682, 2007.

[111] J. Wu, Q. Liu, and H. Fang, "Toward the optimization of operating conditions for hydrogen polymer electrolyte fuel cells," *Journal of Power Sources*, vol. 156, pp. 388–399, 2006.

[112] W. Wu and Y.-T. Lin, "Fuzzy-based multi-objective optimization of DMFC system efficiencies," *International Journal of Hydrogen Energy*, vol. 35, pp. 9701–9708, 2010.

[113] J. Wishart, Z. Dong, and M. Secanell, "Optimization of a PEM fuel cell system based on empirical data and a generalized electrochemical semi-empirical model," *Journal of Power Sources*, vol. 27, pp. 1041–1055, 2006.

[114] H. Zhao and A. F. Burke, "Optimization of fuel cell system operating conditions for fuel cell vehicles," *Journal of Power Sources*, vol. 15, pp. 408–416, 2009.

[115] S. Hikita, F. Nakatani, K. Yamane, and Y. Takagi, "Power-generation characteristics of hydrogen fuel cell with dead-end system," *JSAE Review*, vol. 23, pp. 177–182, 2002.

[116] L. Dumercy, M.-C. Pera, R. Glises, D. Hissel, S. Hamandi, F. Badin, and J.-M. Kauffmann, "PEFC stack operation in anodic dead end mode," *Fuel Cells*, vol. 4, pp. 352–357, 2004.

[117] O. Himanen, T. Hottinen, and S. Tuurala, "Operation of a planar free-breathing PEMFC in a dead-end mode," *Electrochemistry Communications*, vol. 9, pp. 891–894, 2007.

[118] J. W. Choi, Y.-S. Hwang, S. W. Cha, and M. S. Kim, "Experimental study on enhancing the fuel efficiency of an anodic dead-end mode polymer electrolyte membrane fuel cell by oscillating the hydrogen," *International Journal of Hydrogen Energy*, vol. 35, pp. 12 469–12 479, 2010.

[119] S. Dehn, M. Woehr, and A. Heinzel, "Development of a near-dead-ended fuel cell stack operation in an automotive drive system," in *Vehicle Power and Propulsion Conference (VPPC), IEEE*, 2011.

[120] T. Yang and P. Shi, "A preliminary study of a six-cell stack with dead-end anode and open-slits cathode," *International Journal of Hydrogen Energy*, vol. 33, pp. 2795–2801, 2008.

[121] A. Mokmeli and S. Asghari, "An investigation into the effect of anode purging on the fuel cell performance," *International Journal of Hydrogen Energy*, vol. 35, pp. 9276–9282, 2010.

[122] J. Chen, J. B. Siegel, and A. G. Stefanopoulou, "Nitrogen blanketing front equilibria in dead end anode fuel cell operation," in *American Control Conference*, San Francisco, CA, 2011.

[123] Q. Ye and T. Nguyen, "Three-dimensional simulation of liquid water distribution in a PEMFC with experimentally measured capillary functions," *Journal of Electrochemical Society*, vol. 154, pp. B1242–B1251, 2007.

[124] W. Borutzky, B. Barnard, and J. Thoma, "An orifice flow model for laminar and turbulent conditions," *Simulation modeling practice and theory*, vol. 10, pp. 141–152, 2002.

[125] P. Mocoteguy, F. Druart, Y. Bultel, S. Besse, and A. Rakotondrainibe, "Monodimensional modeling and experimental study of the dynamic behavior of proton exchange membrane fuel cell stack operating in dead-end mode," *Journal of Power Sources*, vol. 167, pp. 349–357, 2007.

[126] D. McKay, J. Siegel, W. Ott, and A. Stefanopoulou, "Parameterization and prediction of temporal fuel cell voltage behavior during flooding and drying conditions," *Journal of Power Sources*, vol. 178, pp. 207–222, 2008.

[127] C. A. Ramos-Paja, C. Bordons, A. Romero, R. Giral, and L. Martnez-Salamero, "Minimum fuel consumption strategy for PEM fuel cells," *IEEE Transactions on Industrial Electronics*, vol. 56, pp. 685–696, 2009.

[128] A. Manokaran, S. Pushpavanam, P. Sridhar, and S. Pitchumani, "Experimental analysis of spatio-temporal behavior of anodic dead-end mode operated polymer electrolyte fuel cell," *Journal of Power Sources*, vol. 196, pp. 9931–9938, 2011.

[129] J. F. Moxley, S. Tulyani, and J. B. Benziger, "Steady-state multiplicity in the autohumidification polymer electrolyte membrane fuel cell," *Chemical Engineering Science*, vol. 58, pp. 4705–4708, 2003.

[130] C. Woo and J. Benziger, "PEM fuel cell current regulation by fuel feed control," *Chemical Engineering Science*, vol. 62, pp. 957–968, 2007.

[131] T. Madden, D. Weiss, N. Cipollini, D. Condit, M. Gummalla, S. Burlatsky, and V. Atrazhev, "Degradation of polymer-electrolyte membrane in fuel cells I Experimental," *Journal of the Electrochemical Society*, vol. 156, pp. B657–B662, 2009.

[132] M. Gummalla, V. Atrazhev, D. Condit, N. Cipollini, T. Madden, N. Kuzminyh, D. Weiss, and S. Burlatsky, "Degradation of polymer-electrolyte membrane in fuel cells ii theoretical model," *Journal of the Electrochemical Society*, vol. 157, pp. B1542–B1548, 2010.

[133] S. Burlatsky, M. Gummalla, V. Atrazhev, D. Dmitriev, N. Kuzminyh, and N. Erikhman, "The dynamics of platinum precipitation in an ion exchange membrane," *Journal of the Electrochemical Society*, vol. 158, pp. B322–B330, 2011.